UNIVERSITY OF CALIFORNIA
RIVERSIDE

Molecular Beam Epitaxial Growth and Characterization of Graphene and Hexagonal Boron Nitride Two-Dimensional Layers

A Dissertation submitted in partial satisfaction
of the requirements for the degree of

Doctor of Philosophy

in

Electrical Engineering

by

Renjing Zheng

June 2017

Dissertation Committee:
Dr. Jianlin Liu, Chairperson
Dr. Roger Lake
Dr. Yongtao Cui

The Dissertation of Renjing Zheng is approved:

_____

_____

_____

Committee Chairperson

University of California, Riverside

ACKNOWLEDGEMENTS

First of all, I want to make my sincere gratitude to my advisor, Prof. Jianlin Liu, who gives me extensive research opportunities and support for my Ph.D. study. I made the decision to transfer to Electrical Engineering in my third year of UC Riverside. Dr. Liu kindly accepted me and helped me build up a very exciting research proposal. We have a lot of insightful discussions and he always provides significant suggestions about the research. The scientific thinking strategy and hardworking attitude learned from Dr. Liu helps me to finish my Ph.D. work and will definitely benefit a lot in my future career. And Dr. Liu cares about students very much; I enjoy the annual party the group members and families celebrating together. Thank you very much for mentoring me. I'm very grateful to Prof. Roger Lake and Prof. Yongtao Cui, who are my committee members and provide very helpful advice and collaboration during my research work.

I would like to acknowledge my labmates for their assistance in research. They are Zheng Zuo, Jian Huang, Zhongguang Xu, Alireza Khanaki, Hao Tian, Monzur Morshed, Mohammad Suja, Sunayna Bashar, Wenhao Shi, Yanwei He, Zhenjun Cui and Jingchuan Yang. I also want to thank my dear friends in UC Riverside. I enjoy the happy moment together with you guys and wish our friendship forever.

I would like to give my appreciation to my parents and younger brother. My hard-working parents have sacrificed a lot to get me well-educated and they have provided their best to me and my brother. Their unconditional trust and love makes this dissertation to come true. I also want to express my thanks to the new additions of my family, my husband as well as his wonderful family who all have been supportive and caring.

The best part from my graduate life is finding my best friend, soul-mate, and husband: Zilong, who is a true and great supporter and unconditionally loves me during my good and bad times. These past several years (especially two of us were pursing Ph.D. degrees at the same time) is not an easy ride. No matter what happens, he is always with me. We both have learnt a lot from each other and grown up with better understanding of the life. We have the faith in the coming life adventure together.

Previously Published Material Acknowledgment

1) The results in Chapter 3 have been published in “Zuo, Zheng*, Zhongguang Xu*, Renjing Zheng* (co-first author), Alireza Khanaki, Jian-Guo Zheng, and Jianlin Liu. "In-situ epitaxial growth of graphene/h-BN van der Waals heterostructures by molecular beam epitaxy." Scientific reports 5 (2015).”.

(http://www.nature.com/articles/srep14760)

2) The results in Chapter 4 have been published in “Zheng, Renjing, Zhongguang Xu, Alireza Khanaki, Hao Tian, Zheng Zuo, Jian-Guo Zheng, and Jianlin Liu. "Low-temperature growth of graphene on iron substrate by molecular beam epitaxy." Thin Solid Films 627 (2017): 39-43.”.

(http://www.sciencedirect.com/science/article/pii/S0040609017301566)

3) The results in Chapter 5 were submitted to Applied Physics Letter on May 1st, 2017.

I dedicate this thesis to

my parents and my husband,

for their constant support and unconditional love.

I love you all dearly.

ABSTRACT OF THE DISSERTATION

Molecular Beam Epitaxial Growth and Characterization of
Graphene and Hexagonal Boron Nitride Two-Dimensional Layers

by

Renjing Zheng

Doctor of Philosophy, Graduate Program in Electrical Engineering
University of California, Riverside, June 2017
Dr. Jianlin Liu, Chairperson

Van der Waals (vdW) materials (also called as two-dimensional (2D) material in some literature) systems have received extensive attention recently due to their potential applications in next-generation electronics platform. Exciting properties have been discovered in this field, however, the performance and properties of the systems rely on the materials' quality and interface significantly, leading to the urgent need for scalable synthesis of high-quality vdW crystals and heterostructures. Toward this direction, this dissertation is devoted on the study of Molecular Beam Epitaxy (MBE) growth and various characterization of vdW materials and heterostructures, especially graphene and hexagonal boron nitride (h-BN). The goal is to achieve high-quality vdW materials and related heterostructures. There are mainly four projects discussed in this dissertation.

The first project (Chapter 2) is about MBE growth of large-area h-BN on copper foil. After the growth, the film was transferred onto SiO_2 substrate for characterization. It is observed that as-grown film gives evident h-BN Raman spectrum; what's more, h-BN peak intensity and position is dependent on film thickness. N-1s and B-1s XPS peaks further suggest the formation of h-BN. AFM and SEM images show the film is flat and continuous

over large area. Our synthesis method shows it's possible to use MBE to achieve h-BN growth and could also pave a way for some unique structure, such as h-BN/graphene heterostructures and doped h-BN films by MBE.

The second project (Chapter 3) is focused on establishment of grapehene/h-BN heterostructure on cobalt (Co) film. In-situ epitaxial growth of graphene/h-BN heterostructures on Co film substrate was achieved by using plasma-assisted MBE. The direct graphene/h-BN vertical stacking structures were demonstrated and further confirmed by various characterizations, such as Raman spectroscopy, SEM, XPS and TEM. Large area heterostructures consisting of single- /bilayer graphene and multilayer h-BN were achieved. The mismatch angle between graphene and h-BN is below 1º.

The third project (Chapter 4) is about graphene growth on Fe by MBE at low temperature. Temperature-dependent growth of graphene on Fe using MBE is studied. Two-dimensional (2D), large-area graphene samples were grown on Fe thin films, and characterized by Raman, X-ray photoelectron spectroscopy, X-ray diffraction, optical microscopy, transmission electron microscopy and atomic force microscopy. Graphene is achieved on Fe at a wide growth temperature range and as low as 400 °C. The growth mechanism is studied and shows graphene growth is associated with formation and decomposition of iron carbide.

The forth part is about a convenient way to produce vdW heterostructures: graphene growth of exfoliated h-BN on Co. We demonstrated graphene/h-BN heterostructures by growing graphene onto the substrates which consist of exfoliated h-BN on Co thin film using MBE. The heterostructure samples grown at different temperatures and growth

durations were characterized by Raman, optical microscopy, atomic force microscopy, microwave impedance microscopy and scanning tunneling microscopy. It is found that the graphene/h-BN heterostructures were formed by the formation of graphene underneath rather than on top of the h-BN flakes. The growth mechanism is discussed.

In summary, we develop and optimize growth of vdW materials (h-BN and graphene), and vdW heterostructures by MBE. Various characterization has been carried out to evaluate properties of the films in structural, optical and electrical aspects. Our results reveal that MBE can provide an excellent alternative way for reliable growth of high-quality and large-size vdW materials and related heterostructures, which will attract more attention for the utilization of MBE in vdW materials research.

Contents

List of Tables:

List of Figures:

Chapter 1 Introduction to van der Waals materials and molecular beam epitaxy

1.1 Van der Waals materials and related heterostrucures

Van der Waals (vdW) materials are layer-structured materials with strong covalent bond within layer and weak vdW forces between layers, which is named as two-dimensional (2D) materials in some literatures. This group of materials have received high interest recently for their novel properties and high potential in various applications (photovoltaics, semiconductors, etc.) [1-8]. VdW materials have a big family as shown in Table 1.1. While graphene is currently one of the most prominent vdW members, beyond graphene materials such as MoS_2, ZnSe, topological insulators and hexagonal boron nitride (h-BN) are also being eagerly investigated [9-16].

<table>
<tr><td>Graphene family</td><td>Graphene</td><td colspan="2">hBN
'white graphene'</td><td>BCN</td><td>Fluorographene</td><td>Graphene oxide</td></tr>
<tr><td rowspan="2">2D chalcogenIdes</td><td colspan="2" rowspan="2">MoS_2, WS_2, $MoSe_2$, WSe_2</td><td colspan="2" rowspan="2">Semiconducting dichalcogenides:
$MoTe_2$, WTe_2,
ZrS_2, $ZrSe_2$ and so on</td><td colspan="2">Metallic dichalcogenides:
$NbSe_2$, NbS_2, TaS_2, TiS_2, $NiSe_2$ and so on</td></tr>
<tr><td colspan="2">Layered semiconductors:
GaSe, GaTe, InSe, Bi_2Se_3 and so on</td></tr>
<tr><td rowspan="2">2D oxides</td><td>Micas,
BSCCO</td><td colspan="2">MoO_3, WO_3</td><td colspan="2" rowspan="2">Perovskite-type:
$LaNb_2O_7$, $(Ca,Sr)_2Nb_3O_{10}$,
$Bi_4Ti_3O_{12}$, $Ca_2Ta_2TiO_{10}$ and so on</td><td>Hydroxides:
$Ni(OH)_2$, $Eu(OH)_2$ and so on</td></tr>
<tr><td>Layered
Cu oxides</td><td colspan="2">TiO_2, MnO_2, V_2O_5,
TaO_3, RuO_2 and so on</td><td>Others</td></tr>
</table>

Table 1.1 Current 2D library. The assorted colors indicate the different stability under ambient conditions (room temperature in air): blue (stable), green (probably stable), pink (stable in inert atmosphere), grey (little further information). 'Others' indicates that many other 2D crystals—including borides, carbides, nitrides and so on. (adapted with copyright permission [17])

For exploring new paradigm in the 2D devices, atomic-scale vdW heterostructures, which are made from a combination of alternating layers of graphene, h-BN, MoS_2 and so on, have been paid a great deal of attention to. Such heterostructures provide a fantastic and flexible platform to investigate novel phenomenon in fundamental physics, which has been reported in a lot of recent publications indicating superior properties for device applications [17-20]. Among these vdW heterostructures, the stacking of graphene with another vdW layer, in particular, h-BN [21-24], is of imminent interest.

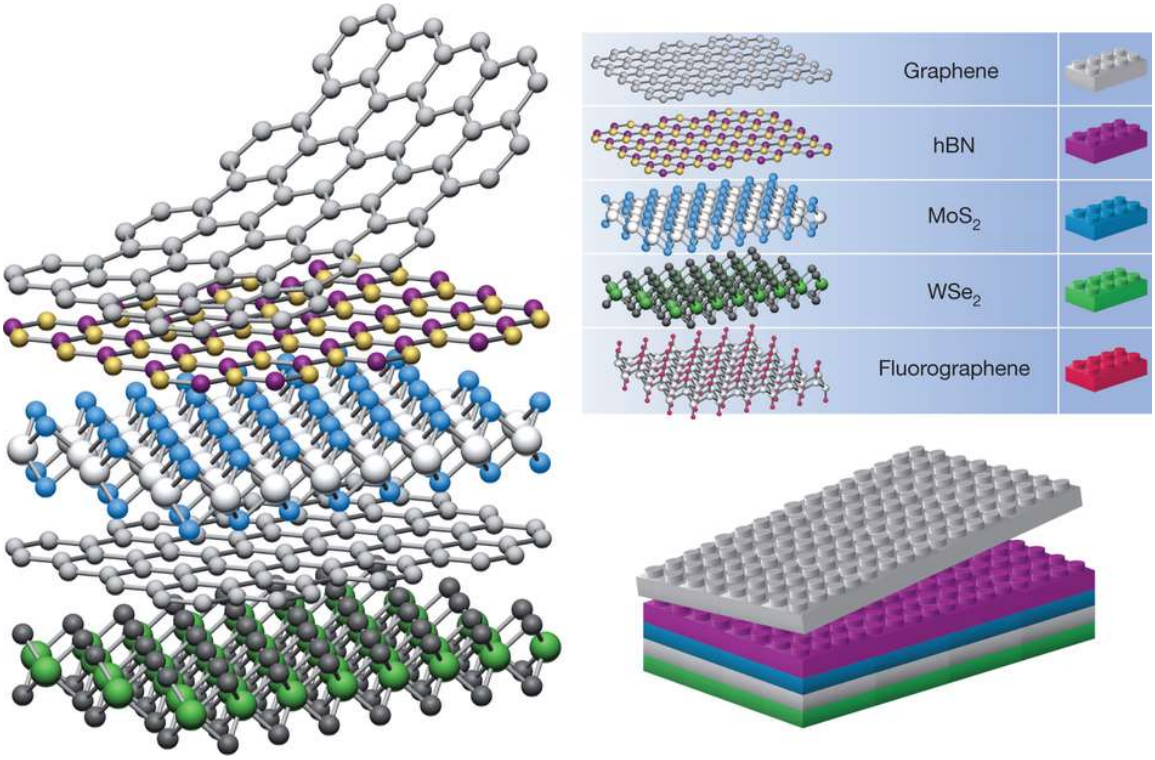

Fig. 1.1 Building up a vdW heterostructure. If one considers 2D crystals to be analogous to Lego blocks (right panel), the construction of a huge variety of layered structures becomes possible. Conceptually, this atomic-scale Lego resembles molecular beam epitaxy but employs different 'construction' rules and a distinct set of materials. (adapted with copyright permission [17])

To achieve vdW materials and heterostructures, mechanical exfoliation and chemical vapor deposition (CVD) growth were widely used [25-27]. A lot of success has been achieved. Nevertheless, direct deposition of high-quality, wafer-scale, well-aligned vdW materials and heterostructures remains challenging. As a versatile tool, molecular beam epitaxy (MBE) has natural advantages in high-quality heterostructure growth thanks to its ultra-high vacuum (UHV) environment, atomic layer epitaxy accuracy and controllability. Additionally, MBE has advantage of instant introduction and control of multiple sources, easy of doping of materials and in situ layer-by-layer characterization. As a matter of fact, vdW epitaxy was first demonstrated using MBE process [28]. Most recently, MBE has also been used to successfully synthesize single- and bi-layer graphene [29]. All of these give the hope and necessity to grow vdW materials and heterostructures by MBE, which is the main goal of this dissertation.

1.1.1 Graphene

Graphene is composed of single- or few-layer sp2-bonded carbon (C) atoms arranged in a 2D hexagonal crystal lattice, and its lateral dimension can span from nanoscale to wafer-scale. The atomic thin graphene layers are stacking together by weak vdW force, which forms few-layer graphene or even thick graphite. Besides graphite, the single layer graphene can be wrapped into fullerenes or carbon nanotubes, as shown in Fig. 1.2. Graphene has unintentionally been produced in small quantities for centuries, for example, pencil core is made from graphite mixed with clay and we are writing graphene layers on paper. However, until the year 2004, the microscale single-layer graphene was first successfully produced by mechanical exfoliation method [30]. Since then, a lot of research

efforts have been put into this extraordinary material and graphene-related research has developed to be a very important area of modern physics.

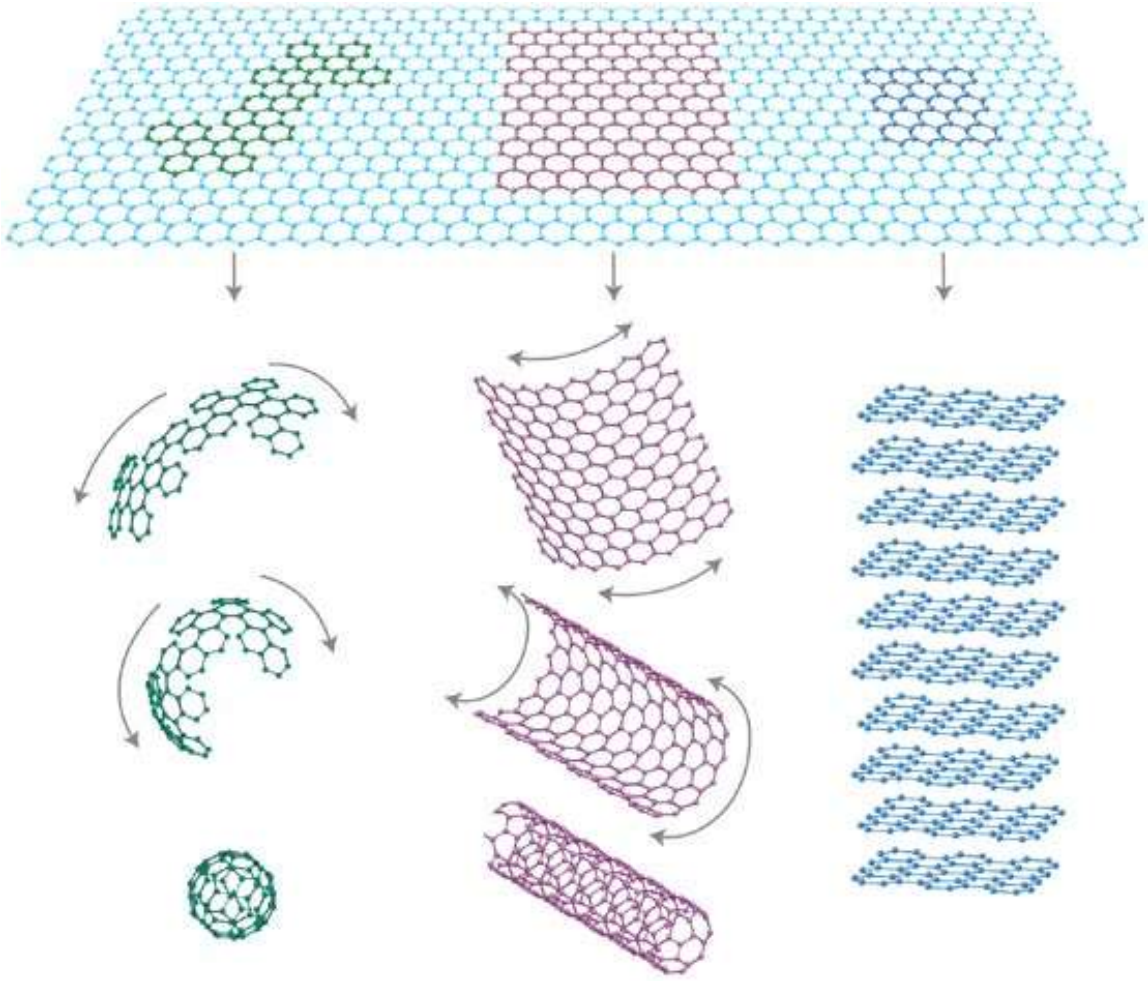

Fig.1.2 Graphene is a 2D building material for carbon materials of all other dimensionalities. It can be wrapped up into 0D buckyballs, rolled into 1D nanotubes or stacked into 3D graphite.

Because of its unique arrangement of carbon atoms (Fig.1.2), graphene has many unusual properties including core-like band structures (Fig. 1.3), high carrier mobility ($\sim 2*10^5$ $cm^2 \cdot V^{-1} \cdot s^{-1}$) [31, 32] with low resistivity (sheet resistance $\sim 10^{-6}$ $\Omega \cdot cm$) [33], high

thermal conductivity ((4.84±0.44)×10^3 to (5.30±0.48)×10^3 W/mK for room temperature) [34], superb chemical and thermal stability, optical transmittance (~97% transmission for white light) [35] and extraordinary mechanical strength (~ 1 TPa Young's modulus) [36], which allows for its wide variety of applications in the field of electronics, optics, sensors and biodevices [37, 38].

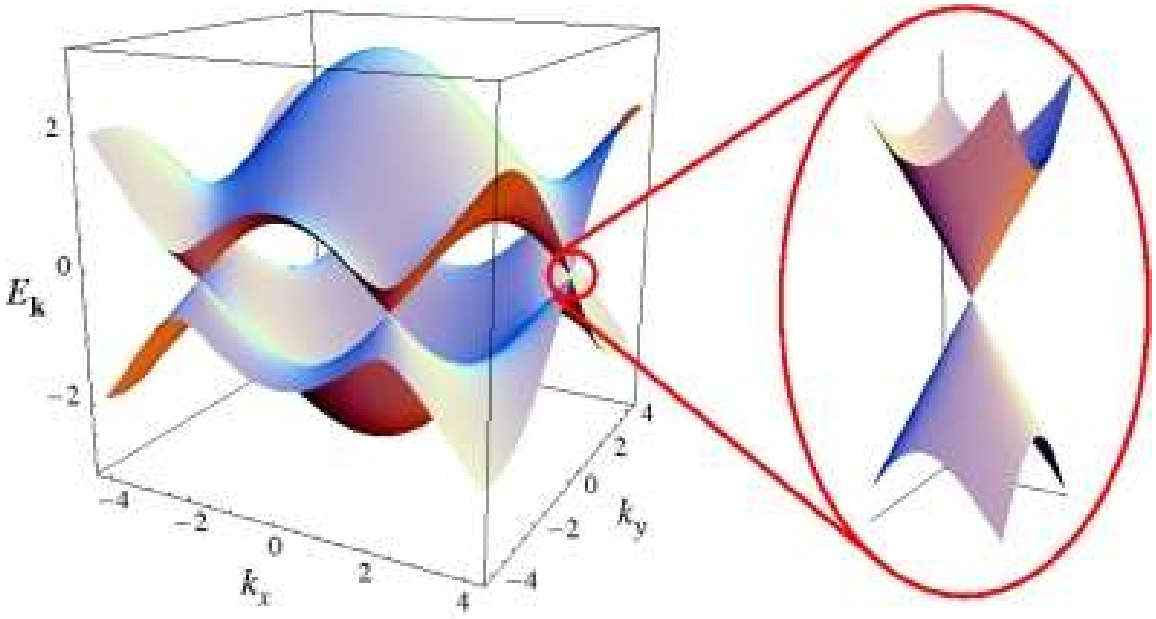

Fig. 1.3 Electronic dispersion in the honeycomb lattice. Left: energy spectrum (in units of t) for finite values of t and t′, with t=2.7eV and t′=−0.2t. Right: zoom in of the energy bands close to one of the Dirac points. (adapted from [86], with copyright permission)

However, graphene properties are hugely influenced by its quality and the interface. (as shown in Table 2.1) Numerous researchers have looked into methods to produce highly-crystalline wafer-scale graphene. Besides conventional "scotch tape" approach for exfoliating graphene from highly ordered pyrolytic graphite (HOPG) mentioned above, graphitization of silicon carbide surfaces [39-41], epitaxial growth on catalytic metal

substrates using CVD [42–44] and MBE [45, 46] are also used. To date, various substrates have been used as templates or substrates for high-quality graphene synthesis, such as Ru, Ir, Cu, etc. [42-49]. Among the graphene producing methods, CVD is the main technique to achieve large-scale high-quality graphene: In most cases, metal substrates are used for graphene growth by CVD method. During the growth, carbon-hydrogens gas is introduced into a CVD reaction chamber, and is decomposed into disassociated carbon at the surface of the metals, and then the disassociated carbon atoms form graphene structure. The decomposition asks for high levels of heat, which requires growth temperature around 1000 ˚C, with catalyst effect of metal substrates. Graphene CVD growth has been proved to be successful and been used for industry process, which produces the acceptable quality of graphene with effective control of the growth process. [50]

Type of graphene	Number of graphene layers	Graphene domain size (um)	Carrier mobility (cm2/V*s)	
			Field effect mobility	Hall mobility
Exfoliated graphite [30]	1	~10	3000-10000	N/A
Epitaxial SiC [39]	1-few	<10	N/A	200 at 27K
CVD/Ni [126]	1-few	10-50	100-2000	N/A
CVD/Cu [127]	1	10-100	N/A	7350 at 6K 5100 at 295K
CVD/Cu [128]	1	25-50	4050	N/A
CVD/Cu [73]	1	~200	4000	N/A
Chemical Exfoliated Graphite [129]	1	~20	365	N/A

Table 1.2 Reported uniformity (domain size) and quality (carrier mobility) of graphene prepared by various methods. (reproduced with copyright permission [130])

However, there are still problems associated with the graphene created by CVD. First, the growth mechanism is not yet fully understood, which leads to the difficulty in separation of graphene from the substrate without damaging structures or introducing other defects/particles. Second, it's still an obstacle to create a perfectly uniform layer of graphene, which is due to the kinetic dynamics of the gas during the reaction process. Third, because of the limitation of base pressure and vapor phase preferred sources, it remains challenging to realize graphene doped with some other elements. Therefore, the in-depth study of graphene growth by MBE is highly demanded.

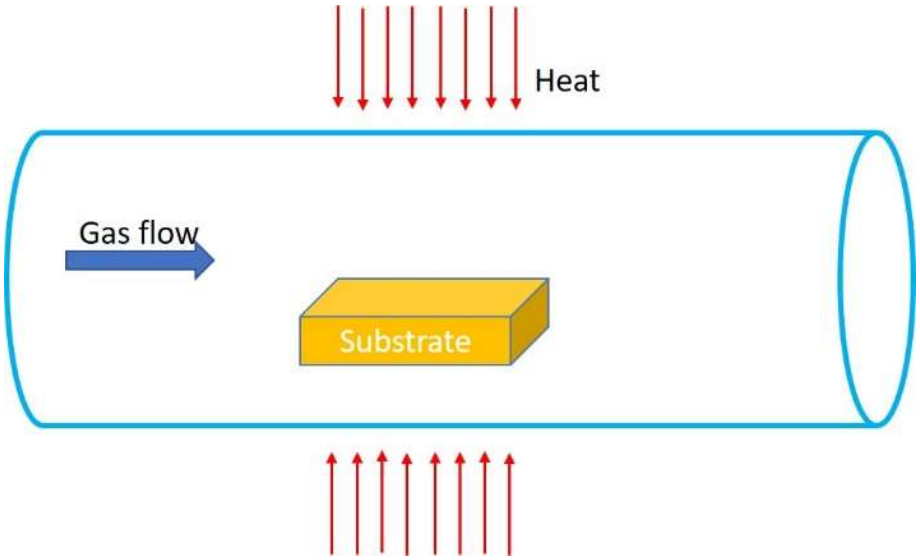

Fig.1.4 Illustration of CVD graphene growth procedure. Substrate is put in the middle of the furnace (low pressure CVD or atmospheric CVD), with carbon-hydrogens and carrier gas introduced as carbon source.

1.1.2 Hexagonal boron nitride

Hexagonal boron nitride (h-BN), known as 'white graphene', is wide band gap (~5.9 eV) [51] semiconductor sharing the same honeycomb lattice structure with

graphene. (Fig. 1.5) Similar as graphene, h-BN has strong covalent bond between B and N atoms within each layer, and weak vdW force between layers. H-BN has a very small in-plane lattice mismatch with graphene (~1.7%), which increase the possibility of graphene suspending perfectly on h-BN. H-BN has a low dielectric constant (relative permittivity) ~ 4 [52], which is comparable with SiO_2 (~3.9) [53]. Also, h-BN shows atomic flat surface with low intrinsic defects. Additionally, h-BN is equipped with extraordinary chemical and thermal stability. These properties enable h-BN as an excellent barrier and substrate dielectric material for graphene and other vdW materials electronic devices. H-BN is also a promising material for ultraviolet (UV) light-emitting devices, which would be an alternative way for achieving compact UV optoelectronics [54-56].

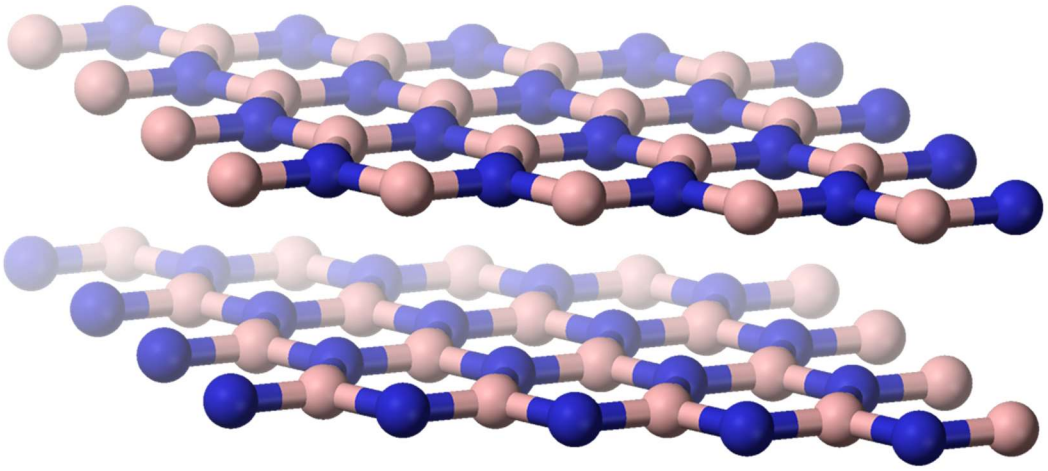

Fig.1.5 Structure of h-BN. (adapted from Wikipedia)

Similar as graphene and other vdW materials, h-BN's performance is also largely influenced by thickness and quality. For example, although the band gap of single or few layer h-BN is almost the same as bulk h-BN, some direct tunneling phenomena has been

observed at ultra-thin h-BN layers [59]. H-BN's barrier height for tunneling is measured to be 3.07 eV with breakdown voltage ~ 7.95 MV/cm, which is at same level of the most commonly used dielectric material SiO_2. To get h-BN better used as ultrathin insulators and gate dielectrics, it is highly demanded of synthesis of high-quality h-BN layers with control of the thickness. To achieve the goal, conventional mechanical exfoliation and CVD are the main methods for h-BN layers production, similar as other vdW materials. Mechanical exfoliation has helped people to obtain high quality h-BN films but the efficiency for volume production is low. [60] The exfoliated h-BN flakes' sizes are usually around tens of micrometer with various thickness (single-layer h-BN is even harder to get compared with other thickness), and it would take a lot of efforts to achieve desired alignment per optimization request of vdW heterostructure.

To have wafer scale, single-crystalline h-BN and fine-control of the number of layers, using CVD method to produce h-BN has been studied intensively. Also, people have tried to use MBE to do the growth. [139. 140] Various precursors such as BF_3/ NH_3, BCl_3/ NH_3, and B_2H_6/ NH_3, borazine, hexachloroborazine, or trichloroborazine have been used for CVD h-BN growth [61-65]. Different substrates have been tried for the h-BN growth, such as Ru [135], Ni [88], Pd [136] and Pt [137]. Besides metal substrate, some other substrates, such as Si and sapphire, have also shown to be a successful substrate for h-BN growth. [71, 72] The growth usually starts with substrate cleaning procedures: substrate is polished by argon sputtering and then annealed to remove possible residues and achieve better flatness. After that, precursor gases will be introduced into the chamber to form h-BN layers. Success has been achieved via this method [61-65]. However, for most CVD growth of h-

BN, it suffers the problem of low growth rate. The growth of h-BN does not proceed in a layer-by-layer mode but becomes super slow after formation of the first monolayer, which is possibly because of the strong reduction reaction and weak vdW forces between layers to adhesive stacking layers. Additionally, compared with graphene, the interaction between substrates and h-BN is much weaker, which is due to the insulating property of h-BN. To solve the thickness issue, several treatments have been tried but are still under developing: for example, using ambient pressure CVD with low temperature growth followed by a post annealing process. In short, the crystal quality, homogeneity and the number of h-BN layers are all critical for practical applications, which calls for a mature recipe to satisfy all the requirements. People have tried different tuning process to achieve the goal, such as change precursor and H_2 partial pressure, and the research work is still on-going [73, 74].

1.1.3 Graphene and h-BN heterostructures

The current progress in graphene and h-BN materials has already provided us a versatile platform for discovering new physics and developing new devices, and it can further lead to a new paradigm of 'complex materials' by constructing graphene and h-BN as building blocks and then combining them into various 'architectures' as demanded, which is named as heterostructures. Thanks to well-matched lattice constants and the flexibility to create artificial materials which would make full use of the unique properties of graphene and h-BN, the heterostructures open doors for novel performance and numerous applications. For example, it has been discovered that the charge mobility in graphene on h-BN is much better compared with other substrates, about three times larger for graphene deposited on SiO_2 at the same carrier concentration. (Fig. 1.6)

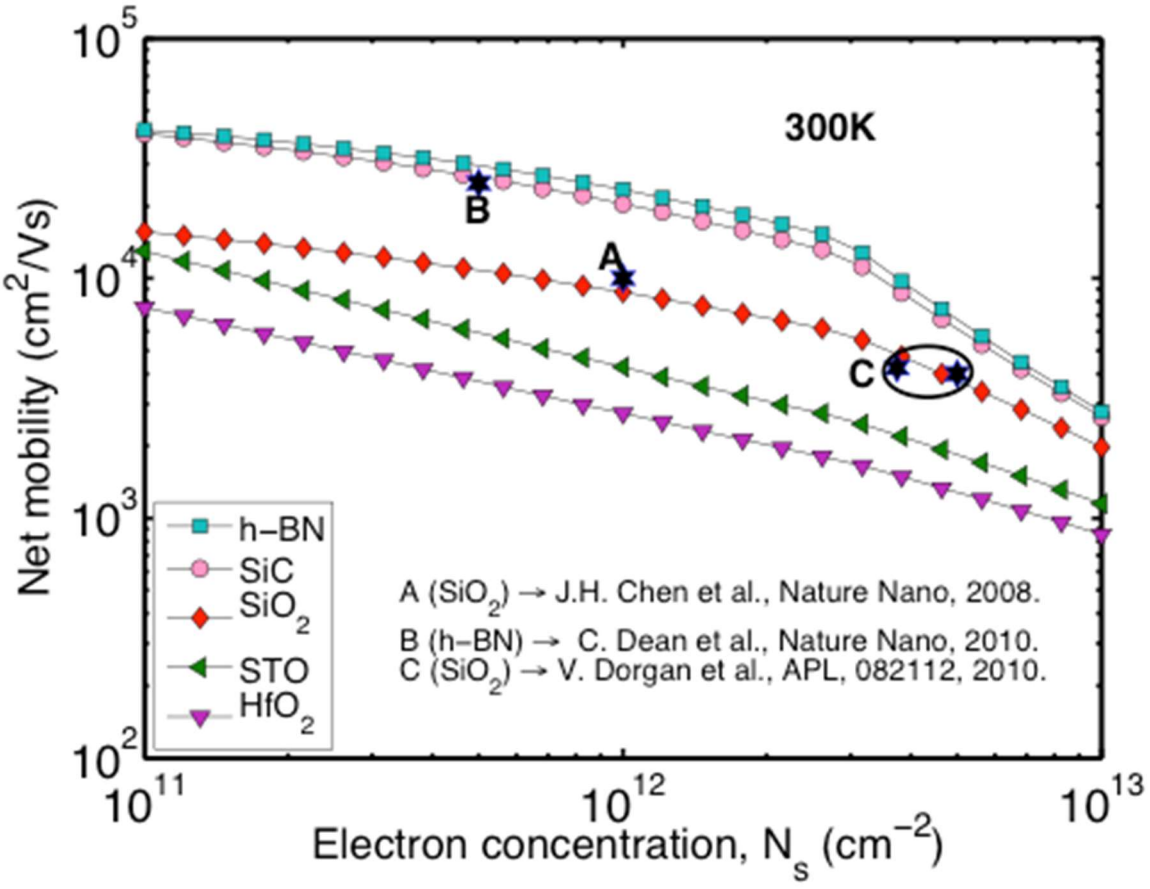

Fig.1.6 Effective mobility versus carrier concentration in graphene on various substrates at room temperature. Graphene on h-BN offers the best-case effective mobility because it is lattice matched with graphene. (adapted from [58] with copyright permission)

A unique characteristic of graphene and h-BN heterostructures is the weak vdW force between layers. As a result, there is no dangling bond and strain at the interface, which gives large tolerance of lattice mismatch between selective material vdW heterostructures [75, 76]. However, vdW force at the interface will result in a periodic distortion, which induces a unique Moiré pattern [77, 78]. A direct utilization of the Moiré pattern analyses is to derive the relative rotation angle of the stacked nanosheets when using transfer process (Fig. 1.7) to fabricate graphene-on-BN devices [133, 134]. Another thing needed to keep

in mind is that it has been verified that the AB stacking of the graphene/h-BN heterostructures (nitrogen atoms are positioned at the center of the graphene hexagon and boron atoms are positioned at the carbons location) is the most stable by first-principles calculations. Moreover, it is found that as the stress increases, the band gap of graphene h-BN heterostructures increases linearly. [83-86]

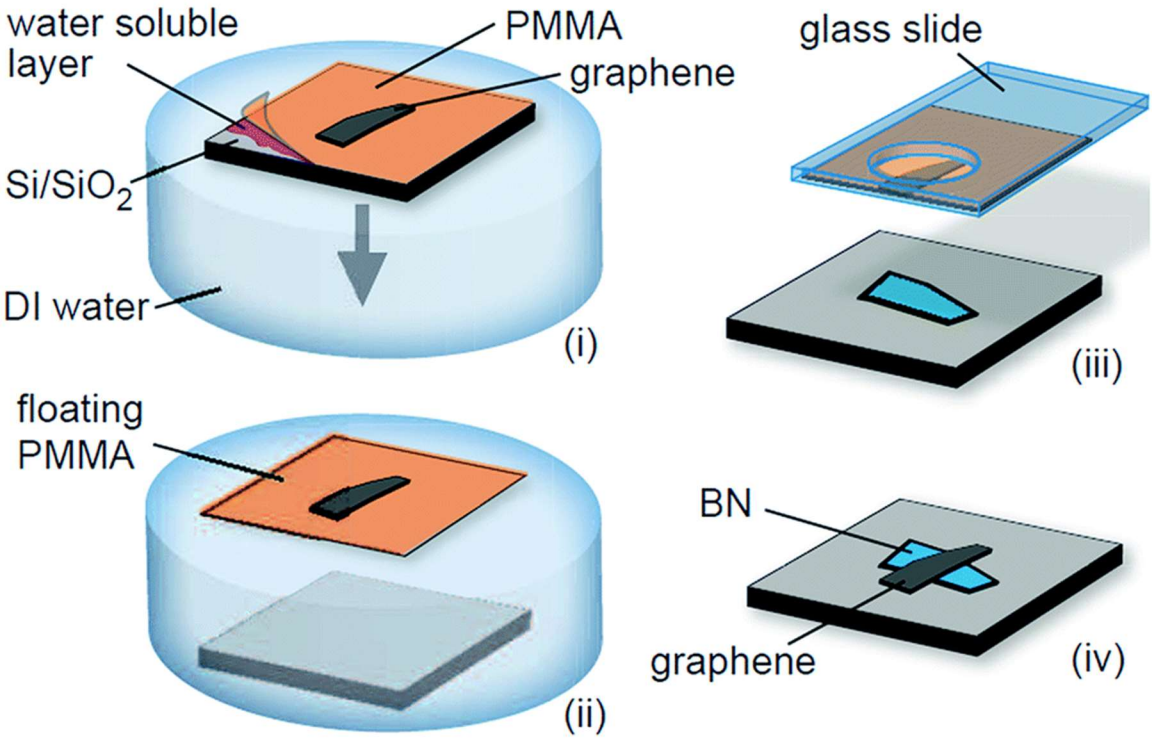

Fig. 1.7 Schematic of the transfer process to fabricate graphene-on-BN devices (adapted from [21] with copyright permission)

Based on the graphene and h-BN heterostructures, there are four key areas where the heterostructures can have a strong impact: (1) 'smart' ultra-strong nano-composite materials; (2) electro-mechanical devices for ultra-fast electronics; (3) materials with predetermined band-gap and work functions for next generation photovoltaic (solar-cells) applications; (4)

atomically thin film transistors for photonic applications. All of these raise huge demand for the production of high-quality and wafer-scale vdW materials and heterostructures, and in this thesis, we use MBE as the main growth tool to realize it.

1.2 Molecular beam epitaxy (MBE)

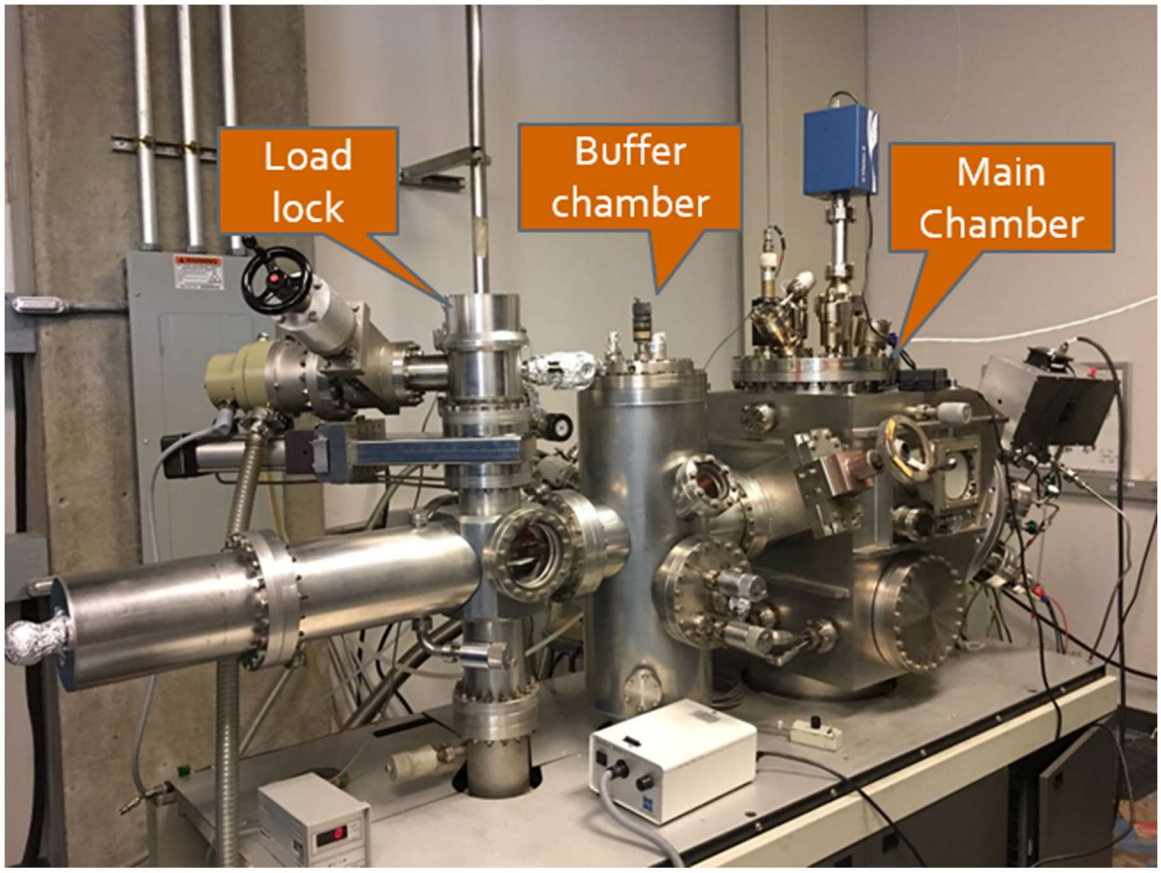

Fig. 1.8 Perkin Elmer MBE chamber in Quantum Structuresl Lab

MBE is a growth method which was invented in the late 1960s at Bell Lab by J. R. Arthur and Alfred Y. Cho. [87] The growth happens in high vacuum environment to produce high-quality, single-crystalline epitaxial ultrathin films and heterostructures made of semiconductors, metals and insulators. It is considered as one of the fundamental tools

for the research and development of the nanotechnology and has main natural advantages listed below.

First, the base pressure of MBE chamber is kept at high vacuum or ultra-high vacuum (UHV) (10^{-9} - 10^{-12} torr). This offers growth happening at clean condition and eliminates defects from contaminations. In Quantum Structures Lab (QSL), we use Perkin Elmer 425 system for vdW materials growth, as shown in Fig. 1.7. There are three connected chambers which ensure UHV base pressure: 1. Load lock chamber, whose pressure is ~ 10^{-5} – 10^{-6} torr with help of mechanical and turbo pumps, can be open to atmosphere to load and unload samples before/ after growth. 2. Buffer chamber, whose pressure is ~ 10^{-7} – 10^{-8} torr with an ion pump, is used as transiting chamber between load lock and main chamber. And it serves to protect main chamber from exposed to load lock; sometimes it also performs necessary annealing process to remove possible water vapor. 3. Main chamber, also known as growth chamber, whose base pressure is ~ 10^{-9} – 10^{-10} torr with help of a series of powerful pumps (mechanical, turbo and ion pumps, etc.), is the place where growth happens. These chambers are separated with stainless steel valves.

Second, MBE' deposition rate is very low (typically less than 100 nm per hour), which allows the films to grow epitaxially, provides atomic layer accuracy and controllability, and easily dopes various materials. Since carrier gases will significantly affect mean free paths of diffused atoms or molecules, the slow deposition rates ask for UHV to achieve the same impurity levels as other deposition. Most of the sources in MBE chamber are solid sources with the materials in ultra-pure form (99.999% or higher). The materials are stored and heated in separate quasi-Knudsen effusion cells or electron beam

evaporators until they begin to slowly melt and evaporate. With precisely controlling of cell temperature or e-beam current, we can achieve growth rate as needed. During the growth, the on-and-off status of diffused elements is controlled by physical shutters. Various materials are created with a form of "molecular beam", which means that evaporated atoms do not interact with each other or chamber base pressure gases before reaching the substrate, due to the long mean free paths of the atoms. After a long-distance traveling (larger than several inches), the elements condense onto a substrate, subsequently reacting with each other to form epitaxial films. Additionally, the atoms/ molecules travel to the surface of substrate with low momentum, which will also give low intrinsic defects. In QSL, the chamber is equipped with various sources to provide more possibilities and combinations for the growth, as shown in Fig. 1.8. Besides solid sources such as boron oxide cell, we also introduce different gas sources into the chamber to provide carbon, nitrogen and hydrogen atoms for the growth, which is controlled by needle valve and mass flow controller (MFC).

Third, MBE can provide in-situ layer-by-layer characterization. During growth procedure, reflection high energy electron diffraction (RHEED) is often used for monitoring the growth of the crystal layers. With a computer connected with a camera to record RHEED images during the growth, we can observe crystallite changes during the growth and further employ precise control of growth of each layer. In-situ growth of heterostructures or superlattices of different materials may be fabricated.

Fourth, the substrates are mounted on a manipulator which can be rotated in plane and out of plane to guarantee isotropic growth. The substrates can be heated to several hundred

degrees Celsius during operation with heater (made from graphite or tantalum filament) behind, which provides more chance for MBE's application for the growths flavoring high temperature. The temperature adjustment precision is 1 ˚C which can help accurately optimize growth temperature.

In conclusion, MBE system is powerful and versatile tool for vdW materials and heterostructures growth.

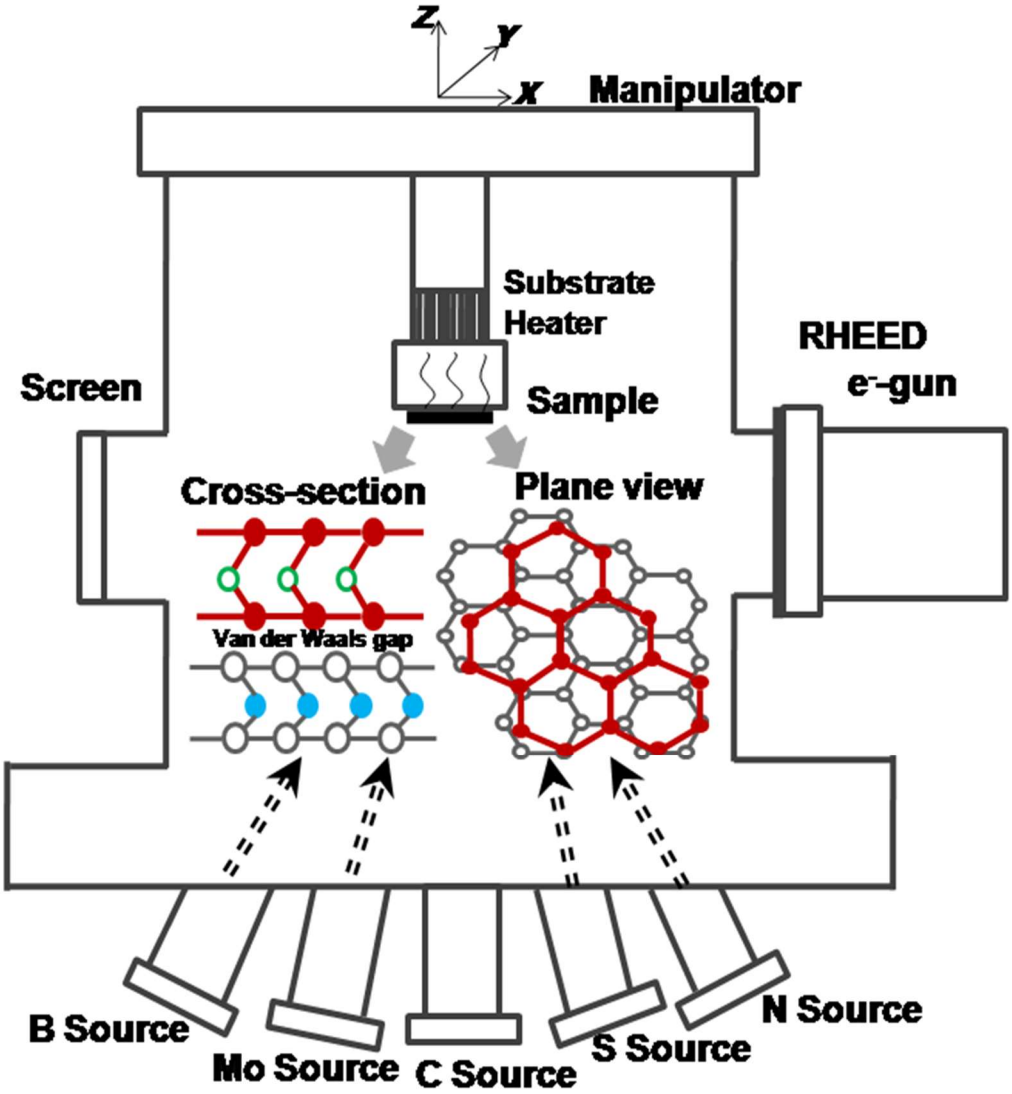

Fig. 1.8 Schematic of MBE growth chamber in Quantum Structures Lab

Chapter 2 Molecular beam epitaxy growth of hexagonal boron nitride on copper foil

2.1 Overview

Hexagonal boron nitride (h-BN) is a wide bandgap (5.97 eV) insulator, with the same layered honeycomb structure as graphene. It is a promising material for various applications, such as compact ultraviolet laser devices, dielectric substrate for graphene electronics, etc. A lot of success has been achieved with chemical vapor deposition (CVD) [88-91], but it hasn't been achieved by molecular beam epitaxy (MBE).

In this chapter, we report our study of MBE growth of large area h-BN on copper (Cu) foil. Various growth parameters combinations have been tried to achieve and optimize h-BN growth on Cu with MBE. After the growth, we transfer the film onto SiO_2 substrate for further characterization. As-grown film gives evident h-BN Raman spectrum; peak intensity and position of h-BN is dependent on film thickness. N-1s and B-1s are detected by XPS, which further suggest the formation of h-BN. AFM and SEM images show the film is flat and continuous over large area.

2.2 Growth procedures

Before growth, commercial Cu foil (99.999%, 0.025 mm thick, Alfa Aesar) is etched in 5% nitric acid for 30 s and then annealed by 10 sccm H_2 in MBE chamber at 900 ºC for 30 min. With help of etching and annealing, Cu surface has been improved significantly, which can be observed from AFM images shown in Fig. 2.1. The roughness (RMS) value decreases from previous 2.64 nm to 1.03 nm at 2 um scale, which gives a better chance to achieve h-BN growth by MBE.

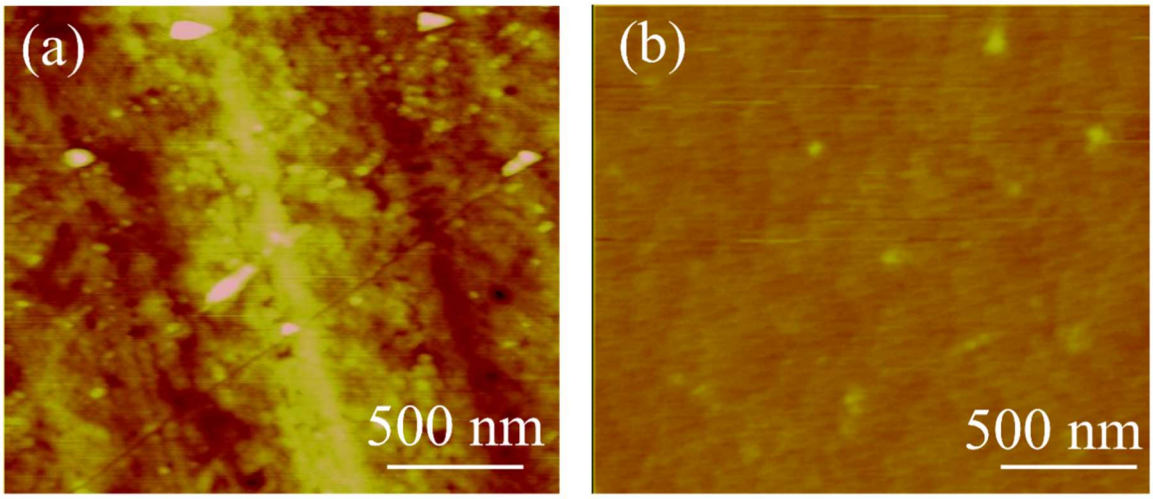

Fig. 2.1 AFM images of Cu foil (a) before and (b) after etching and annealing process.

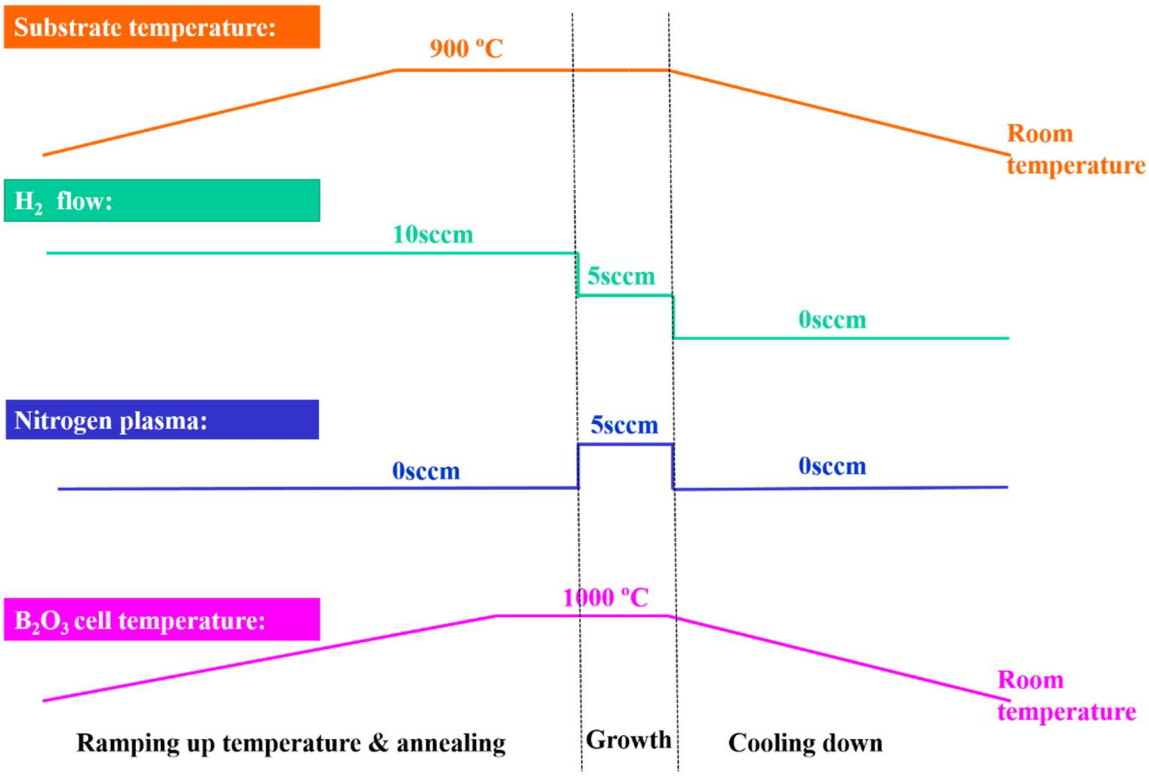

Fig. 2.2 Schematic of h-BN growth procedures on Cu foil by MBE.

After annealing, Cu foil is directly used for h-BN growth. With boron oxide effusion cell and nitrogen radio frequency (RF) plasma working as boron and nitrogen source,

respectively, H_2 is also introduced into the chamber to help anneal and grow h-BN. There are a lot of details to be optimized in such a growth. Four major parameters need to be tuned to achieve the success: substrate temperature, H_2 flow, nitrogen plasma flux (adjusted by RF plasma power and N_2 gas flux) and boron growth rate which is controlled by cell temperature. And the different time durations of four slots also have influence on the growth result, as discussed here:(i) ramping up of substrates and cell temperature; (ii) annealing of substrate; (iii) growth; (iv) cooling the system. After a lot of trials and fails, the typical growth parameter is determined as shown in Fig. 2.2. The substrate temperature is 900 ºC and boron cell temperature is 1000 ºC. The growth time is 60 min with ramping and cooling rate of 10 ºC/min. During the growth, H_2 flux is 5 sccm with N flux at 5 sccm.

2.3 Wet transfer technique of h-BN film onto SiO_2

After growth, the sample on Cu foil is detached from substrate holder. Since the thin thickness and softness of Cu, the foil is not flat over large scale. For further characterization, we use the standard wet transferring process to etch the copper foil and transfer h-BN film onto SiO_2 substrate. The transfer process can be found in Fig. 2.3. As-grown film is spun using 495 PMMA with a spin speed of 4000 rpm, which leaves the PMMA supporting layer thickness of ~2 um. After that, the film is baked at 100 ºC for 10 min in the air. Then, the sample is emerged into 5% $FeCl_3$ etchant to dissolve Cu and have grown film with PMMA floating on the solution. After washing the film in DI water for several times, we use SiO_2 wafer to take film out from DI water. The film is naturally dried on SiO_2 for 1 day to remove water and then put onto hot plate at 60 ºC overnight to remove possible water residue or vapor between film and SiO_2. The last step is dissolving PMMA in acetone and

blowing the sample dry with N_2 gun. After all these step, a piece of clean grown film is exposed on SiO_2 wafer.

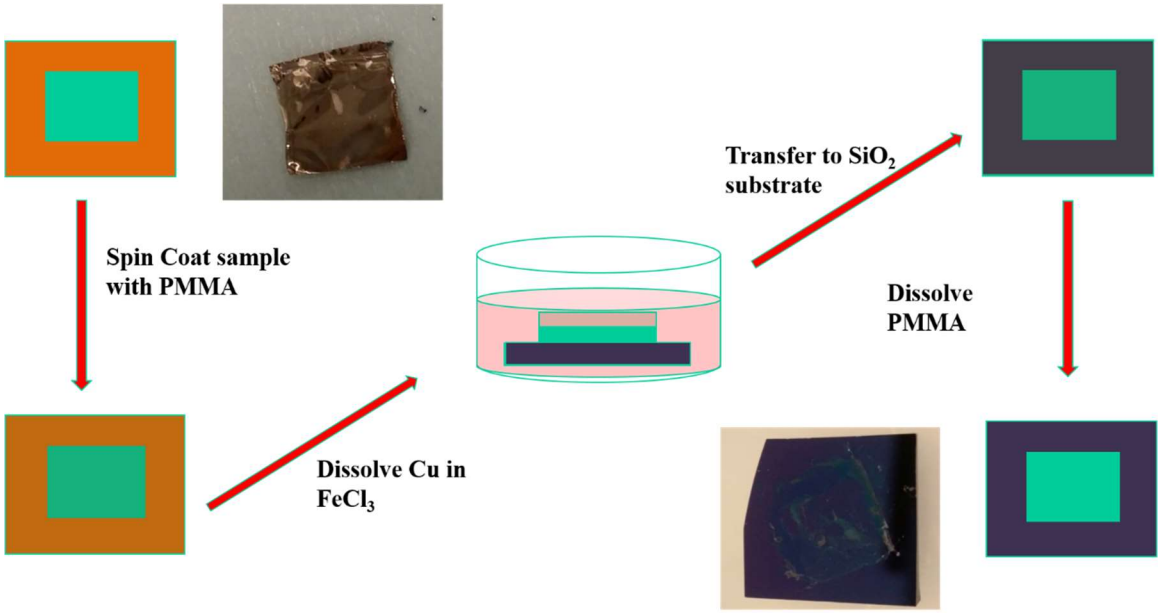

Fig. 2.3 Wet transferring procedure to produce h-BN/SiO_2 sample for further measurement.

2.4 Various characterization of h-BN film

After transferring, continuous h-BN film is observed on SiO_2, as shown in Fig.2.4. From optical microscopy image (Fig.2.4 (a)), h-BN film shows micrometer scale continuity, with most area showing green color. At some folded areas, yellow color is observed which is due to h-BN transmittance of white light changing with thickness. From SEM image (Fig.2.4 (b)), we observe h-BN film in contrast with SiO_2 substrate, which shows brighter color compared with SiO_2. At the edge of the film, triangular-like flakes with triangular teeth are observed. The shape indicates h-BN growth preference, which has been observed in CVD growth. [90] A lot of theoretical works focus on the formation of the triangular. [92, 93] The widely acceptable one is h-BN has different terminated edge: boron-

terminated or nitrogen-terminated because of composition of boron and nitrogen. The nitrogen-terminated edge has lower edge energy compared with boron-terminated edge. To minimize surface energy, triangular shape is energetically favorable compared with other shape from Wulff construction.

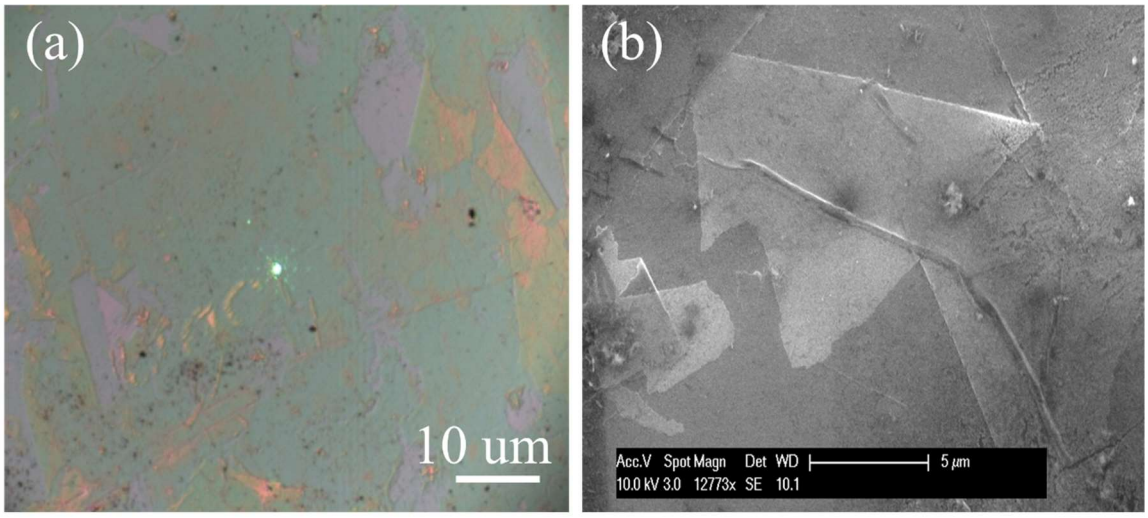

Fig. 2.4 Optical and SEM analysis of transferred h-BN on SiO_2.

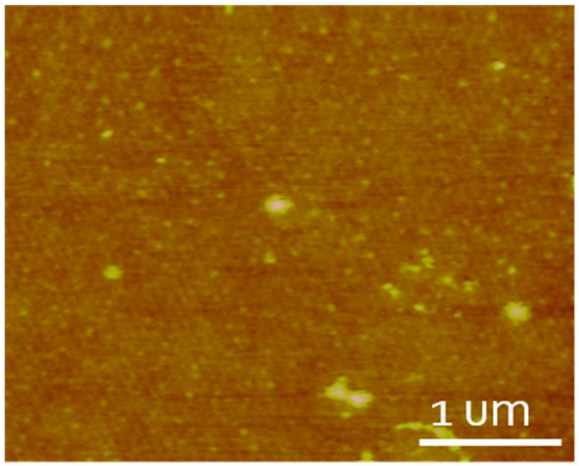

Fig. 2.5 AFM image of transferred h-BN film on SiO_2.

From AFM image shown in Fig. 2.5, it gives a locally uniform film with some residues left. The RMS is ~1.5 nm at 2 um scale.

Raman spectrum is measured using 532 nm laser as the excitation source on the transferred h-BN film, as shown in Fig. 2.6. The dominant peak locates at 1360 cm^{-1}, which is attributed to the B-N E_{2g} mode within h-BN layers. This is a direct proof of h-BN existence. Another two peaks are located at 520 cm^{-1} and 950 cm^{-1}, which are from SiO_2/Si

wafer. However, h-BN peak owns a large Full-Width-Half-Maximum (FWHM) value, which indicates the poor quality of grown h-BN.

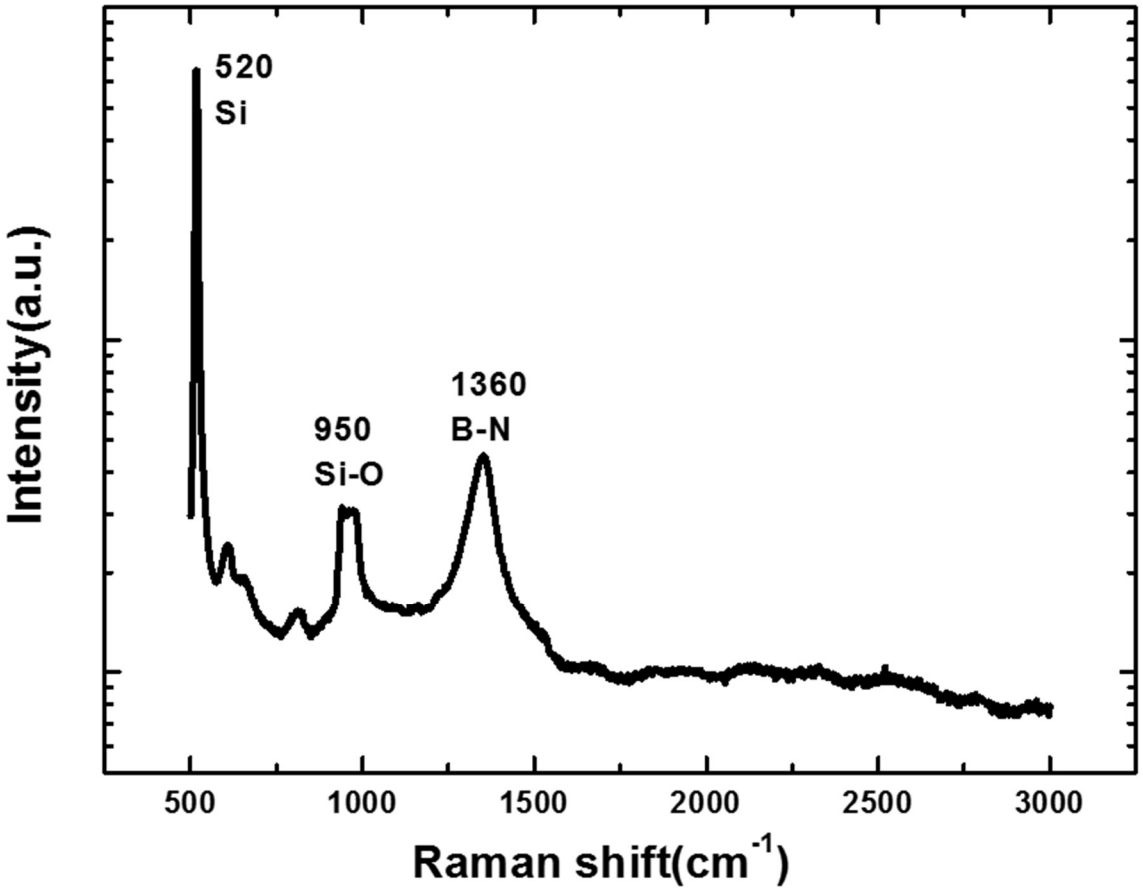

Fig. 2.6 Raman spectrum of h-BN on SiO_2.

Additionally, Raman is measured at different locations of transferred h-BN film. It can be observed that the peak intensity is dependent on thickness. (Shown in Fig. 2.7) When Raman spectrum is measured at thinner film (black circle), it gives smaller signal compared with thicker area (blue circle). What's more, peak position changes slightly with different locations. The Raman peak of thinner h-BN is higher compared with thicker h-BN. The observed change is due to thickness effect of optical phonon and the intrinsic

stretching of h-BN layers. The relationship between thickness and Raman shift paves a way to distinguish h-BN with different thickness. For example, atomically thin h-BN is harder to find under optical microscopy compared with graphene since h-BN does not absorb visible light. With using Raman related analysis, it is possible to see h-BN monolayers once a Raman spectrometer is calibrated for a given substrate.

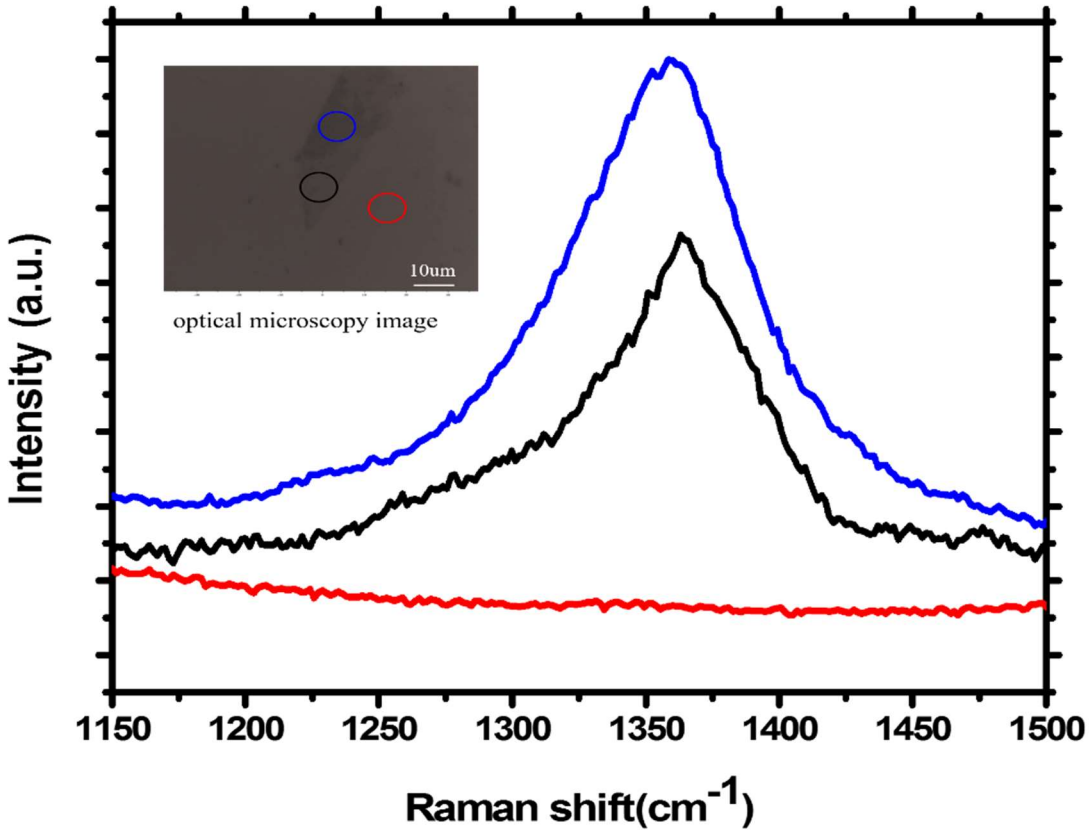

Fig. 2.7 Raman spectrum measured at different locations. Different colors are locations shown in the corresponding-color circles of inset optical microscopy image.

XPS spectrum is done on h-BN/SiO_2, which is shown in Fig. 2.8. The spectra of B1s exhibits curve with peak of ~191.6 eV and N1s peak ~397.7eV, which agrees with the

value of a boron compound with nitrogen. From all of the characterization, we can claim the successful growth of h-BN on Cu foil.

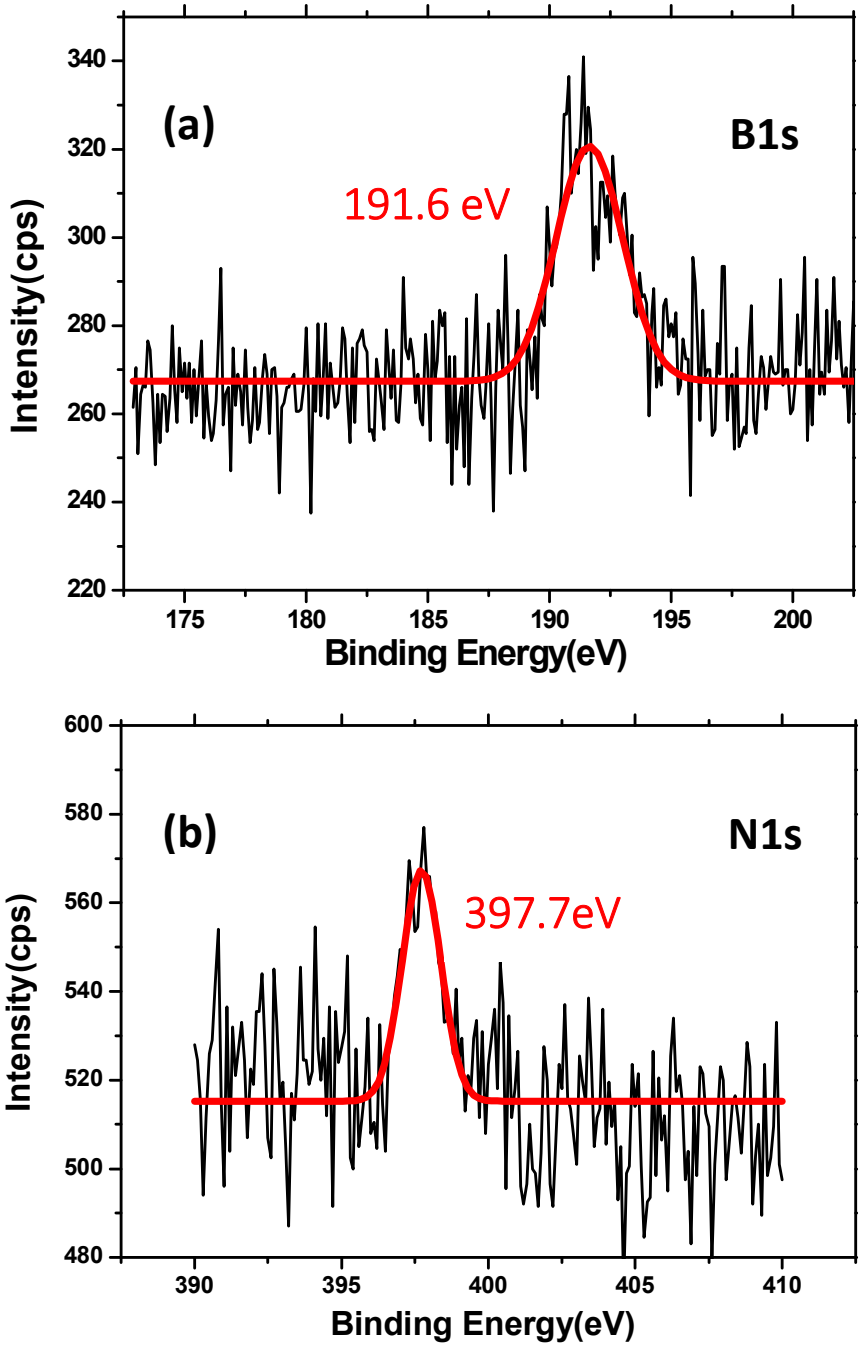

Fig. 2.8 XPS result measured on transferred h-BN/SiO_2 sample, located at (a) B1s and (b) N1s, respectively.

2.5 Discussion and problem encountered

We have successfully grown h-BN film on Cu foil with MBE method. Raman and XPS spectra indicate existence of h-BN, and the film is continuous under various microscopes. Our synthesis method could also make some unique structure possible, such as h-BN/graphene heterostructures and doped h-BN films. However, the growth suffers a very low success rate (<5%), which is due to heavy Cu evaporation under UHV condition. The heavy evaporation causes damage to heater. To solve the problem, we are looking for better substrate candidate which can resist evaporation at high temperature.

Chapter 3 In-situ epitaxial growth of graphene/h-BN van der Waals heterostructures by molecular beam epitaxy

3.1 Overview

As discussed at the end of Chapter 2, h-BN growth on Cu foil has succeeded but suffered low success rate and severe damage to the chamber due to heavy Cu evaporation. A new substrate material is highly demanded for h-BN growth. And besides van der Waals (vdW) materials themselves, the vdW heterostructures have also received a great deal of attention for their exceptional layered structures and exotic properties, which can open up various device applications in nanoelectronics. The production of graphene and h-BN heterojunctions with well-aligned, defect-free structure is the main demand to improve performance of graphene related devices. However, direct stacking of vdW materials remains difficult.

In this chapter, we demonstrate a solution for fabricating the graphene and h-BN vdW heterostructures on cobalt (Co) substrates. Various characterizations were carried out to evaluate the heterostructures. Wafer-scale heterostructures consisting of single-layer/bilayer graphene and multilayer h-BN were achieved. The mismatch angle between graphene and h-BN is below 1º. This work has been published in [131].

3.2 Growth procedures tuning process

Thermally oxidized Si wafers with a SiO_2 layer of 300 nm were used as substrates. They were transferred to an e-beam evaporator system for the deposition of a Co film of 400 nm. The wafers were subsequently loaded on to standard 3” wafer holders and

transferred to an MBE system (shown in Fig. 3.1) for growth. A Kundson effusion cell filled with B_2O_3 powder (Alfa Aesar, 99.999%) was used as B source. A thermos-cracker was used to crack acetylene gas (Airgas, 99.999%) as C source. The C source was tuned by either acetylene gas flow or cracker temperature. An electron cyclotron resonance (ECR) system was used to form nitrogen gas plasma (Airgas, 99.9999%) as N atomic source. The N source was tuned by either nitrogen gas flow or ECR magnetron current. Each individual source has its own gas cut off valve or front shutter to precisely control the growth. Those sources can be used in any combination to meet different structure requirements.

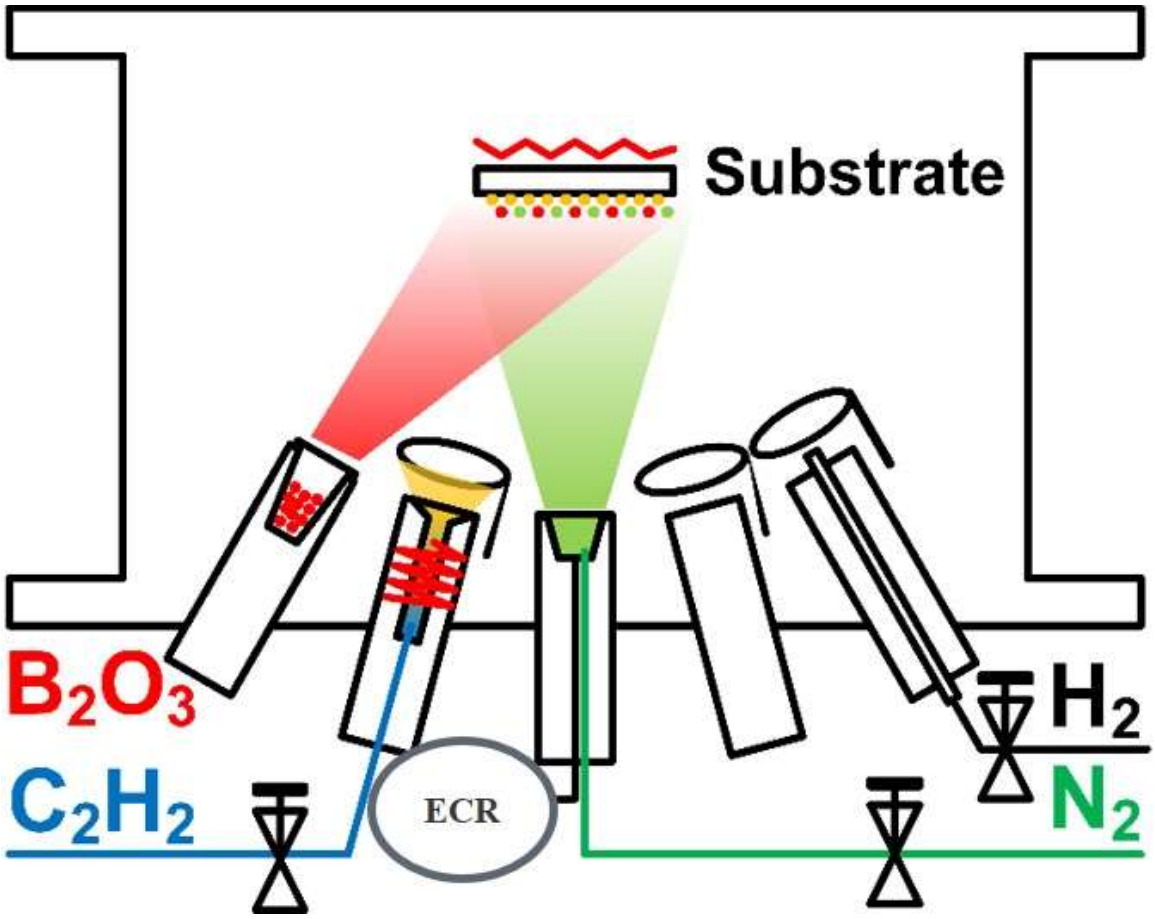

Fig. 3.1 Configuration of MBE chamber to grow graphene/h-BN heterostructure

During the growth, graphene was grown on Co film and then used as substrate for

subsequent h-BN growth. As shown in Fig. 3.2, there are various parameters to be tuned to reach optimized growth result. Five major parameters are listed as: 1. Co substrate temperature, on which growth happens; 2. C_2H_2 flux which is key for graphene growth; 3. N plasma flux and 4. Boron cell temperature, which has influence on the h-BN growth; 5. H_2 flux, which shows considerable influence on the growth result. The growth can be divided into four parts in terms of time flow: (i) ranging from ramping up of substrate and boron cell temperature; (ii) annealing substrate to remove possible oxides and contamination; (iii) growth of graphene and h-BN; and (iv) cool the system down. How long each portion takes also have impact on the result. Compared with h-BN growth on Cu in Chapter 2, the addition of parameter and time flow (iii) increases difficulty of the growth. With a lot of efforts on engineering of these parameters and different trials of combinations, we achieved successful growth conditions and results discussed below.

For a typical growth, the substrate is firstly annealed at 800~850 ºC under a hydrogen flow of 10 sccm for a duration of 30 minutes. At the end of substrate surface treatment, the hydrogen gas flow is stopped and substrate temperature is further ramped up to 870~900 ºC for graphene/h-BN heterostructure growth. The thermal cracker temperature is ramped to 1200 ºC and 3 sccm acetylene is introduced into the chamber for graphene growth. The growth lasts from 10 s to 1 minute. Subsequently, h-BN growth follows with minimal time gap. B cell temperature is precisely ramped to 900~1100 ºC right before h-BN layer growth. Nitrogen flow rate is 10 sccm and the growth lasts 10~15 minutes. At the end of h-BN growth, the substrate temperature is slowly cooled down towards room temperature at a rate of 10 ºC/min. The slow substrate cooling process suggests that the epitaxy undergoes

layer-by-layer growth mode, which is in contrast to fast cooling procedure with much higher cooling rates in the growth of graphene by precipitation of carbon atoms from the metal substrate in some CVD process [94, 95].

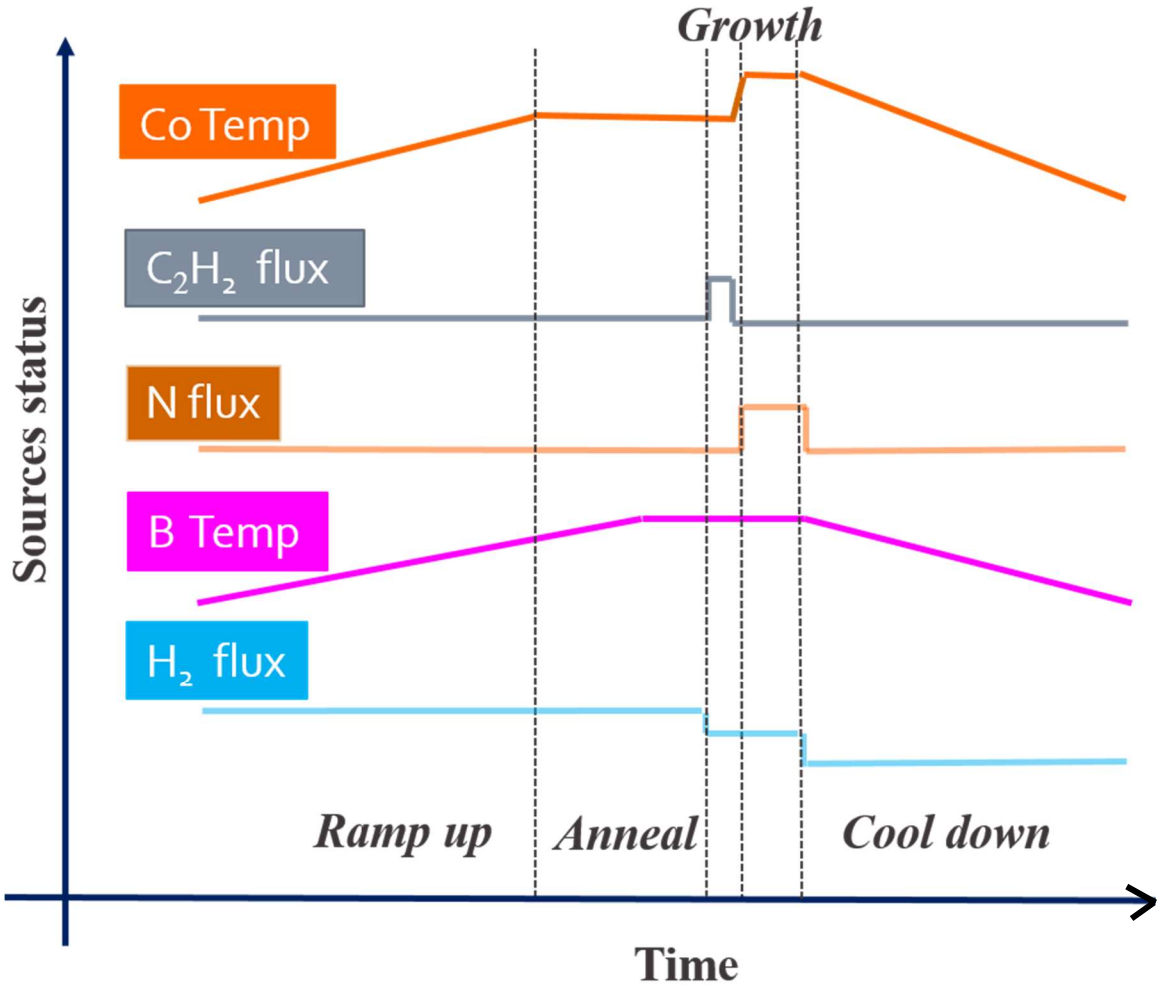

Fig. 3.2 Growth parameters and time division of graphene/h-BN heterostructure.

3.3 Various characterization of grown graphene/ h-BN heterostructures

Raman characterizations were performed using a HORIBA LabRam system equipped with a 50-mW 514-nm green laser. Scanning electron microscopy (SEM) images were acquired using a Philips XL30-FEG system. X-ray photoelectron spectroscopy (XPS) was

carried out using a Kratos AXIS ULTRA XPS system equipped with an Al Kα monochromatic X-ray source and a 165 mm mean radius electron energy hemispherical analyzer. Transmission electron microscopy (TEM) images and electron diffraction patterns were acquired using a FEI/Philips CM-30 TEM**.** Plan-view TEM sample was prepared using direct transfer method. After spin coated with PMMA, the sample was submerged in $FeCl_3$ solution to etch away the Co metal layer, which often takes several days. The film was then transferred onto carbon coated Cu TEM grid and treated with acetone and DI water to remove PMMA. Cross sectional TEM sample was prepared using focused ion beam technique. The graphene/h-BN thin film was covered by an Ir layer and further protected by electron-beam and ion-beam deposited Pt layers.

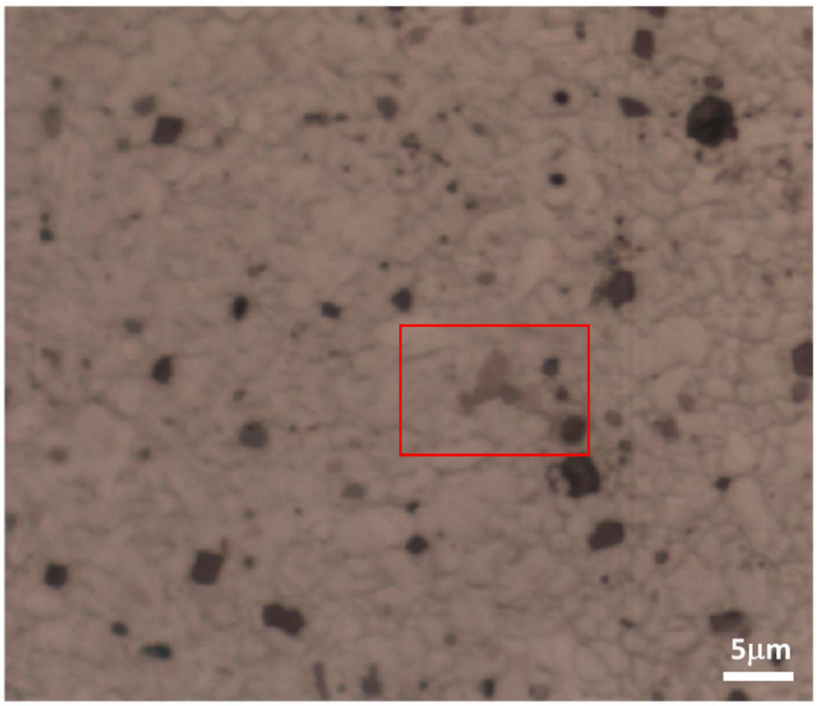

Fig. 3.3 Optical microscopy image of graphene/h-BN heterostructure sample with discrete h-BN triangular domains (Sample A). Rough surface with many holes has been observed. Different thickness of graphene shows on the image, as indicated in red square.

As grown vdW thin films are transparent, it is not visible for bare eye or through optical microscope, shown in Fig. 3.3. However, there are some surface imperfections easily seen, which result from the high temperature effect on Co. Similar results are observed with AFM shown in Fig. 3.4, Co roughness (RMS) increases from 1nm to 15nm at scale of 2 um, and Co forms grains of size is around several-hundred nanometers. The domains have different crystallinity but are locally flat.

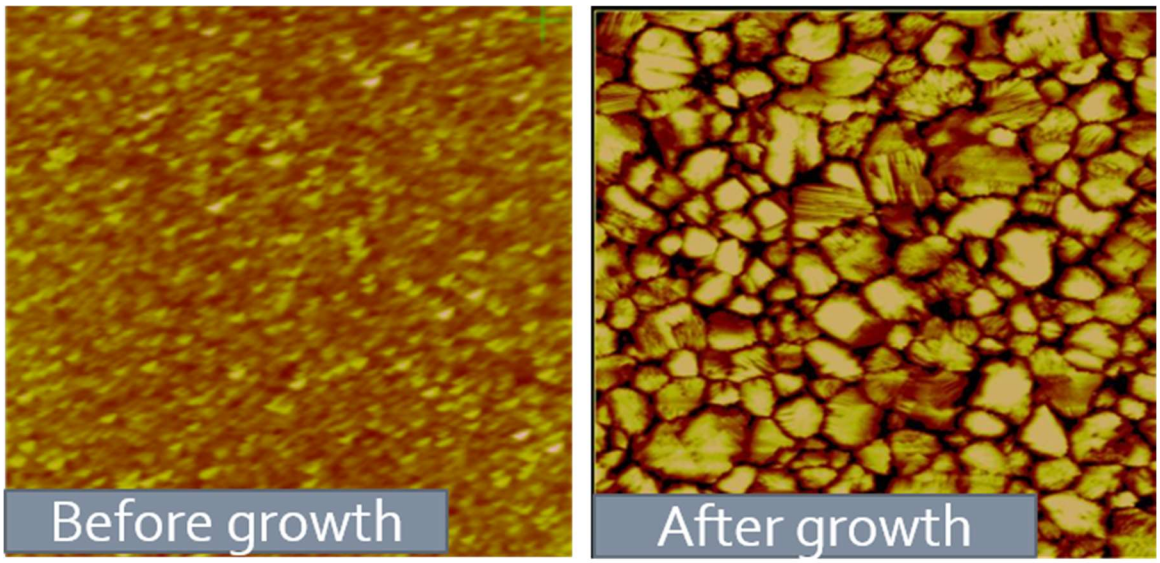

Fig. 3.4 AFM images of sample before and after growth (Sample A)

As the samples are imaged by SEM, a surface contrast is observed in secondary electron imaging mode because secondary electron signals from h-BN and graphene/Co substrate have different intensity. Fig.3.5 shows an SEM image of a graphene/h-BN sample (Sample A) on which large triangular domains of ~20 μm are observed. Despite the underlying very rough Co substrate surface, which consists of small grains due to heat treatment, wafer-scale graphene has been grown, followed by the formation of the triangular shaped h-BN domains as inferred by both SEM (Fig. 3.5) and Raman scattering

results (Fig. 3.6). As observed in the inset of Fig. 3.5, we can observe several large triangular flakes of size about 20 μm, which is direct proof of existence of h-BN. Holes features are observed, which is due to Co evaporation at high temperature. Moreover, some bright features are also observed, which is possibly due to excessive boron. It gives the hint that boron to nitrogen ratio needed to be further tuned to remove boron's over-deposition.

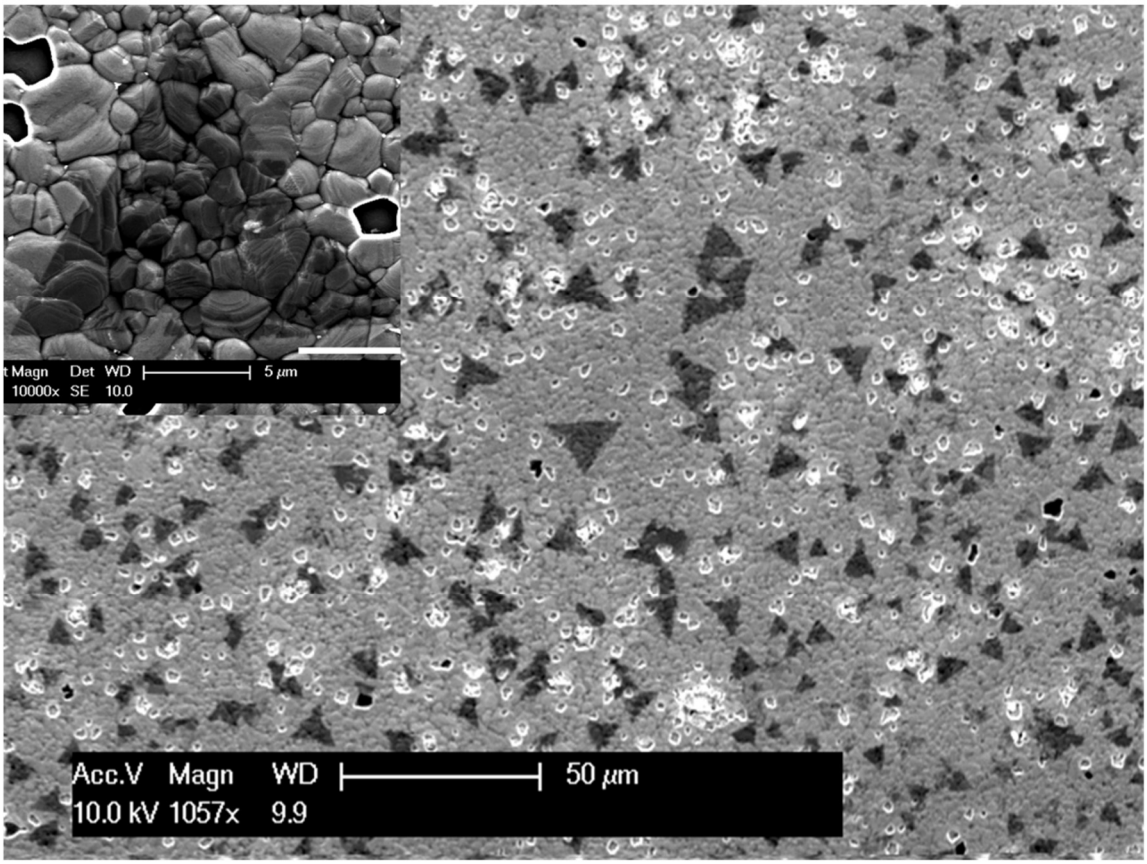

Fig. 3.5 SEM image of graphene/h-BN heterostructure on cobalt substrate (Sample A). Inset is taken under the same condition with larger magnification. The background is the rough substrate surface with packed Co grains resulted from heat treatment.

From Raman spectrum shown in Fig. 3.6(a), which is measured away from triangular shape. Three main peaks can be observed: first one is located at 1351 cm^{-1}, which is

graphene defect peak (D). Besides that, G and 2D peaks are also seen, namely, only graphene signal is detected. From G to 2D ratio, we conclude it is multilayer graphene. When Raman is measured on a triangle (Fig. 3.6 (b)), the first peak changes from 1351 cm^{-1} to 1360 cm^{-1}, which is more likely to be h-BN E_{2g} optical phonon peak. Besides that, the signature graphene G and 2D peaks are observed similar as (a). This result is in close agreement with the SEM result shown before.

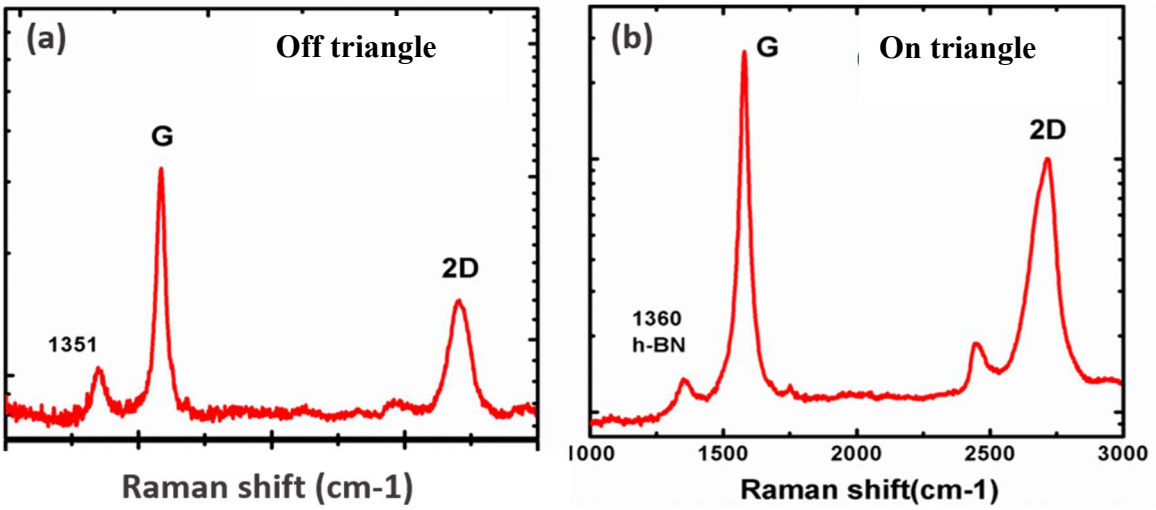

Fig. 3.6 Raman spectra of graphene/h-BN sample with discrete h-BN triangular domains (Sample A) acquired at different locations across the sample surface.

3.4 Morphology evolution

With growth conditions talked above, we achieved h-BN and graphene heterostructure, which is the first graphene/h-BN heterostructure grown by MBE method to the best of our knowledge. However, the surface quality is not good and h-BN are formed in discrete flake format. In order to achieve continuous wafer-scale h-BN film instead of discrete flakes,

fine-tuning of the sample growth condition was performed. Detailed difference in growth condition is summarized in Table 3.1.

Step	Parameters	Sample A	Sample B
Pre-growth Annealing	Temperature	800 °C	850 °C
	Duration	40 minutes	10 minutes
Graphene Growth	Substrate temperature	800 °C	850 °C
	Gas flow	3 sccm	3 sccm
	Cracker temperature	1200 °C	1000 °C
	Growth duration	1 minute	10 s
H-BN Growth	Substrate temperature	900 °C	850 °C
	Boron cell temperature	1000 °C	950 °C
	Nitrogen gas flow	10 sccm	10 sccm
	Nitrogen ECR current	50 mA	60 mA
	Growth duration	15 minutes	10 minutes

Table 3.1 Comparison of growth conditions of sample A and B.

First, the total growth duration was shortened to reduce heat treatment duration which helps to suppress Co evaporation. The shorten time is mainly from h-BN growth duration: decreasing from previous 15 min to 10 min. Additionally, both graphene and h-BN were grown at the same substrate temperature of 850 °C, thus the growth time delay between graphene layer and h-BN layer was minimized. After these adjustment, a direct improvement was observed with optical microscopy (Fig. 3.7). The resulting sample (Sample B) shows smoother surface morphology compared with Sample A (Fig. 3.5).

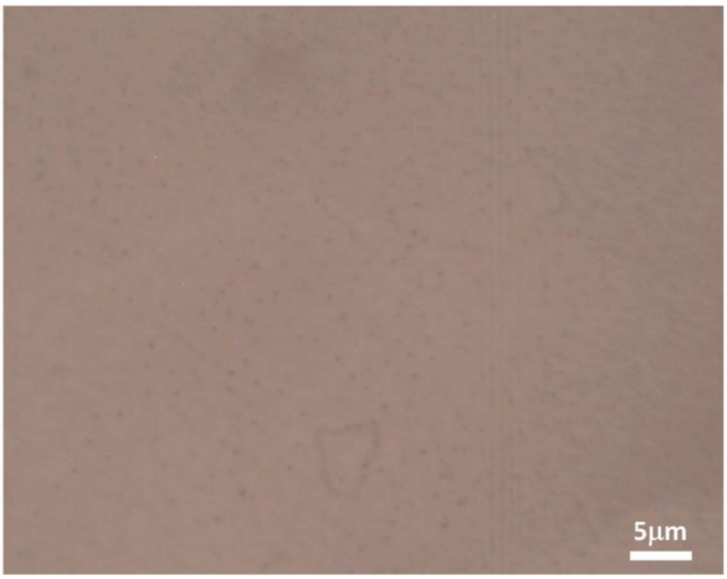

Fig. 3.7 Optical microscopy image of graphene/h-BN sample with wafer-scale film (Sample B)

Second, we try to improve graphene growth with direction of high quality and thinner layer thickness. A thinner graphene is expected with less carbon deposition. With this assumption, carbon thermal cracker temperature was decreased from 1200 °C to 1000 °C, and growth duration was changed from 1min to 10 s. Graphene growth temperature was increased by 50 °C which will help to align crystalline of graphene domain and achieve better quality of the film.

Third, parameters were tuned to balance boron to nitrogen ratio and further improve h-BN layer coverage and stoichiometry. Boron cell temperature was lowered from 1000 °C to 950 °C to lower boron deposition rate. And the ECR current of nitrogen plasma was increased from 50 mA to 60 mA to produce more nitrogen plasma to react with boron. Additionally, the growth temperature of h-BN was decreased from 900 °C to 850 °C.

With work of tuning these parameters, Sample B exhibits the graphene/h-BN film that covers the entire sample surface, and triangular h-BN domains are no longer visible (Fig. 3.8).

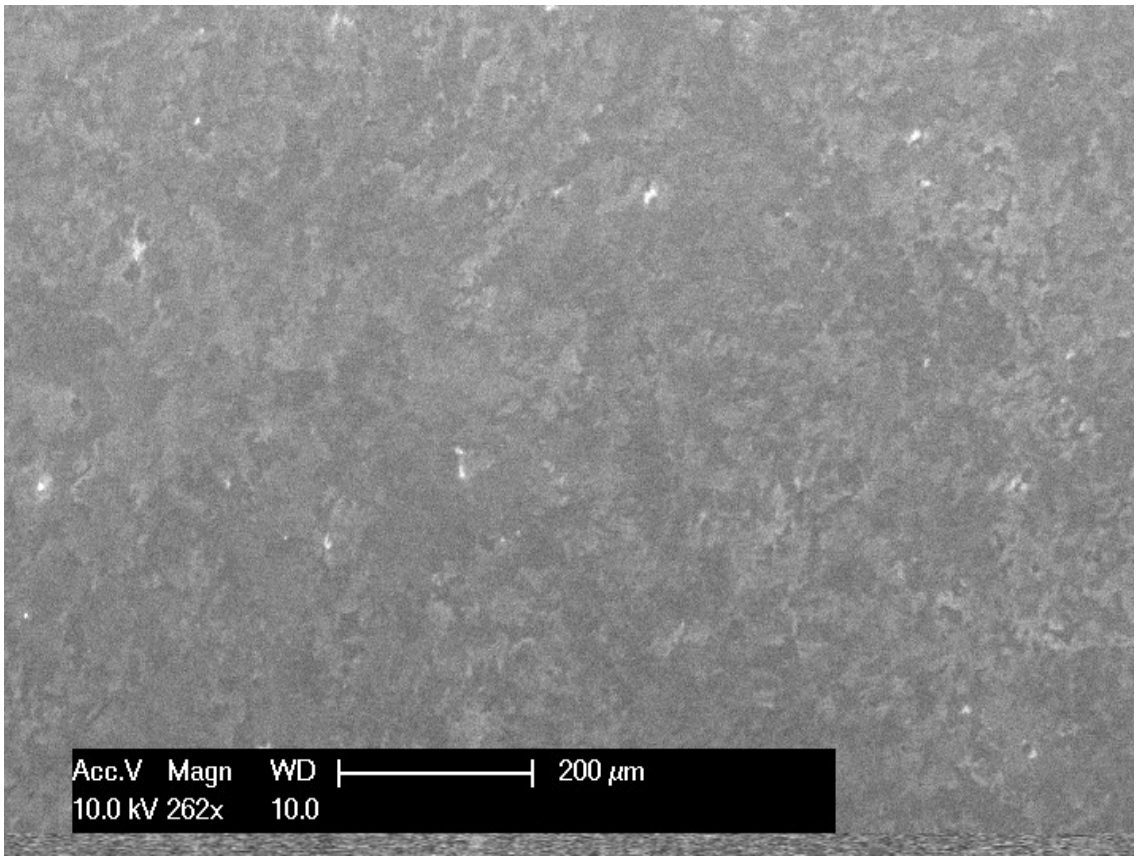

Fig. 3.8 SEM image of Sample B showing wafer-scale h-BN and graphene coverage, and without evident triangular domains.

To better study the parameters' effect on the growth result, two more samples were grown for reference using the same substrate annealing conditions as that of Sample A, while their graphene layers were grown at higher temperature (Sample C: 900 °C) and the h-BN layers were grown with a longer time (Sample D: 30 min h-BN growth duration). From the optical microscopy image and Raman spectra shown in Fig. 3.9, we find both

Sample C and D show continuous graphene/h-BN heterostructure films, however they are not as uniform as that of Sample B.

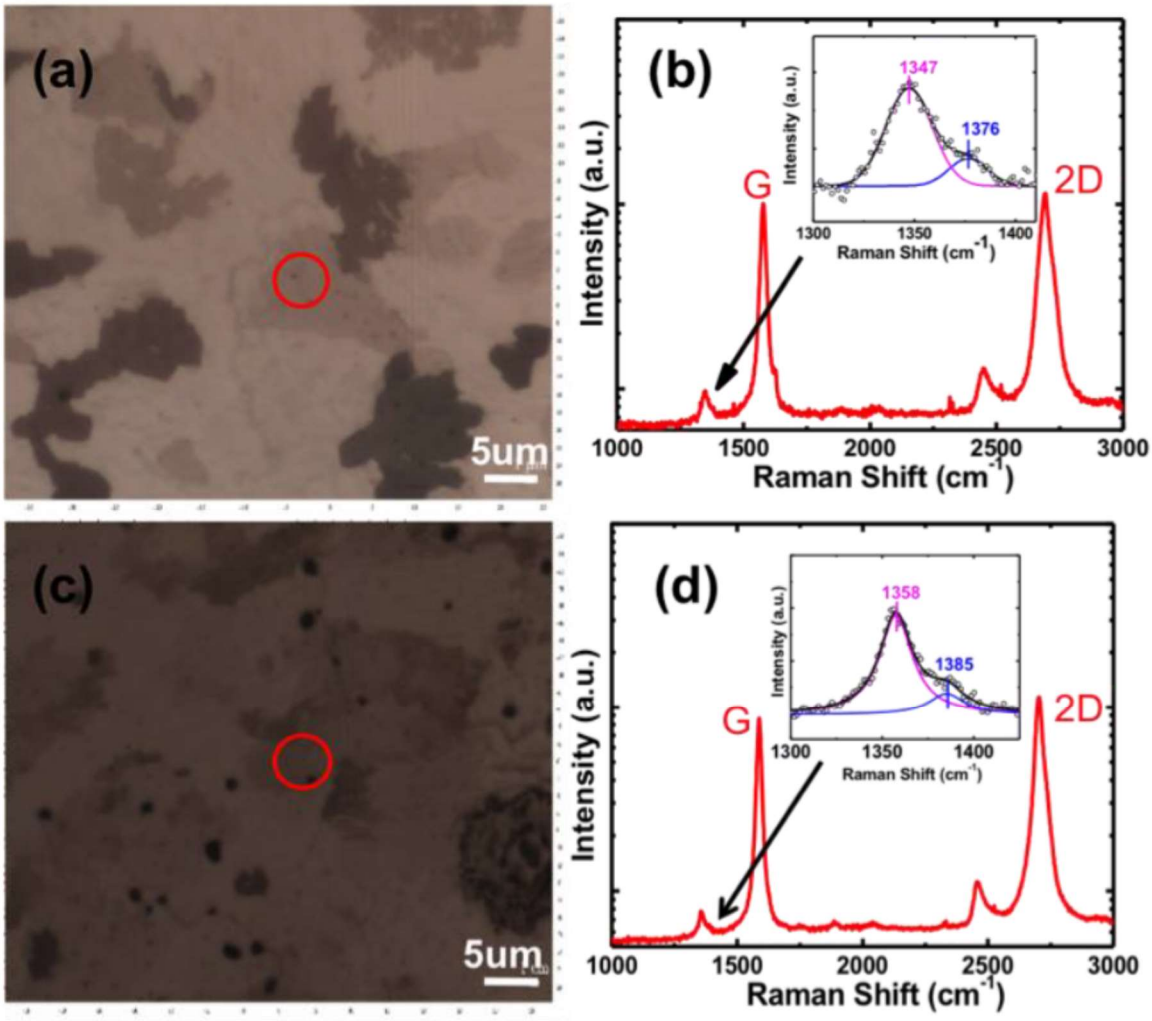

Fig. 3.9 Optical microscopy images and Raman spectra for reference Sample C (a, b) and Sample D (c, d). Raman spectra were measured in the red circle indicated in optical images, respectively.

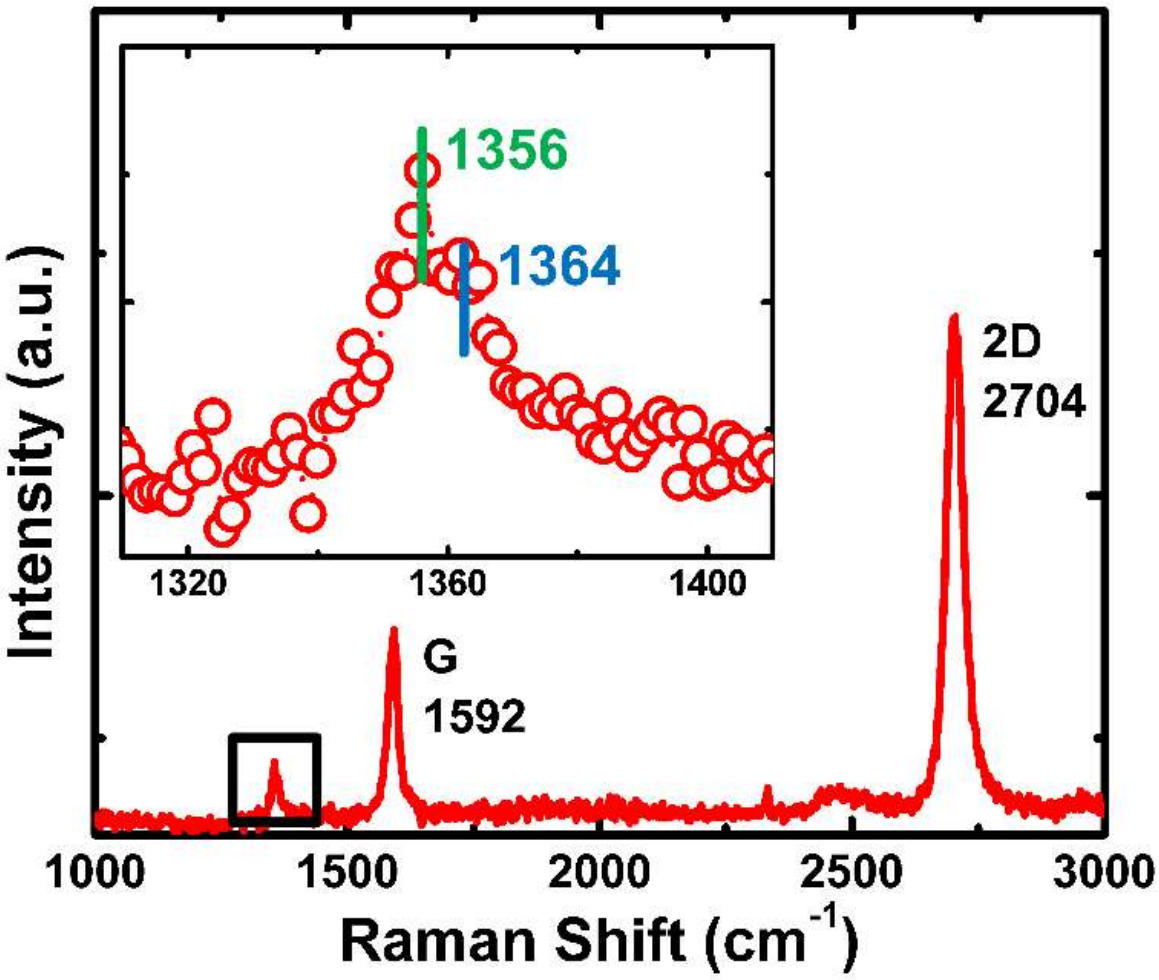

Fig. 3.10 Raman spectrum of graphene/h-BN heterostructure (Sample B). Evident graphene G and 2D peaks are observed, with their intensity ratio indicating 1~2-layer graphene. The inset is enlarged spectrum in the 1300~1400 cm^{-1} region. Two peaks are resolved, relating to graphene D mode and E_{2g} optical phonon peak of h-BN, respectively.

Fig. 3.10 shows Raman spectrum of sample B. Three evident peaks are observed from the spectrum. When we zoom into the peak lying at 1356 cm^{-1}, the data is plotted in the inset. The appearance of D peak has been observed in other reports of graphene/h-BN heterostructure [96]. In addition, an h-BN E_{2g} optical phonon peak is evident at 1364 cm^{-1},

which indicates existence of h-BN. Besides that, graphene G and 2D peaks located at 1592 cm^{-1} and 2592 cm^{-1} are observed. The G/2D peak ratio indicates the grown graphene has thickness of single-/bi-layer. Analyzing the 2D peak of graphene to detect the mismatch angle of graphene and h-BN has been reported recently [97]. In this experiment, the FWHM of the 2D peak of as grown sample is 38 cm^{-1}, which indicates the mismatch angle is below 1º. This self-assembled well-aligned heterostructure growth method shows a huge advantage in time and work consumption compared with mechanical exfoliation method, which has to use microscopy to locate sample and achieve alignment.

Fig. 3.11(a) shows an XPS survey scan spectrum, with the peaks of interest circled. Fine scans were performed in these sites and evident energy peaks for B, C, and N were observed. Fig. 3.11 b, c and d show XPS spectrum of B1s, C1s, and N1s state, respectively. C1s peak is observed at a position of 284.5 eV, which is smaller than environmental C1s peak in XPS, and is closer to the sp2 C-C bond at 284.0 eV [98]. This is an indication of graphene. B1s and N1s exhibit an energy position at 398.0 eV and 190.6 eV, respectively, which are typical characteristics of h-BN [99]. Based on integrated peak intensity and corrections, B/N ratio was estimated to be 1.1 from the surface of h-BN, indicating that h-BN is slightly B-rich.

Fig. 3.12 shows results of plan-view TEM measurement together with selective area electron diffraction (SAED) of the transferred graphene/h-BN heterostructure. The film was prepared using PMMA transfer method. After spin coated with PMMA (4000 rpm for 40 s), sample was baked on the hot plate at 100 °C for 10 min. After that, sample was submerged in 5% $FeCl_3$ solution to etch away the metal layer. With assistance from PMMA

supporting layer, the film was off from Co and floating on the solution after one day etching. Then we used SiO_2 wafer to transferred the film onto carbon coated Cu TEM grid. With leaving the grid at room temperature for one to two days to fully remove water, then we treat it with acetone, IPA and water to remove PMMA. After drying the grid again, it is ready to do TEM on the transferred film.

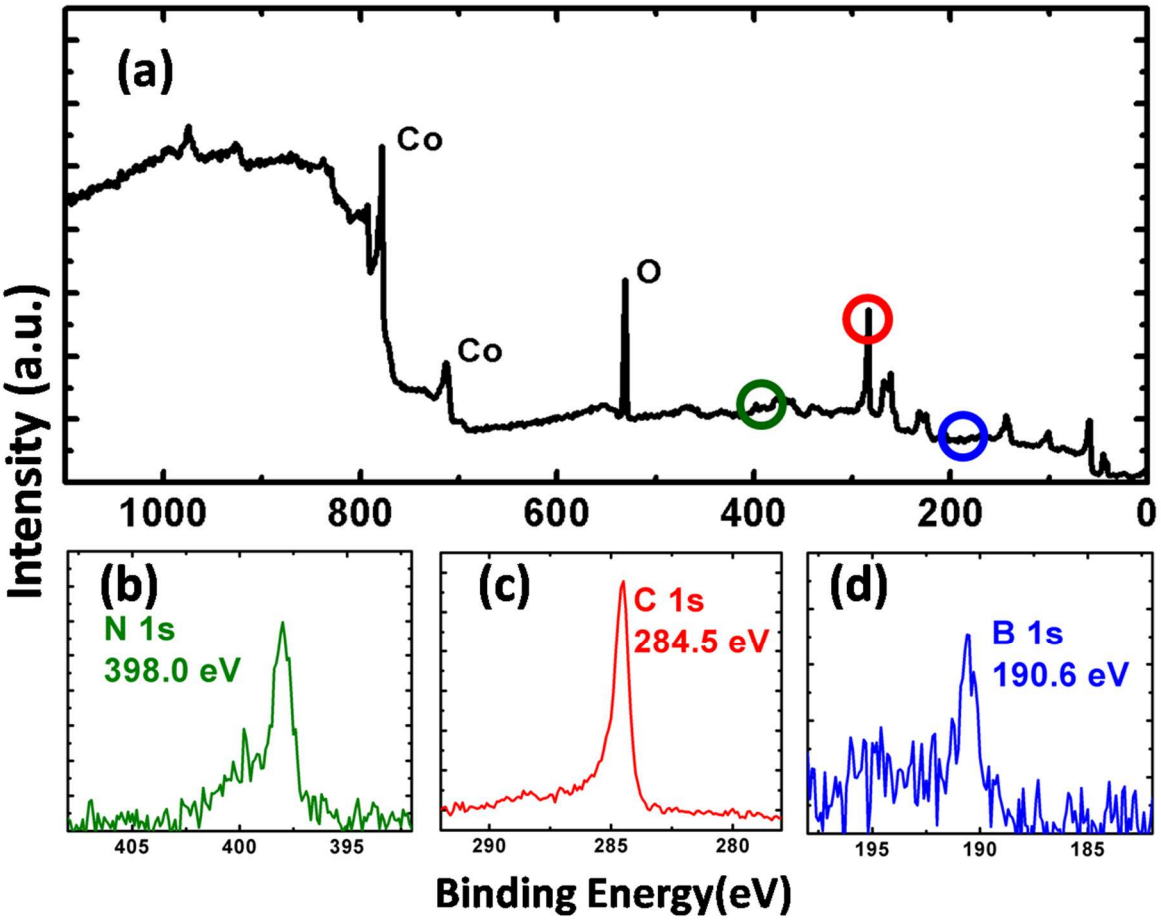

Fig. 3.11 XPS spectra of graphene/h-BN heterostructure on Co substrate (Sample B). a) the survey spectrum, b) N1s peak, c) C1s peak, and d) B1s peak. B1s and N1s are at 190.6 eV, and 398.0 eV, respectively, indicating the existence of h-BN. C1s peak is at 284.5 eV, indicating the presence of graphene.

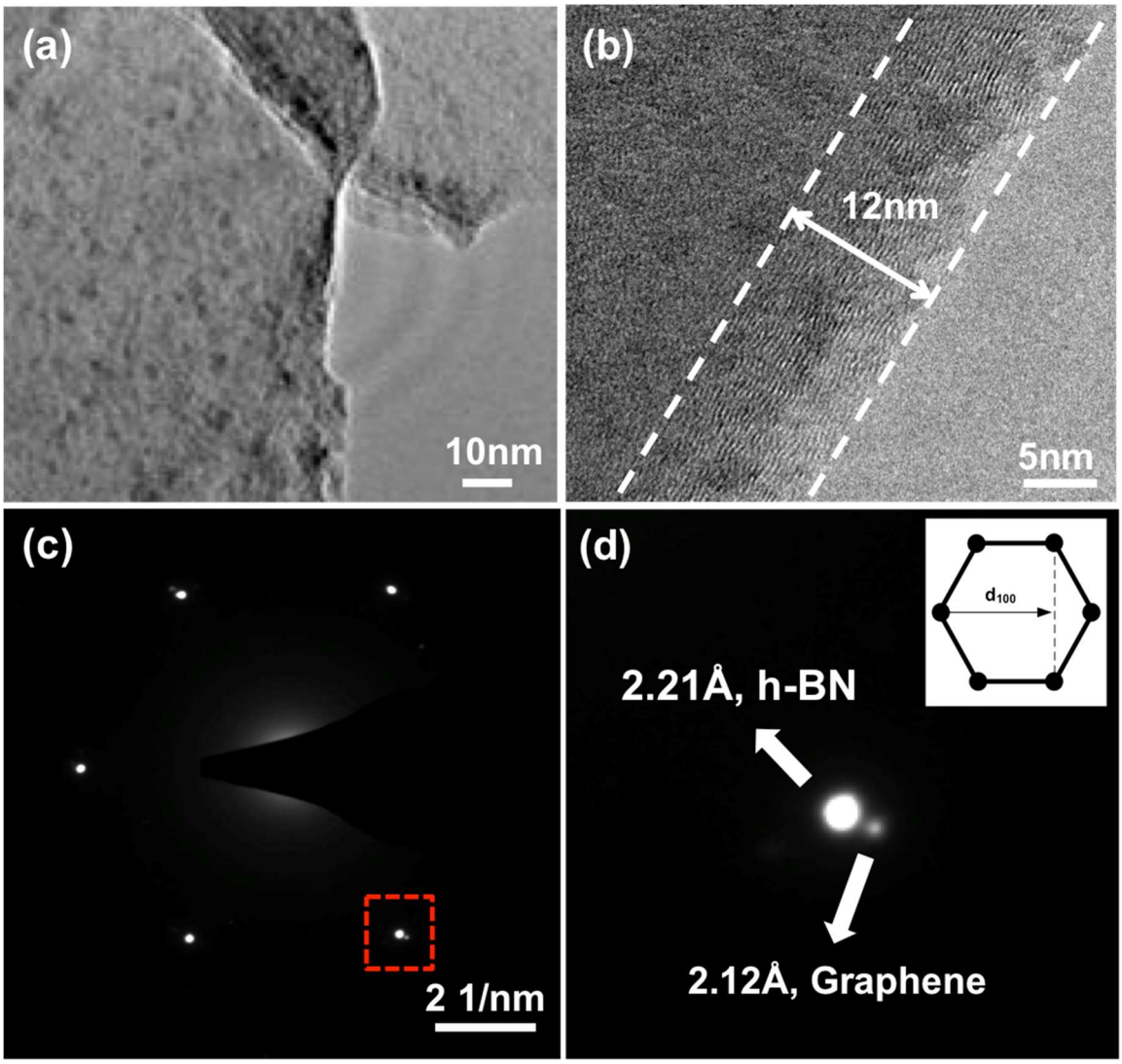

Fig. 3.12 (a), (b) Plan-view TEM image of transferred graphene/h-BN heterostructure (Sample B). (c) SAED pattern of Sample B. Diffraction patterns with six-fold symmetry are observed. (d) Enlarged image of the red square area marked in Fig. 3.12 (c). Two diffraction spots are observed, revealing the (100) plane distance of 2.21 Å and 2.12 Å, which matches h-BN and graphene lattice constants, respectively.

As shown in Fig. 3.12 (a), continuous thin film is observed with some edges folded. Black spots observed mainly originate from PMMA residue during film transfer process.

When a high magnification TEM imaging is done on the folded edge (Fig. 3.12(b)), lined pattern is observed which is because of the layered structure of graphene and h-BN. The thickness of the graphene/h-BN heterostruture can be measured from the edge, which is ~12nm at this specific location.

Fig. 3.12(c) and (d) show selected area electron diffraction (SAED) pattern of the plan-view graphene/h-BN heterostructure thin film. A clear hexagonal set of diffraction spots is observed. A second set, which has weaker intensity and larger diffraction angle, is also seen, shown in Fig. 3.12(d), which is a zoom-in image of the area marked with a red square. Two sets of diffraction spots are clearly observed, which correspond to the electron diffraction from (100) planes of h-BN and graphene. The calculated interplanar spacings corresponding to the two spots are 2.13 Å and 2.06 Å, which match well with expected numbers for h-BN and graphene, respectively. The strong intensity of h-BN diffraction pattern may indicate a well-aligned, multi-layer h-BN. There is a small rotation (<1º) observed between the two sets, similar to other reports on graphene/h-BN heterostructures [100], which also matches our conclusion from Raman studies.

Fig. 3.13 shows a cross-sectional TEM image of the heterostructure with different magnifications. The sample was prepared using focused ion beam (FIB) technique. The graphene/h-BN thin film was covered by an iridium (Ir) layer and further protected by electron-beam and ion-beam deposited platinum (Pt) layers during TEM specimen preparation. Lattice fringes are observed in the 15nm thick band. The inter-fringe distance is 0.33nm, measured from Fig. 3.13 (d), which is in close agreement with the out-of-plane lattice constants of h-BN and graphene.

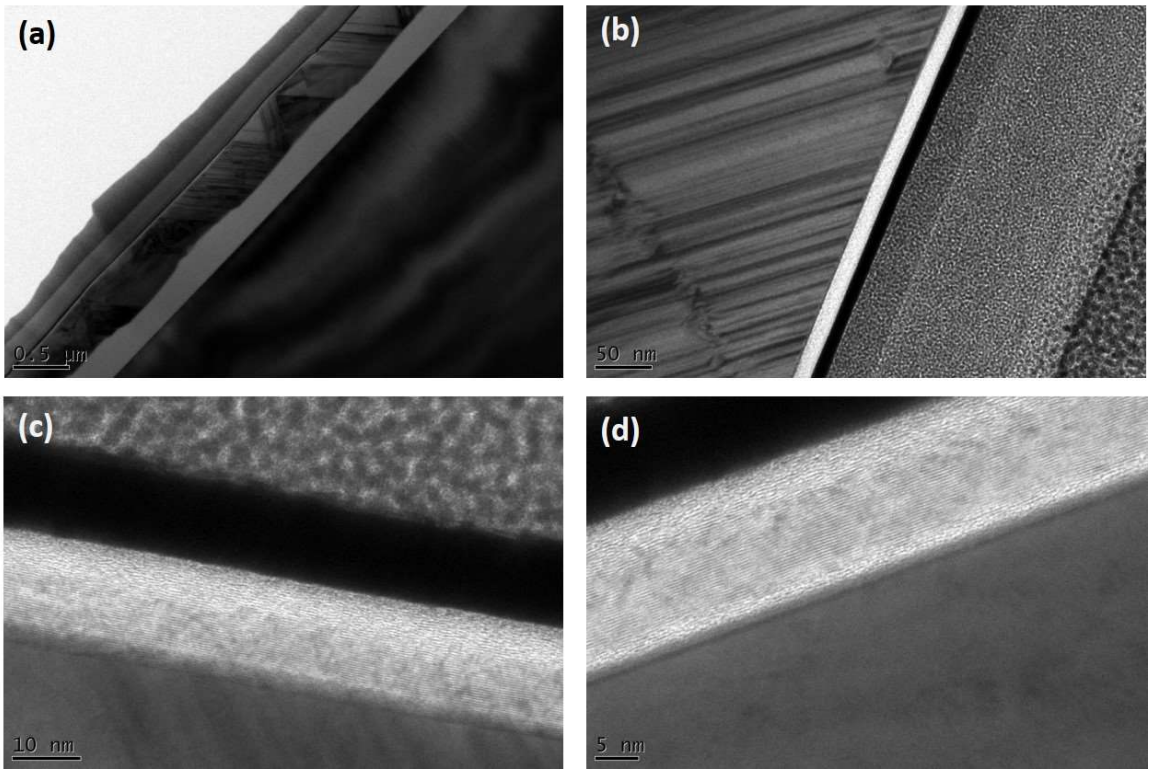

Fig. 3.13 Cross-sectional TEM images of transferred graphene/h-BN heterostructure (Sample B) at different magnifications.

To analyze electrical properties of the heterostructure, a transistor device was fabricated as shown in Fig. 3.14(a). The process is as follows: After the film was transferred onto an oxidized silicon substrate with a 300 nm SiO_2 layer, photoresist was spun onto the film and photolithography was done to create the pattern. Then, SF_6 gas was used to etch unprotected h-BN and graphene to expose the edge of the heterostructure. After that, a 10/70 nm Ti/Au contact was deposited. Fig. 3.14 (b) shows an optical microscopy image of the device. The channel length is 1mm and channel width is 5 mm. Figure 3. 14 (c) and (d) show I_D–V_G transfer characteristics and I_D-V_D characteristics of the transistor device, respectively. The mobility is then extracted from the linear regime of the transfer

characteristics. For a typical transistor device, its mobility was found to be around 101 cm^2 V^{-1} s^{-1}. The present relatively low mobility may mostly originate from the device fabrication process. For example, h-BN was grown on top of graphene, which may not have improved the performance of graphene underneath too much.

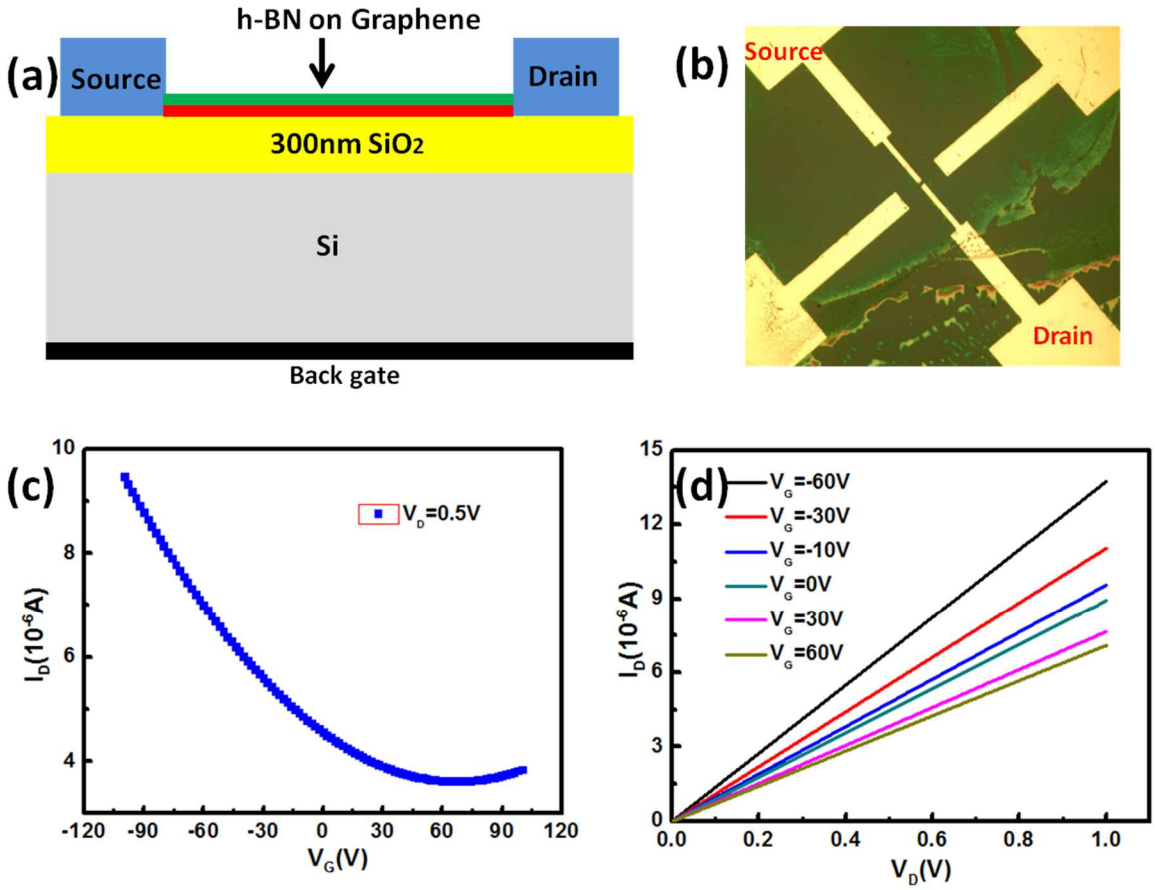

Fig. 3.14 Device fabrication and electrical measurement on the transferred film.

3.5 Conclusion

In this chapter, we have demonstrated direct epitaxial growth of h-BN on graphene utilizing MBE. Signature triangular h-BN flakes with sizes as large as 20 μm were observed. Further improvement on the growth condition results in high-quality wafer-scale graphene/h-BN heterostructure film. The epitaxial single/bi-layer graphene/few-layer h-

BN structure is further confirmed by XPS, Raman spectroscopy, electron diffraction, and TEM imaging. The misorientation between the graphene and h-BN layers is less than 1°. While MBE synthesis of high-quality graphene/h-BN heterostructures is a critical step toward the realization of 2D electronics, reasonable electronic functionality of heterostructures is of greater concern. We fabricate a device to demonstrate the basic electric property of the heterostructure. In the future work, two- and three-terminal devices will be fabricated and the electrical measurements will be carried out to evaluate their electrical performance.

Chapter 4 Low-temperature growth of graphene on iron substrate by molecular beam epitaxy

4.1 Overview

As discussed in previous chapters, graphene has attracted a great deal of interest due to its fascinating properties and a wide variety of potential applications. Several methods have been used to achieve high-quality graphene films on different substrates. To date, various transition metals have been used as templates or substrates for high-quality graphene synthesis. Compared with other metals, such as Cu [128], Ni [138], Co [29], Pt [47], there are very few reports about graphene growth on iron (Fe) [102-104], which is the most widespread transition metal. The main reason could be the challenging procedure of graphene growth on Fe due to its higher chemical reactivity. In addition, its growth mechanism, which may correlate with the complex Fe-C phases (shown in Fig. 4.1), remains elusive.

Transition metals	Growth mechanism	Carbon solubility at ~1000C	Max size graphene up to date
Ru	Bulk-mediated	0.34 wt. %	In research scale
Ir	Bulk-mediated	0.041 wt. %	In research scale
Pt	Under debate	~3.1E-4-0.0043 wt. %	In research scale
Cu	Surface-mediated	~7.4E-4-0.008 wt. %	23″ x 300″
Ni	Bulk-mediated	~0.6 wt. %	2″x 4″
Co	Bulk-mediated	~0.9 wt. %	1″x1″
Fe	Bulk-mediated	~0.02 wt.% @ 723C Maximum ~2.5 wt.%	High-quality not achieved

Table 4.1 Different metal substrates used for graphene growth.

Table 4.1 lists part of metals which have been used for substrates of graphene growth. Based on different carbon solubility in different metals, there are two growth mechanisms studied here: bulk-mediated and surface mediated. We have already shown that Cu and Co can be used for vdW materials growth in MBE chamber, which usually needs high growth temperature. Compared with other metals, Fe has higher carbon solubility, which will have more carbon dissolved in the metal during the growth and might lead to lower growth temperature. And the complex Fe-C diagram also offers versatility for engineering graphene layer numbers.

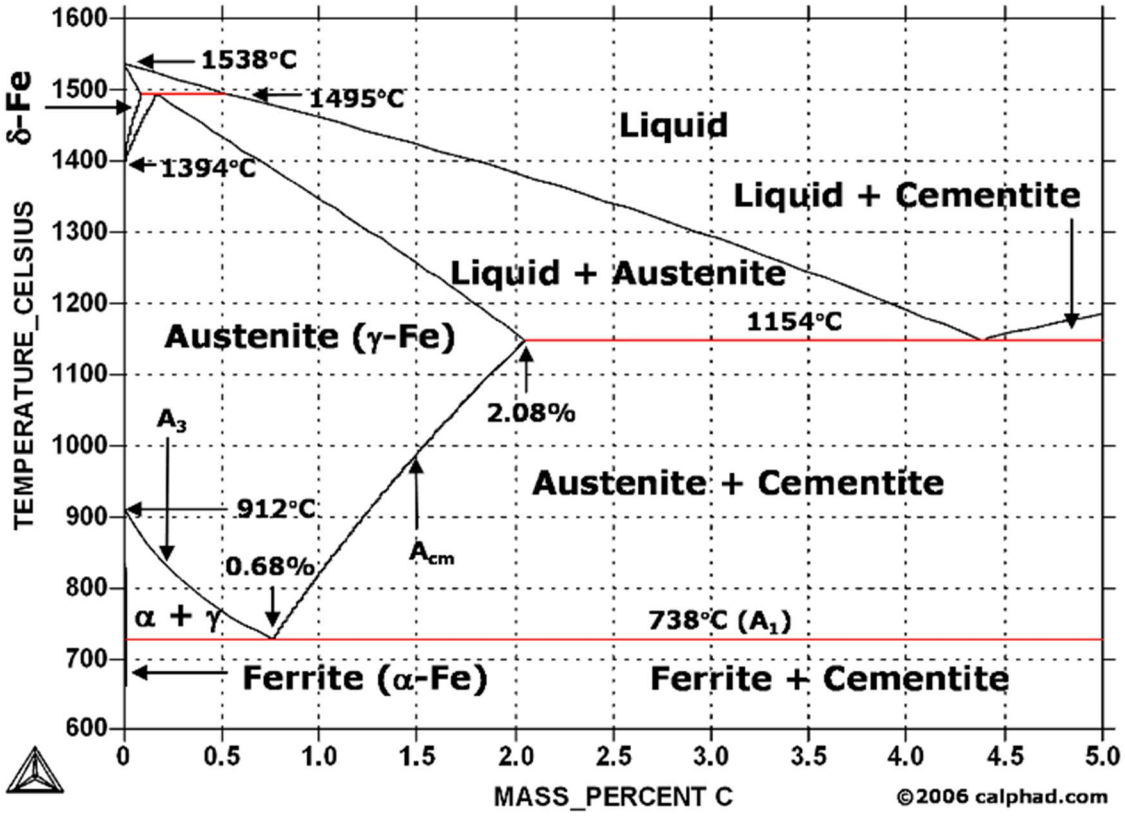

Fig. 4.1. Fe-C phase diagram showing which phases are to be expected at metastable equilibrium for different combinations of carbon content and temperature. (adapted from calphad.com)

In this chapter, we demonstrate low-temperature growth of high-quality, large-area graphene thin films on Fe substrates by gas-source MBE. Two-dimensional (2D), large-area graphene samples were grown on Fe thin films, and characterized by Raman, X-ray photoelectron spectroscopy, X-ray diffraction, optical microscopy, transmission electron microscopy and atomic force microscopy. It is found the optimized large-area graphene growth temperature is relatively low between 500 °C and 550 °C. Unique mechanism involving the formation/decomposition of iron carbide (Fe_xC_y) is responsible for the growth of graphene on Fe, in contrast to precipitation of C atoms without involving metal carbides from other metals. The formation of graphene by involving the chemical reaction between Fe and C rather than temperature-sensitive physical precipitation process enables precise control of the thickness of the film because the reaction of Fe and C can be well controlled at certain temperature, compared with drastic wide-range temperature change requirement for the precipitation growth of graphene on other metals. Moreover, the reaction of Fe and C can occur at relatively low temperature (graphene flakes can be grown on Fe at a growth temperature as low as 400 °C), leading to low-temperature synthesis of graphene. Thus, this work not only elucidates the mechanism of graphene growth on Fe but also provides a convenient route to achieve scalable epitaxial graphene films for those applications that can only sustain moderate- and low-temperature processes. The result in this chapter has been published in [132].

4.2 Materials and growth method

A Perkin-Elmer MBE system was used for graphene growth. Acetylene gas (C_2H_2, Airgas, 99.9999%) was connected to the MBE chamber as a C source and the flow rate

was tuned by a mass flow controller (MFC). H_2 gas (Airgas, 99.9999%) was also introduced to the chamber by a needle valve during the process when necessary. The Fe film of 300 nm was grown on a SiO_2/Si wafer by an e-beam evaporator and used as substrate. After the substrate was transferred to the growth chamber, the substrate was heated to a targeted growth temperature between 250 °C and 800 °C at a rate of 10 °C/min and annealed for 10 minutes. During the annealing process, 10 sccm H_2 was introduced into the chamber to remove possible iron oxide and suppress evaporation of Fe. After that, H_2 flow rate was decreased to 6 sccm, and the graphene growth started by the introduction of 2-5 sccm acetylene. During the growth, the pressure was usually between ~1×10^{-4} and 1×10^{-5} torr depending on the source flow rates. The growth lasted for 2 minutes. After the growth, the sample was slowly cooled to room temperature at a rate of 10 °C/min.

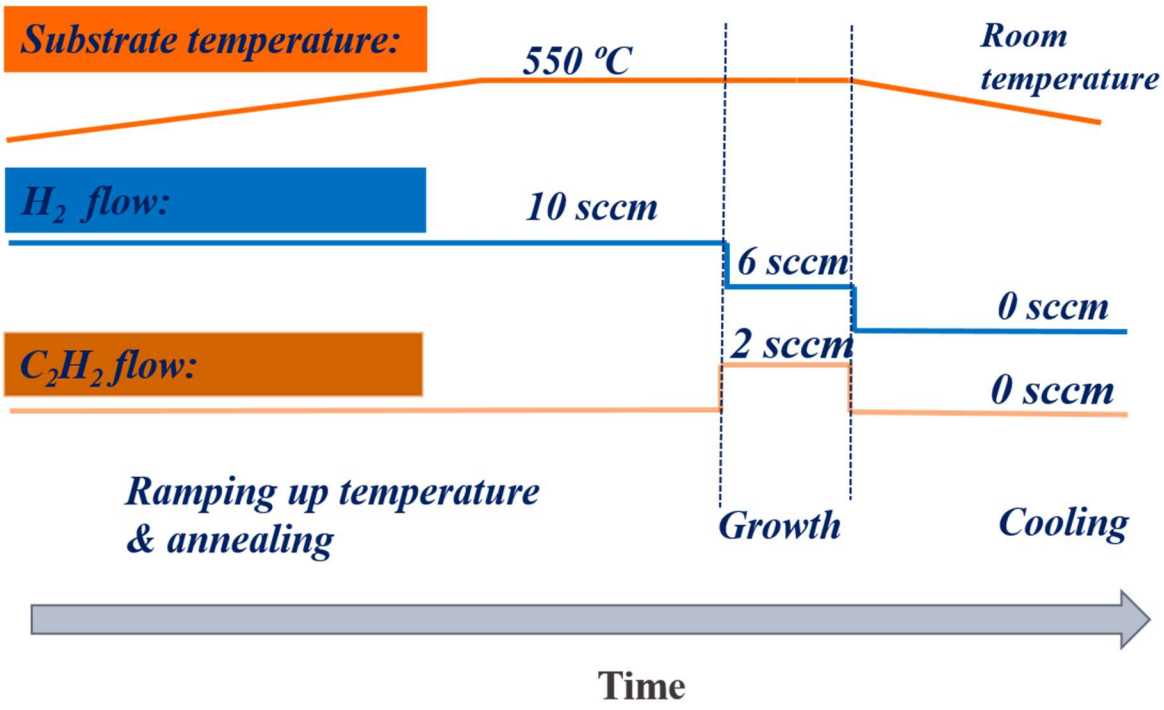

Fig. 4.2 Schematic of a typical graphene growth on Fe by MBE

After growth, graphene surface becomes rough as shown in Fig. 4.3. Before growth, the substrate RMS is 1.03 nm, which is at reasonable range of e-beam evaporation growth. After grown, the surface became very rough with RMS increased to 13. 18 nm at 2 um scale due to heat effect on Fe.

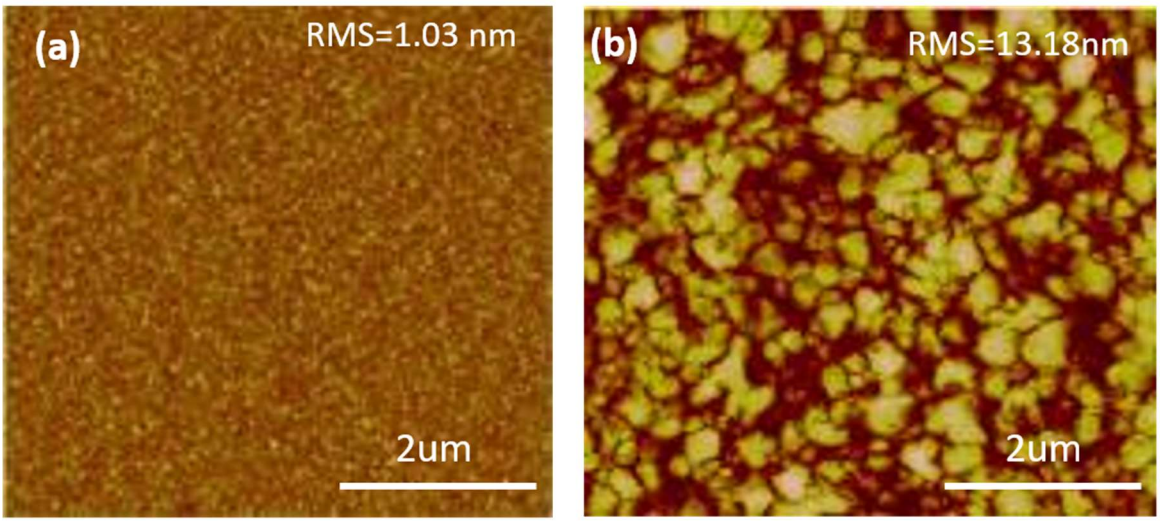

Fig. 4.3 AFM of sample (a) before and (b) after growth.

4.3 Characterization methods and analysis of graphene growth on Fe

Optical microscopy and Raman characterization were performed using a HORIBA LabRAM system equipped with a 50-mW 514-nm green laser. X-ray photoelectron spectroscopy (XPS) characterization was carried out using a Kratos AXIS ULTRA XPS system equipped with an Al Kα monochromatic X-ray source and a 165-mm mean radius electron energy hemispherical analyzer. X-ray diffraction (XRD) spectra were measured with a Bruker APEX system. Cross-sectional transmission electron microscopy (TEM) image was obtained by an FEI/Philips CM20 system, and plan-view TEM image was acquired by an FEI Tecnai12 system. Atomic force microscopy (AFM) characterization

was performed using a Veeco Dimension 5000 system. Some characterizations were done on transferred graphene films, which were removed from Fe substrates by etching of substrate in $FeCl_3$ solution and the assistance of a polymethyl methacrylate (PMMA) coating layer.

Fig.4.4 shows a typical Raman spectrum of graphene grown on Fe at 550 °C, in which graphene signal can be detected with graphene G and 2D peaks. Additionally, the G (1594 cm^{-1})/2D (2709 cm^{-1}) ratio is 1.1, indicating that the as-grown film is few-layer graphene, which need to be further improved to achieve single- or bi layer graphene. D peak located at 1350 cm^{-1} is also seen in the spectrum, indicating that defects exist in the graphene film grown at 550 °C. [105]

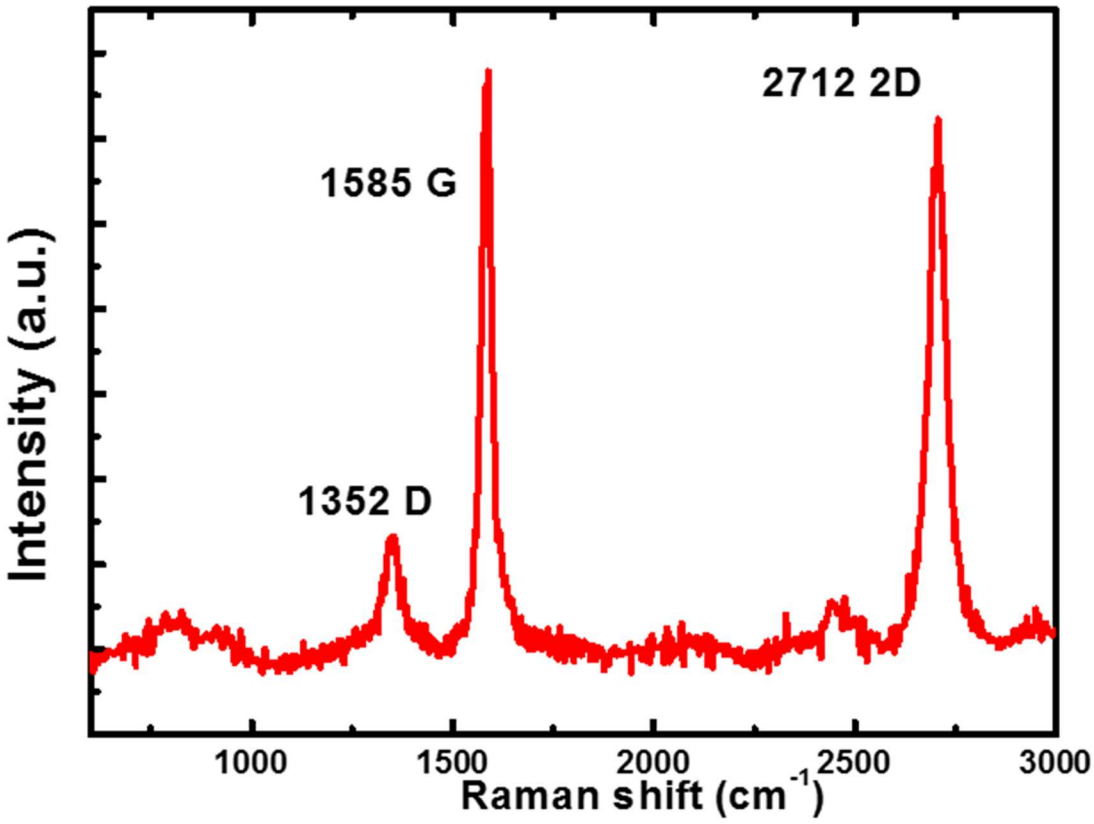

Fig. 4.4 Raman spectrum of graphene grown on Fe, the growth temperature is 550 °C.

Raman mapping is also carried out and the result for the 550 °C sample, is shown in Fig. 4.5. Graphene signal is always detected over the mapping area 40 μm * 40 μm of the sample. Mapping is measured with respect to the intensity of the G peak, which provides graphene thickness information. From the mapping result, most area is uniform in the thickness (green color), and some area is thicker (red color). It is consistent with the optical microscope imaging results, namely, the as-grown graphene is uniform at most areas with darker spots representing thicker film.

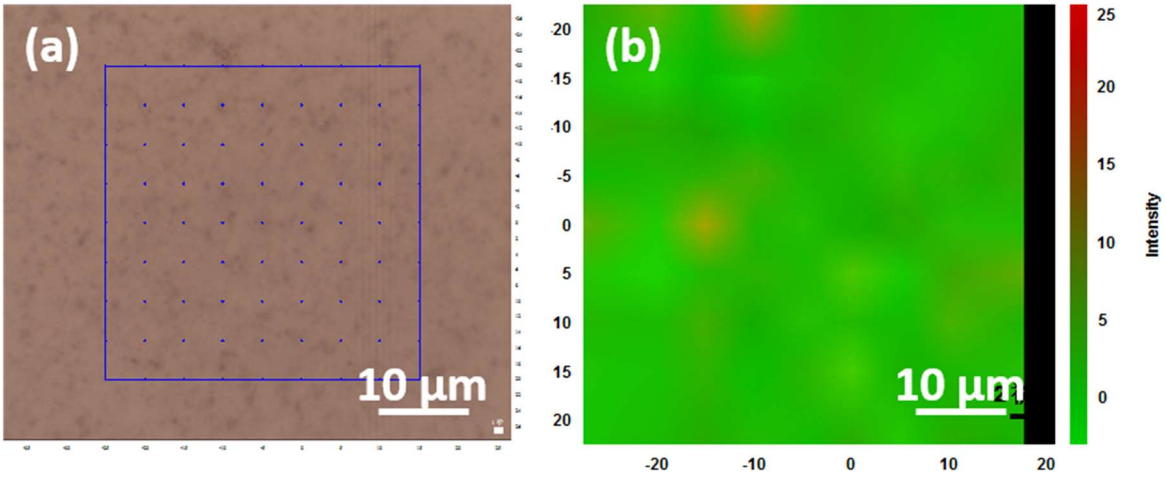

Fig. 4.5 Raman G peak intensity mapping of graphene grown on Fe.

With local flatness shown in the center area, the graphene is non-uniform when measured over large scale. As shown in the optical images and Raman spectrum of Fig. 4.6, A, B are measured at center area while C, D are measured at edge area. Center area provides thinner graphene film compared with edge area, which is mostly due to higher temperature at the edge area. What's more, more condensed and larger black domain can be observed at edge area of the film, which is possibly due to unbalanced temperature distribution and over-heated temperature at edge area. From all of these, the importance of

temperature on graphene growth with Fe substrate has been proven and will be studied in details later.

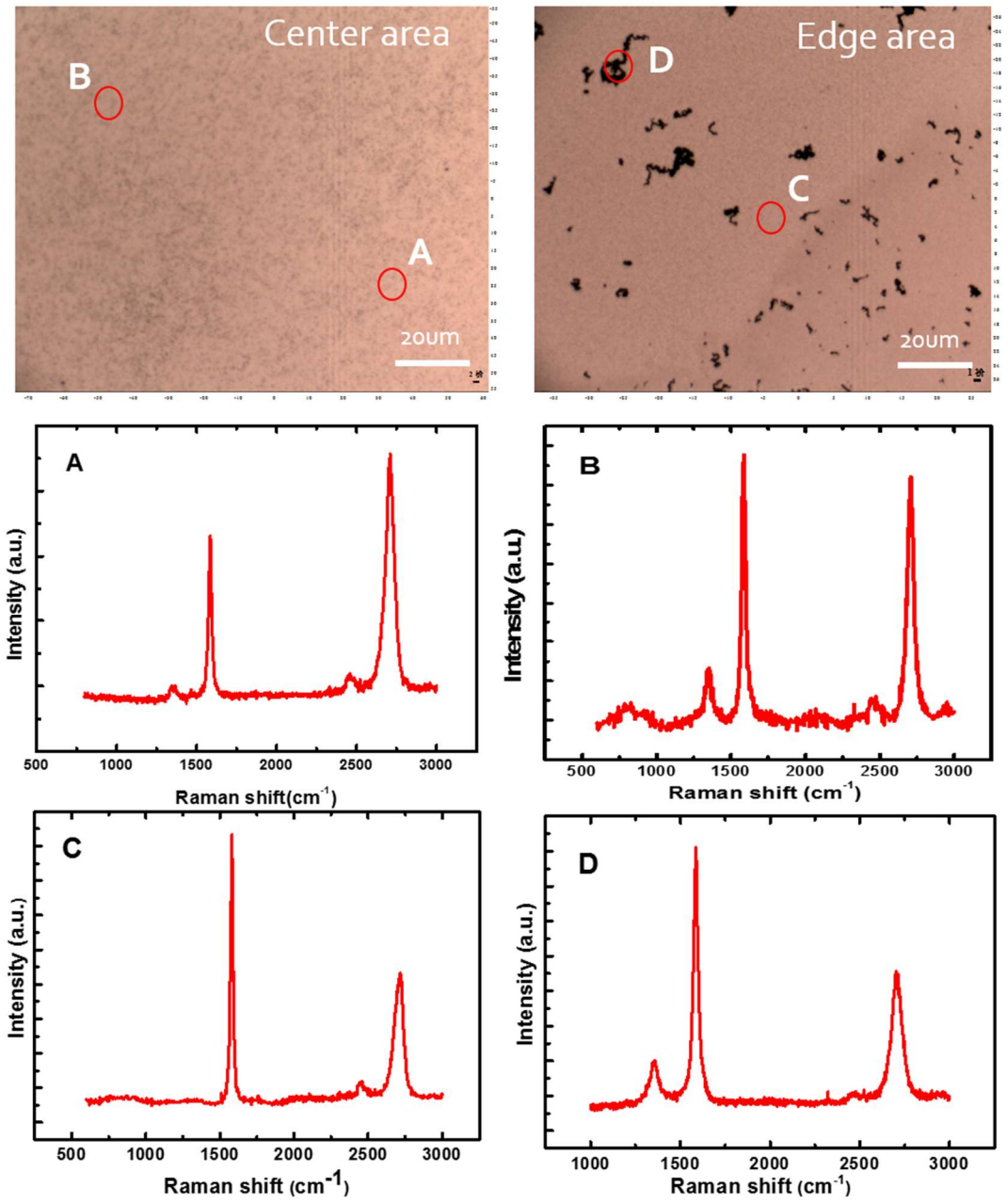

Fig. 4.6 Different optical microscopy and Raman signals achieved at center and edge of graphene. A, B are measured in the same center area, while C, D are measured at the edge area.

Fig. 4.7 shows XPS spectrum of the graphene sample grown at 550 °C. Graphene-like C sp^2 peak is located at 284.8 eV, and C-O peak (288.3 eV) is also observed [106], which is synthesized in carbon groups. In addition, Different Fe bonds are detected: Fe 2p 3/2 and 2p 1/2 peaks [107]. With these different phases of Fe, high-quality graphene film can still form on Fe, further indicating that the chemical reaction of C and Fe has played an important role in the formation of graphene.

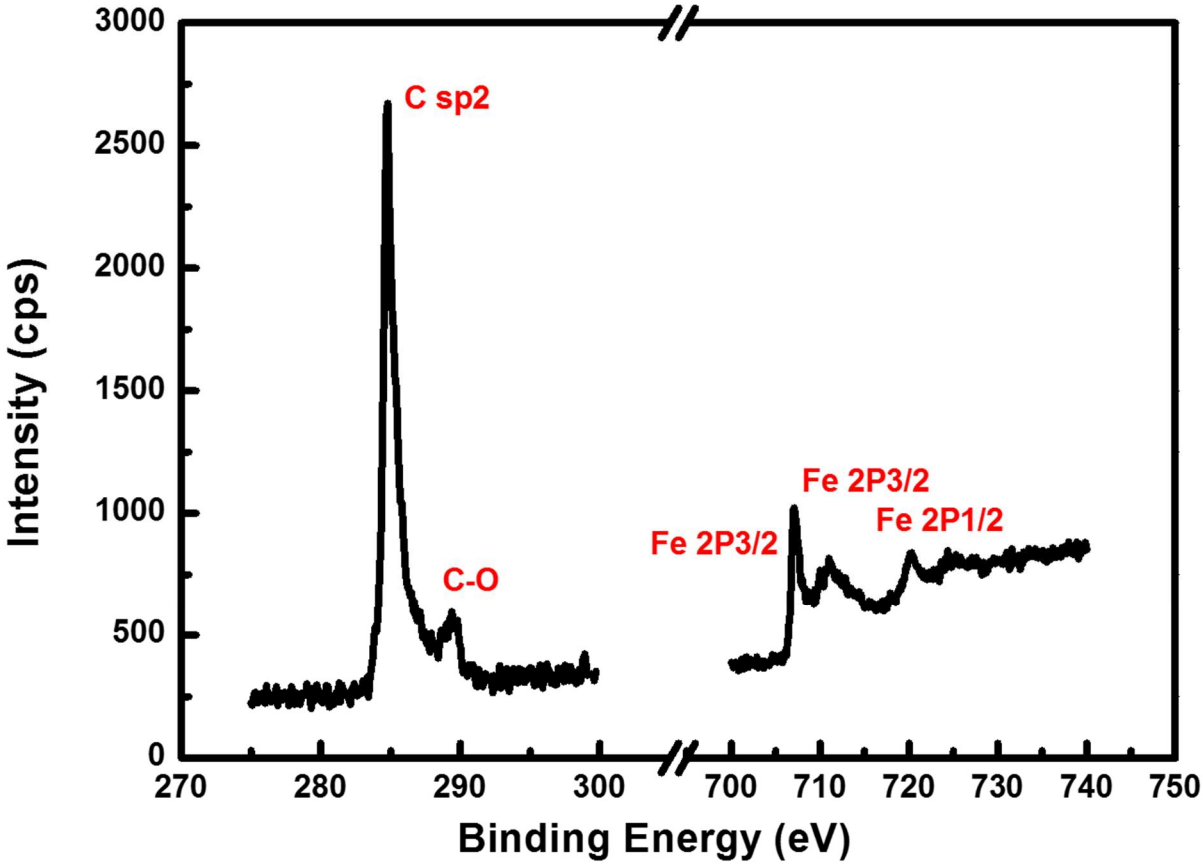

Fig. 4.7 XPS spectrum of graphene sample grown on Fe at 550 °C. Carbon group C sp^2, C-O peak, Fe group: Fe 2p 3/2, and Fe 2p 1/2 peaks are mainly detected, which indicates existence of oxides of polycrystalline Fe.

4.4 Graphene at different growth temperatures

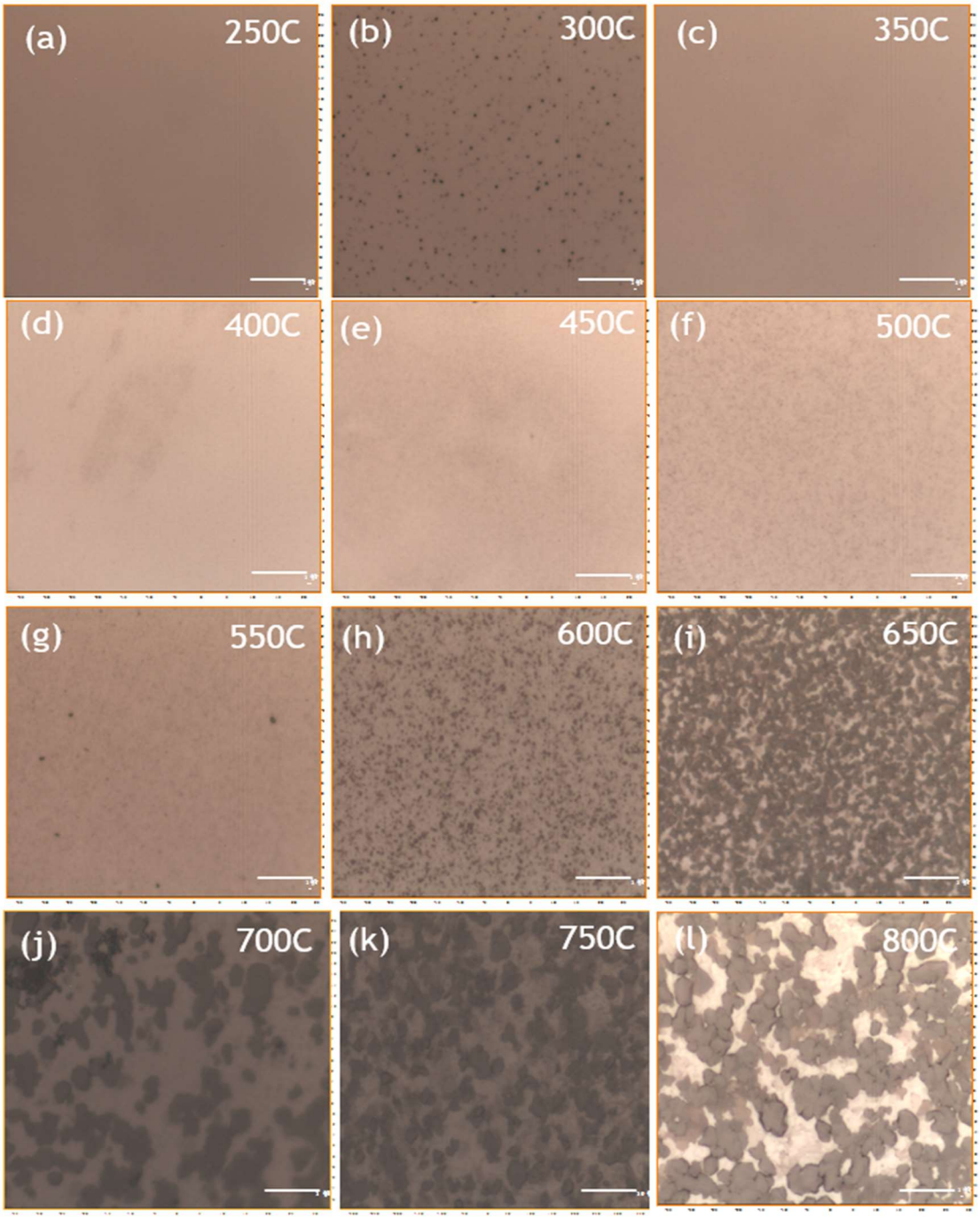

Fig. 4.8 (a)-(l) Optical microscopy images of graphene samples grown on Fe at different substrate temperatures. As temperature is below 350 °C, there is no obvious growth.

Graphene flakes are seen at 400 °C, and keep enlarging with the increase of temperature. As temperature is between 500 °C and 550 °C, the Fe substrates are fully covered by uniform graphene films. As temperature is over 600 °C, condensed graphite grains are observed. The scalebar is 10 um.

To find temperature dependence of graphene growth, a set of optical microscopy images of as-grown graphene samples on Fe substrates at growth temperatures between 250 °C and 800 °C with a step of 50 °C, the optical microscopy images of grown sample is shown in Fig. 4.8. Significant change in morphology of graphene films is observed. At low growth temperatures (≤350 °C), no film is visible. Starting from 400 °C, graphene flakes are formed and enlarged with the increase of the growth temperature. Graphene film extends to cover the whole substrate as the growth temperature reaches 550 °C. From 600 °C, graphene films can still be seen, however, condensed graphene domains start to appear randomly. The domains become larger and thicker with the increase of growth temperature. It should be noted that micrometer-sized graphene flakes are grown at a growth temperature as low as 400 °C, and large-area continuous graphene films on Fe are achieved at growth temperature of 500~550 °C, while much higher growth temperature is required to form graphene on other metal substrates (Cu, Co, etc.)

A detailed Raman analysis of sample grown at different temperatures is shown in Fig. 4.9. (Raman was measured at center area of each sample) Fig. 4.9 (a) shows G/2D ratio and (b) shows full width at half maximum (FWHM) of 2D peaks from Raman spectra of the samples grown from 400 °C to 800 °C, respectively. Fig.4.9 (c) shows D/G ratio as a

function of growth temperature, which reflects relative density of defects in the graphene films [108].

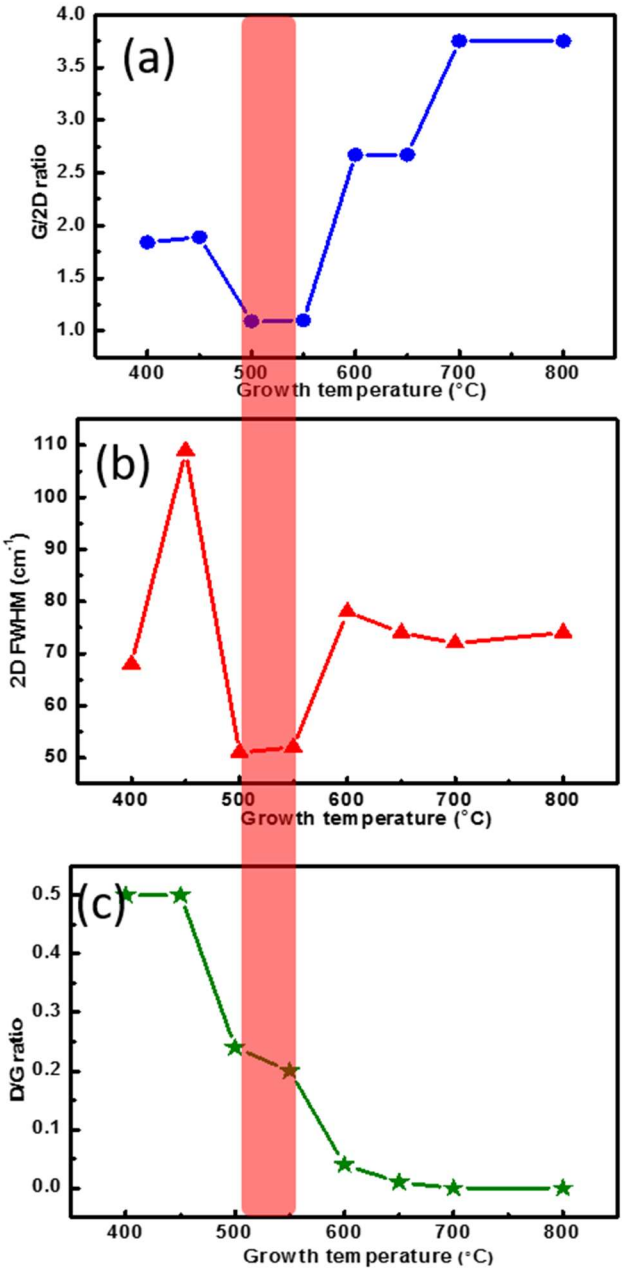

Fig. 4.9 Raman analysis of graphene samples grown on Fe at different temperature. (a) A typical Raman spectrum of a sample grown at 550 °C. The inset is a Raman mapping result of graphene film grown at 550 °C. The mapping area is 40 μm×40 μm. (b) G/2D ratio, (c) FWHM of 2D peak, (d) and D/G ratio as a function of growth temperature for samples grown from 400 °C to 800 °C. The red area indicates optimized growth window.

From Fig. 4.9 (a), the lowest G/2D ratio is ~1 as the growth temperature is between 500 °C and 550 °C, as shown in red region of Fig 4.9. Similar trend is shown in measured FWHM, which reaches its minimum of ~

50 cm^{-1} at the same growth temperature range, indicating again that the graphene film has 2 or a few layers [109]. As seen from Fig.4.9 (c), D peak is always detected as growth temperature is lower than 650 °C, and disappears as the temperature exceeds 700 °C. Similar results of temperature-dependent effect on D peak were also observed for graphene grown on other metals [110-112]. Balancing the thickness and defects, the growth temperature window of graphene on Fe is determined between 500 °C to 550 °C in our MBE system.

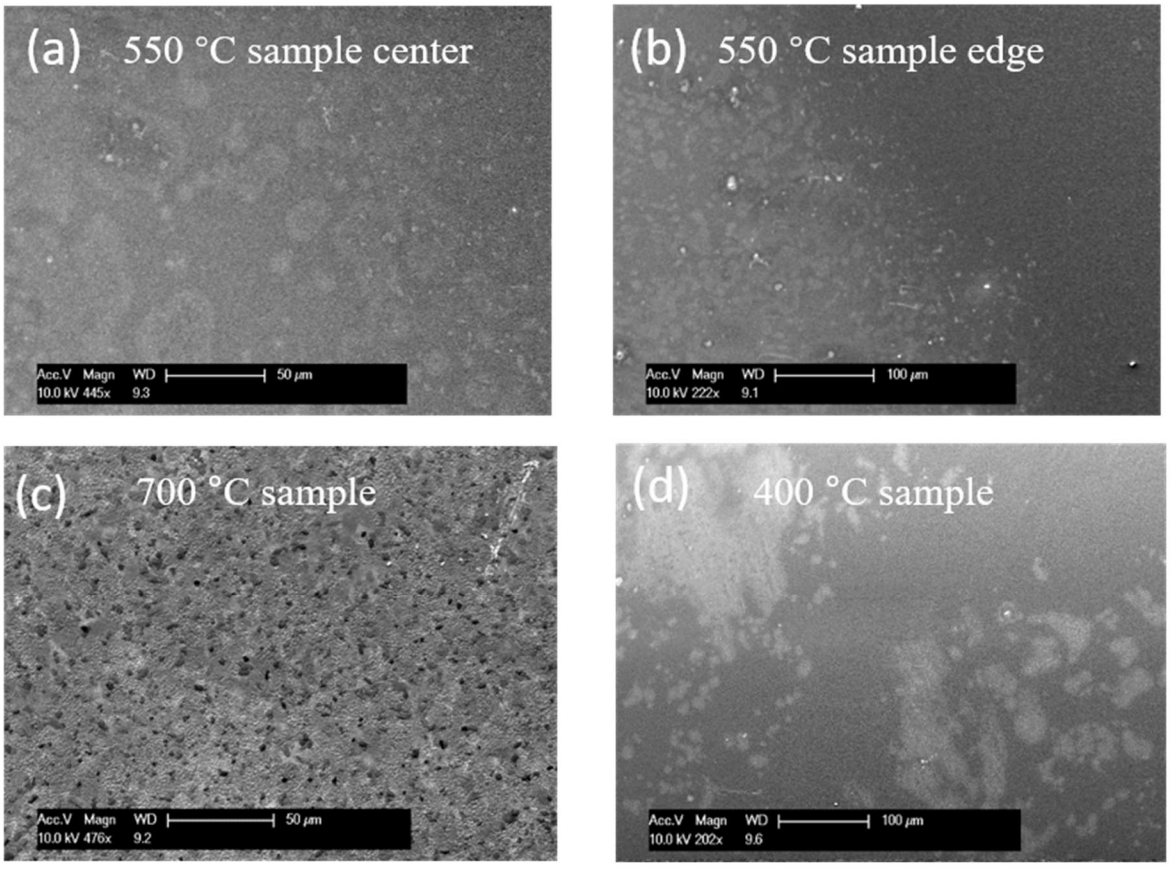

Fig. 4.10 SEM images of some as-grown films, which are grown with different temperature and locations. (a) (b) are samples grown at 550 °C but different locations: center and edge, respectively. (c) is sample grown at 700 °C. (d) is sample grown at 400 °C.

SEM was also performed to find graphene coverage information at different temperatures. As seen in Fig. 4.10, continuous graphene film with locally uniform thickness is evident at the center of 550 °C grown sample. For 400 °C grown sample, only discrete graphene flakes are observed. And thick graphite is observed on 700 °C grown sample. The results are in good agreement with optical microscopy images.

Fig.4.11 gives XRD patterns of graphene samples grown at different temperatures. Fe [110], [200] and [211] peaks are evident in the spectra of all these samples, showing that Fe thin films are polycrystalline [113, 114]. Graphitic signal, which is located at 27.5 2θ diffraction angle [115], is observed for the samples grown at a temperature of 600 °C and higher. The intensity of the graphene peak increases with the increase of temperature. This result is in close agreement with optical microscopy result shown in Fig. 4.8: As the temperature is higher than 600 °C, graphite features form instead of graphene films. 2θ diffraction peaks at 38.2°and 43°are observed for the samples grown between 350 °C and 650 °C, which indicates the existence of various iron carbide Fe_xC_y with different Fe and C mole fractions, including cementite (Fe_3C) [116]. As the temperature is lower than 350 °C, C solubility in Fe is so low that Fe_xC_y cannot be formed. As the temperature is higher than 650 °C, decomposition of Fe_xC_y into Fe and graphite speeds up, which essentially prevents the formation of graphene thin film. Only within a growth temperature window, in this case, 350~650 °C, the formation and decomposition of Fe_xC_y can be balanced to form graphene films. It suggests that the graphene on Fe growth is not a simple layer-by-layer deposition process or C precipitation process, but related to the chemical reaction of C and Fe atoms.

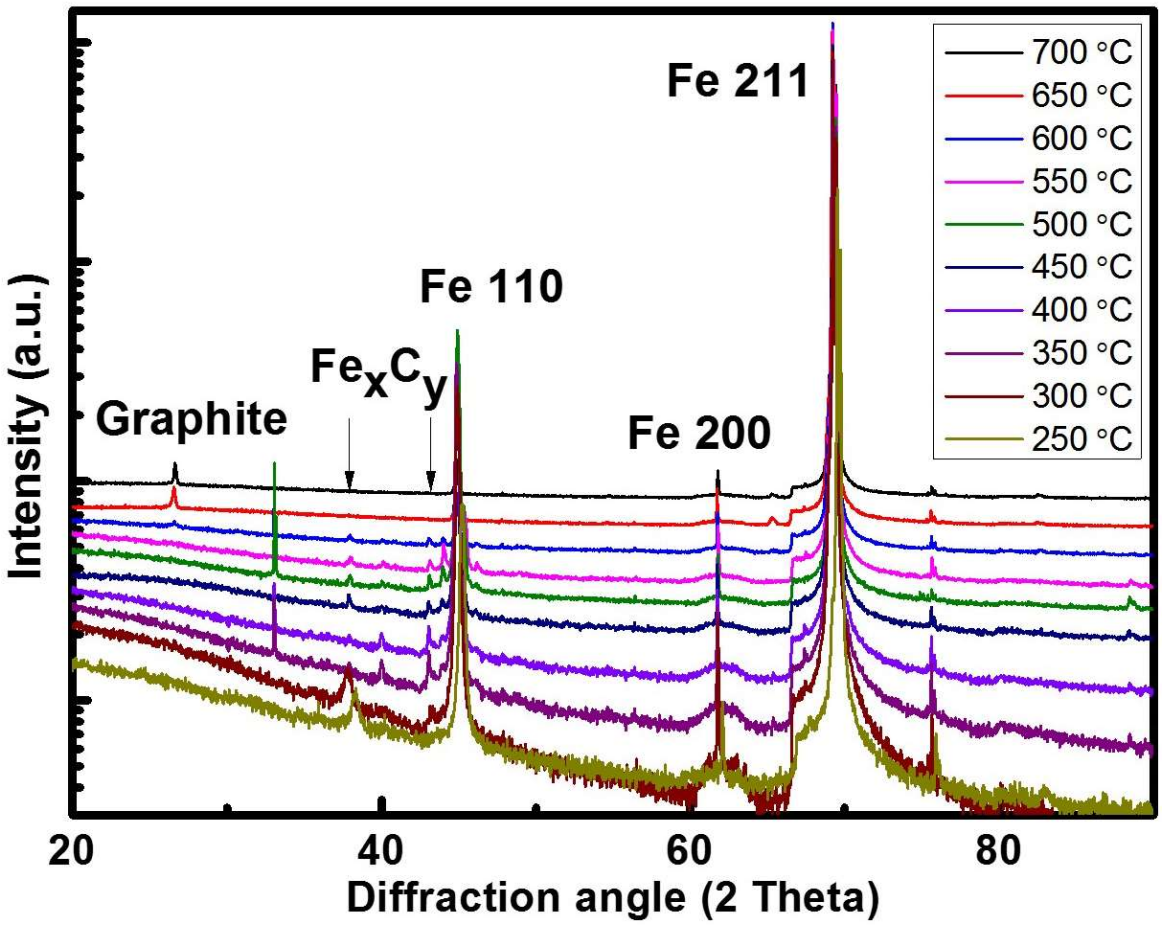

Fig. 4.11 XRD patterns of graphene samples grown on Fe at different temperatures. Graphite signal is detected as growth temperature is higher than 600 °C. Fe_xC_y signal is observed as the growth temperature is between 350 °C and 600 °C.

Fig. 4.12 (a) shows a high-magnification cross-sectional TEM view of a thicker film area. Layered graphene with a measured inter-layer distance of 0.34 nm is evident, which matches out-of-plane inter-layer distance of graphene very well. This is a solid proof to show graphene existence. Fig. 4.12 (b) shows a low-magnification cross-sectional TEM image of the graphene sample grown at 550 °C. The surface of Fe thin film is not flat, which is originated from the heat treatment at the growth temperature. It is evident that a

continuous graphene film grows conformally on the Fe substrate. Nevertheless, the film thickness is not uniform across the surface. Fig. 4.12 (c) shows a plan-view TEM image of the sample grown at 550 ºC. Relatively thin and uniform graphene film with some darker spots representing thicker areas is observed. The inset image shows a clear selected area electron diffraction (SAED) pattern, leading to a calculated A-plane distance of 0.211 nm, which is in good agreement with the theoretical value of graphene. It shows that graphene is of highly-crystalline.

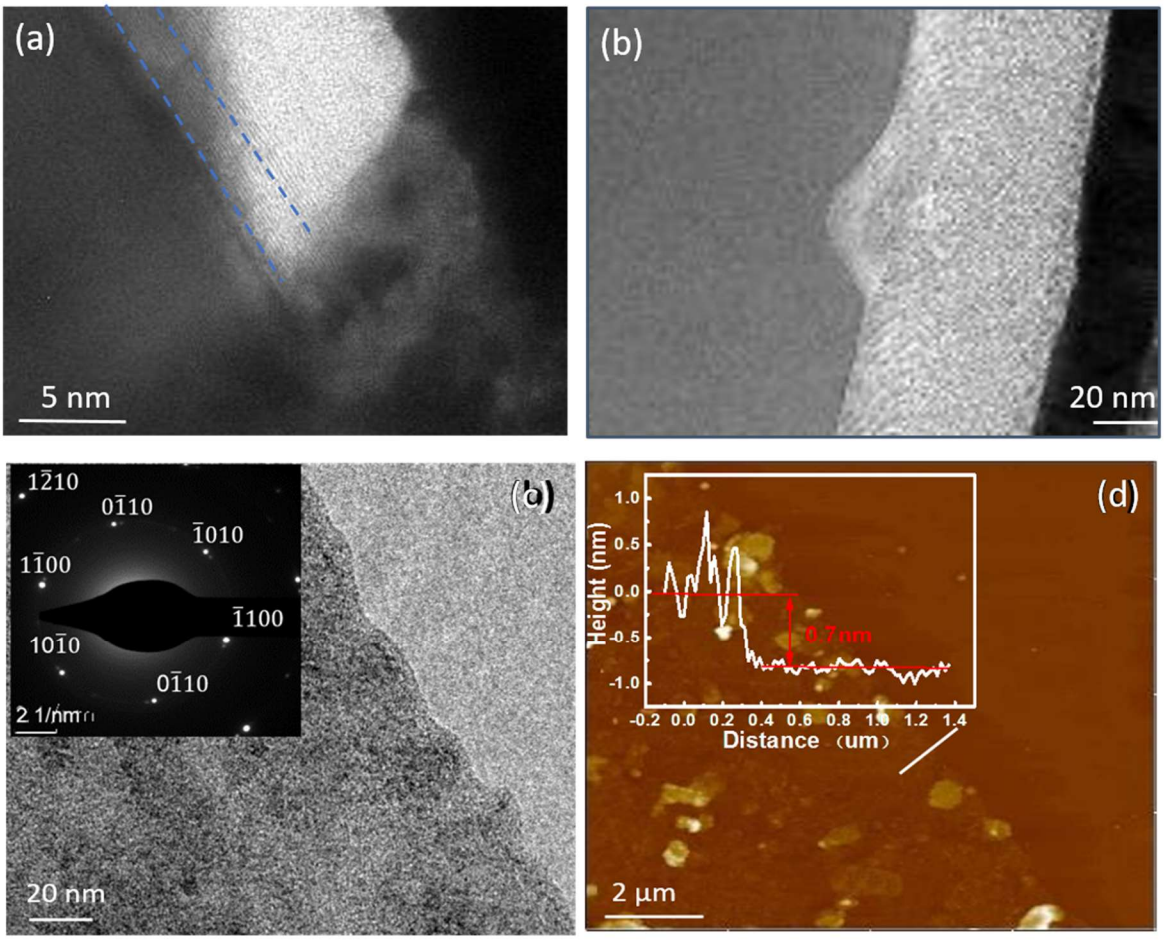

Fig. 4.12 (a) Cross-sectional TEM image of graphene sample grown on Fe at 550 °C. Graphene is seen in between Fe substrate and Ir/Pt protection layers used during TEM

sample preparation. (b) A higher-magnification TEM image of a local thicker film region on this sample, showing graphene layered structure. (c) Plan-view TEM image of a transferred graphene film from the sample grown at 550 °C. The inset is its SAED pattern. (d) AFM image of a transferred graphene film on SiO_2. The inset shows a line scan profile, indicating a graphene thickness of about 0.7 nm.

AFM measurement of a transferred graphene on SiO_2 is shown in Fig. 4.12 (d). From it we can find most areas are flat and thin. A line scan profile shown in the inset of Fig. 4.12 (d) reveals a thickness of graphene film is about 0.7 nm, which indicates the existence of a bi-layer graphene. This result is in close agreement with the Raman result of this sample shown earlier. Some bright spots observed in the AFM image could be either related to the convex areas in the graphene film, which are inherited from rough Fe surface, or from thicker graphene domains.

4.4 H_2 influence on graphene on Fe growth

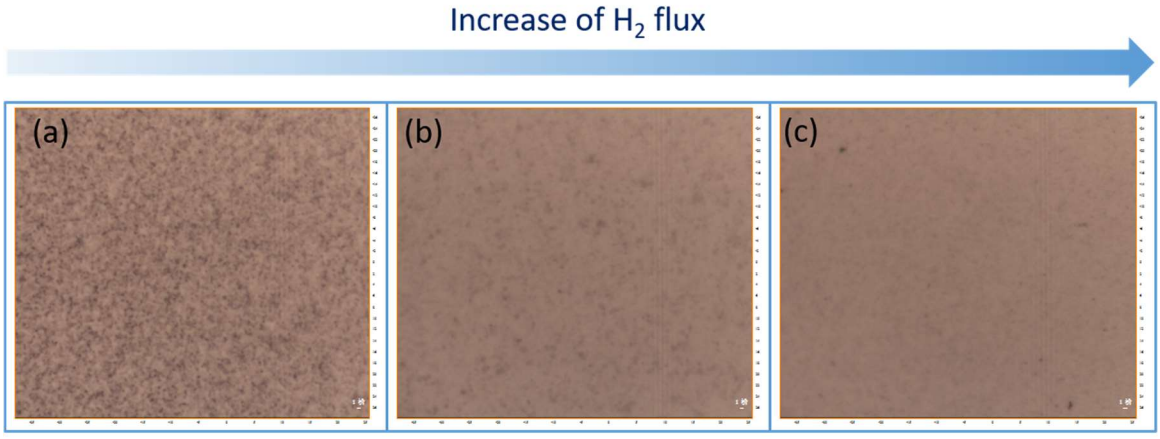

Fig. 4.13 Optical microscopy images of graphene grown on Fe at 550 ˚C with different H_2 flux: (a) 0 sccm, (b) 6sccm and (c) 15 sccm. The improvement of morphology can be easily observed with the increase of H_2 partial pressure.

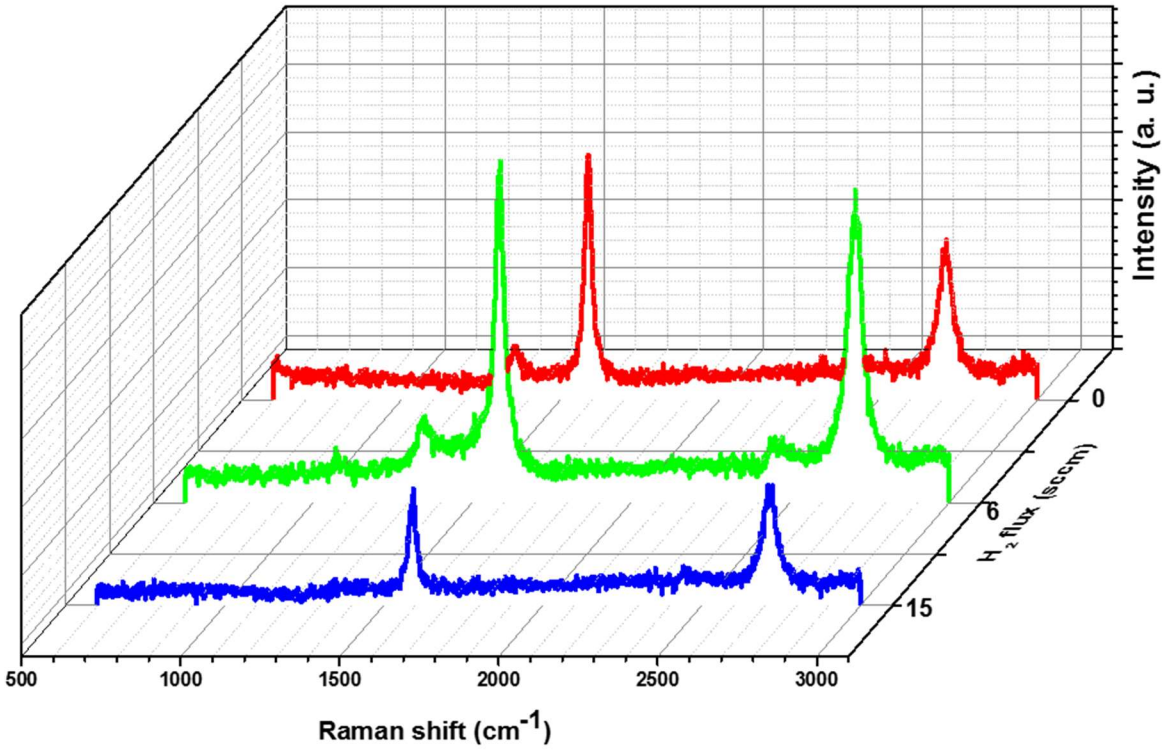

Fig. 4.14 Raman spectra of graphene grown on Fe at 550 ˚C with different H_2 flux: the red curve is 0 sccm, green curve 6 sccm and blue curve 15 sccm.

H_2 has been predicted to have significant influence on graphene growth. [117-119] To understand its effect on graphene growth on Fe with MBE, we introduce different H_2 flux during the growth. Optical microscopy images of the samples are shown in Fig. 4.13. With the increase of H_2 flux, the surface of graphene is thinner and more uniform, which indicates possible advantage of using H_2 for the growth. Raman analysis was done on the same series of samples and the result is shown as red, green blue curves in Fig. 4.14, respectively. It is observed that with the increase of H_2, the intensity of D peak gradually decreases and finally disappears. At the same time, graphene characteristic peaks G/2D ratio decreases, which means graphene is becoming thinner. From that, we conclude that

the presence of H_2 benefits graphene growth in such ways : 1. H_2 will dilute carbon partial pressure in the chamber, which slows down the growth rate; 2. With reactive H_2, the unorganized or defective graphene edges can be etched that improves the crystallinity of graphene. It provides a possible direction to improved graphene quality, which will be needed to be studied further in the future. However, the ability of MBE chamber should also be taken into consideration, which are kept in UHV condition with the help of various pumps (turbo, mechanical, ion pumps). Too much H_2 will increase work load to the pumps and decrease the lifetime of pumps. And H_2 itself is very difficult to be pumped away due to very small atomic number.

4.5 Growth mechanism of graphene on Fe growth

Finally, we briefly discuss the graphene growth mechanism. As the temperature is lower than 350 °C, the solubility of C in Fe is low, therefore, reaction between C and Fe is negligible, leading to no graphene growth. As the temperature is higher than 350 °C, enough C atoms are dissolved into Fe substrate and react with Fe to form iron carbide: $Fe + C \rightarrow Fe_xC_y$, which transform into graphene at the same time: $Fe_xC_y \rightarrow Fe + C$. The sequential reaction and decomposition mechanism leads to the growth of graphene in the intermediate temperatures (400~650 °C). As the temperature is higher than 650 °C, the formation and decomposition speed of Fe_xC_y increases drastically, which leads to the quick formation of discrete thick graphite domains rather than 2-D uniform graphene films. Thus, the formation and decomposition of Fe_xC_y plays an indispensable role in the growth of graphene on Fe, which is different with graphene growth on other metals.

4.6 Conclusion

In this chapter, we have carried out temperature-dependent growth of graphene thin films on Fe by MBE. Graphene begins to grow at a very low temperature of 400 °C and covers entire Fe surface at a relatively low temperature of 500~550 °C. Graphitic islands dominate the growth at a temperature higher than 600 °C. It is found that the formation/decomposition of Fe_xC_y is responsible for the growth of graphene on Fe, which differs with the precipitation growth of graphene on some other metals. Graphene samples were characterized by Raman, X-ray photoelectron spectroscopy, X-ray diffraction, optical microscopy, transmission electron microscopy and atomic force microscopy, which gives information of graphene quality. Additionally, introducing H_2 helps to grow thinner and higher quality graphene.

Chapter 5 Precipitation growth of graphene under exfoliated hexagonal boron nitride to form heterostructures on cobalt substrate by molecular beam epitaxy

5.1 Overview

Research on graphene and hexagonal boron nitride (h-BN) heterostructure has attracted intense attentions for band engineering and device performance optimization of graphene. The advantages of the system have attracted widespread interest of the growth and properties study of the heterostructures containing graphene and h-BN. Much work has been reported about the preparation of the heterostructures by employing various growth methods and using on different substrates. However, the growth of graphene and h-BN heterostructure is still challenging. Because of the stability of boron and nitrogen molecules under inert conditions, the reaction to form h-BN usually requires high growth temperature (>900 ˚C) and long growth duration (several hours). Additionally, due to the weak vdW interaction, it is difficult for boron and nitrogen atoms to stick to the top of the deposited film and, therefore, hinders the thick h-BN growth, which is the basic requirement for dielectric substrates and barriers.

In this chapter, we use exfoliated h-BN on Co thin film as the substrate to easily achieve thick h-BN and grow graphene '*on*' the substrate by molecular beam epitaxy (MBE). The heterostructure samples were characterized by Raman, optical microscopy, atomic force microscopy, microwave impedance microscopy and scanning tunneling microscopy. It is found that graphene can be grown at relatively low growth temperature

(~740 °C) and '*underneath*' h-BN flake. In this way, we demonstrate a new pathway to produce graphene/h-BN heterostructure on Cobalt (Co) by MBE. Growth mechanism involving the dissolution/precipitation of carbon atoms in Co is used to explain the unconventional growth behavior. The results in Chapter 5 have been submitted to Applied Physics Letter.

5.2 Substrate preparation and equipment information

The substrate is prepared with the conventional mechanical exfoliated method to produce h-BN flakes on the tape and then put on various wafers ((i)A 300 nm Co substrate was grown on SiO_2/Si wafer by e-beam evaporator mainly discussed in this study and (ii) SiO_2/Si wafer for reference) as shown in Fig. 5.1. After that, the substrate is cleaned with acetone, IPA and water to remove tape residue.After that, h-BN flakes were transferred on Co by typical tape-exfoliation method to finish substrate preparation. The substrate was afterwards transferred into a Perkin-Elmer MBE chamber for graphene growth. Acetylene gas (C_2H_2, Airgas, 99.9999%) was connected to the MBE chamber as C source, while H_2 gas (Airgas, 99.9999%) was also introduced to the chamber by a needle valve to suppress Co evaporation. The substrate temperature was ramped to a target growth temperature between 720 °C and 800 °C with a ramping rate 10 °C/min. Before growth, substrate was annealed in 10 sccm H_2 for 10 minutes to remove possible contamination. Then H_2 flow rate was decreased to 6 sccm, and graphene growth started by the introduction of 3 sccm acetylene. The growth duration lasted from 60 to 1200 s. After the growth, the sample was cooled to room temperature with a cooling rate of 10 °C/min.

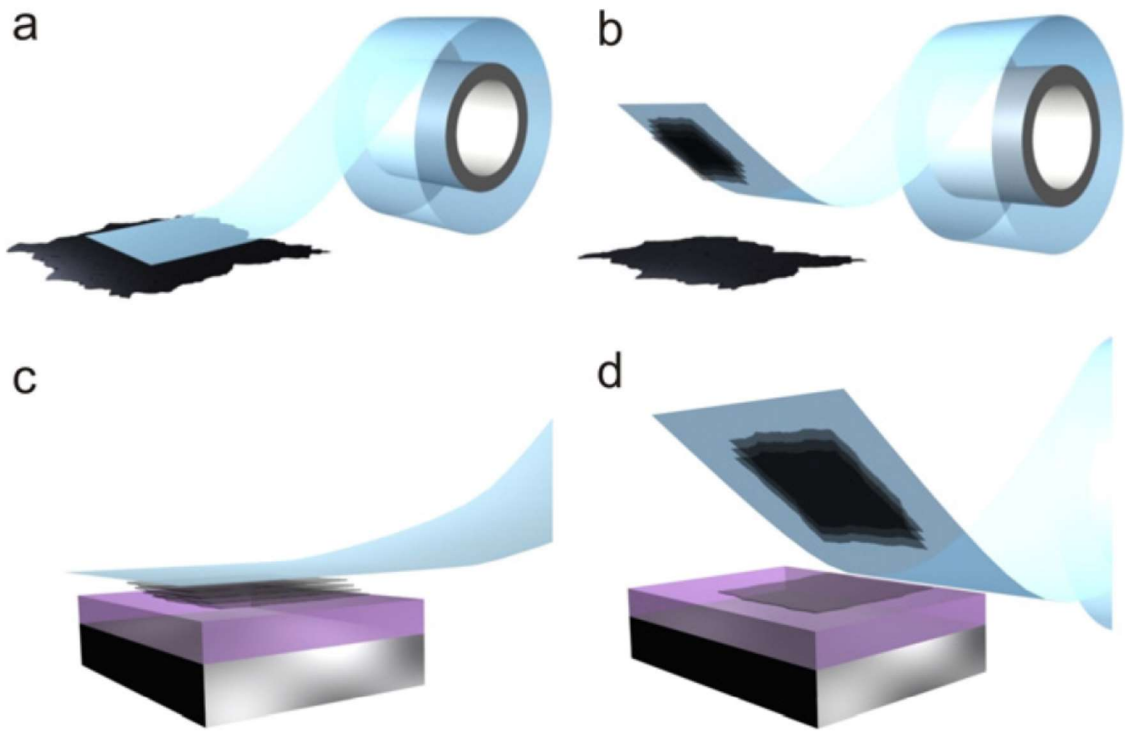

Fig. 5.1 Micromechanical exfoliation of h-BN. (a) Adhesive tape is pressed against a 2D crystal so that the top few layers are attached to the tape (b). (c) The tape with crystals of layered material is pressed against a surface of choice. (d) Upon peeling off, the bottom layer is left on the substrate. (Adapted from [101], with copyright permission)

Before the growth, AFM was done on prepared exfoliated h-BN flakes on Co substrate (Fig. 5.2). H-BN flakes sit on the Co substrate with much lower density compared to that of SiO_2/Si substrate using the same procedure, which is due to the rougher Co surface (RMS roughness ~ 1.5 nm at 4 μm^2 area) compared with pristine SiO_2/Si. Raman spectrum (Fig. 5.2) shows a sharp h-BN E_{2g} peak located at 1367 cm^{-1} for a flake size ~ 100 μm^2. The inset images of Fig. 5.2 are measured by tapping mode AFM and show the h-BN flake thickness is of ~65 nm, which is desirable thickness compared with the thin grown h-BN

film. The RMS roughness of h-BN at the center area is 0.85 nm (4 μm^2 area), and some 'wrinkles' from h-BN are also observable from AFM image which is from exfoliation process.

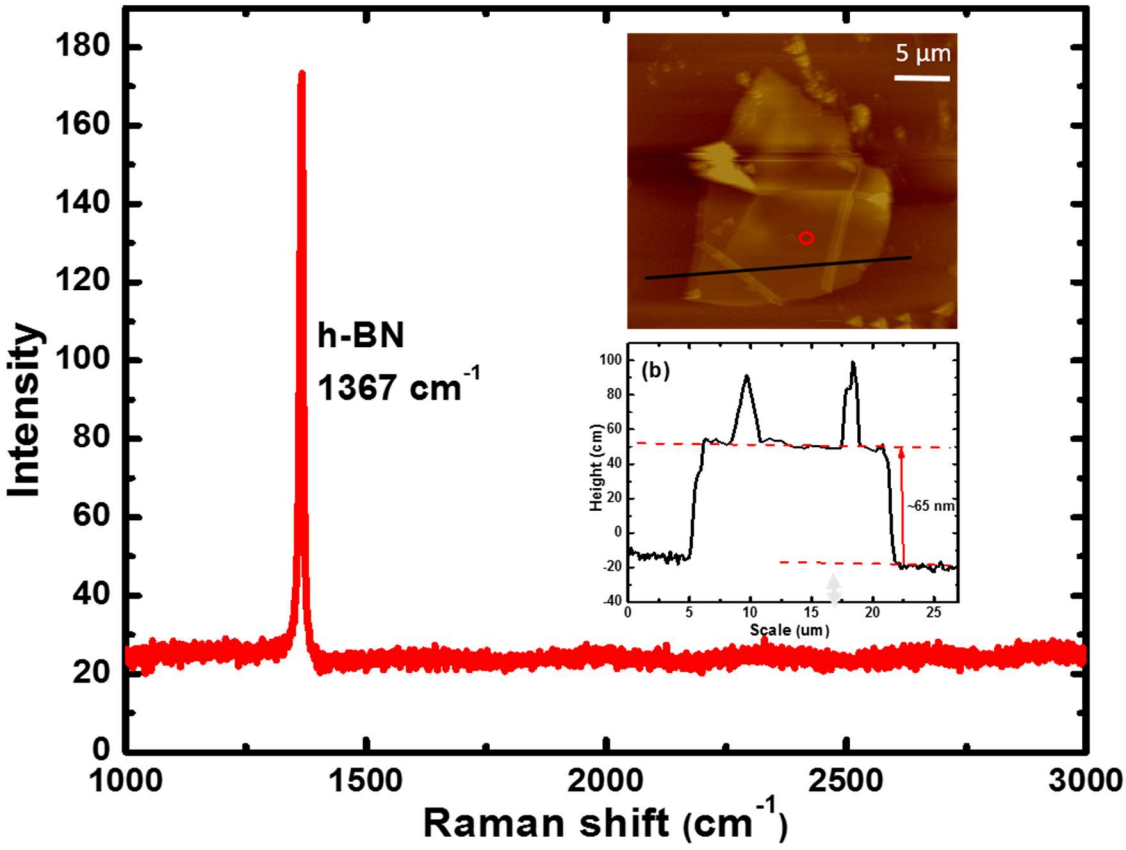

Fig. 5.2 Raman and AFM analysis of exfoliated h-BN on Co substrate before growth. The main image is Raman spectra measured on exfoliated h-BN area, shown as the red spot of the inset. The inset images are tapping mode AFM images, with top one showing topological information and bottom one showing thickness profile along the black line of top inset image.

The characterization equipment information is listed. The surface roughness of the substrate was measured by a tapping mode Veeco D5000 atomic force microscopy (AFM)

system. Optical microscopy and Raman characterizations were performed using a HORIBA LabRam system equipped with a 60-mW 532-nm green laser. A lab-built Microwave Impedance Microscope (MIM) based on a contact-mode Bruker Dimension Icon AFM platform was used for surface morphology analysis and conductance of samples after growth. The samples were also studied using a Nanosurf Naio Scanning Tunneling Microscope (STM).

5.3 Growth procedures and characterization of grown films

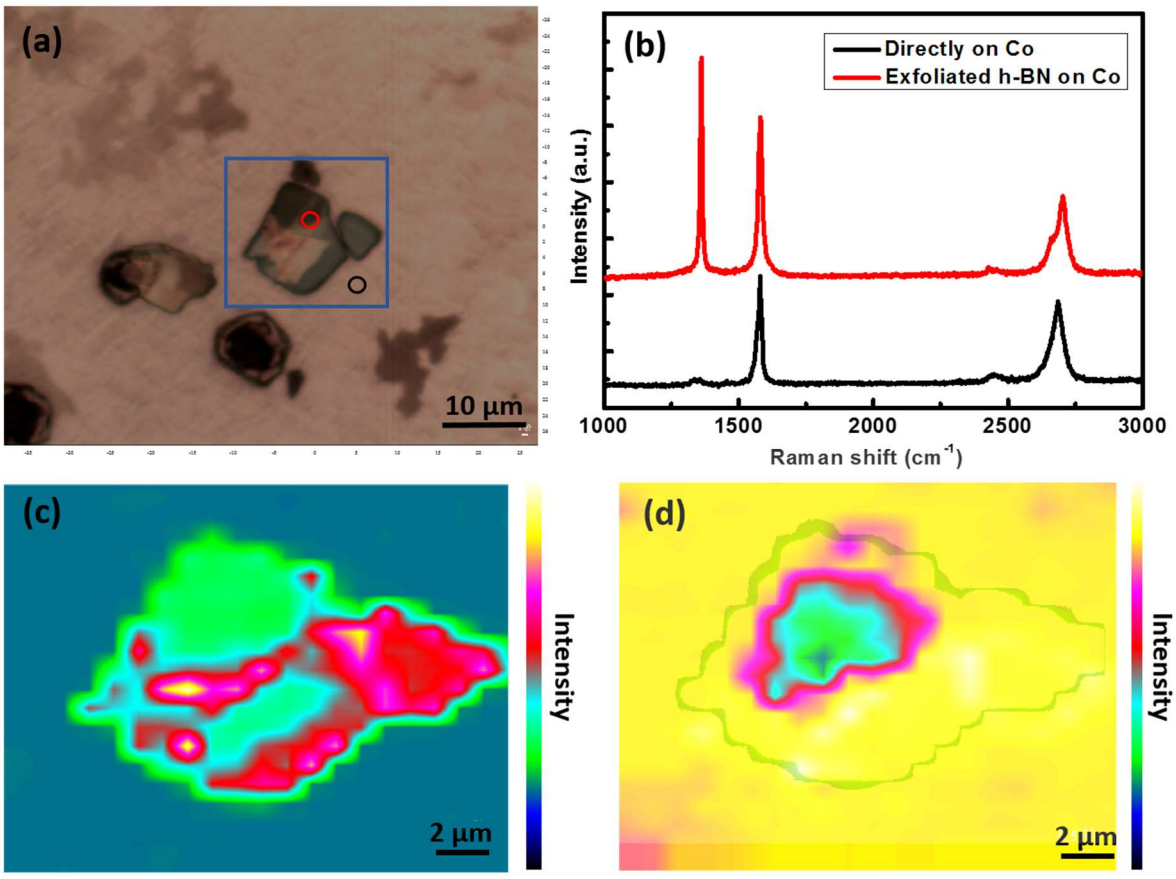

Fig. 5.3 Characterizations of graphene on exfoliated h-BN growth. (a) Optical microscopy image of graphene on exfoliated h-BN on Co. Blue square is h-BN flake. There is a black

hole at left corner of blue square, which is due to Co loss. (b) Raman spectra of as-grown sample, which are measured on the part shown in the red and black circles in (b). (c, d) Raman mapping of h-BN E_{2g} and graphene G peaks. The mapping area is indicated in (b) blue square.

A typical graphene growth was done at 770 ˚C for 100 s. In the optical microscope image (Fig. 5.3(a)), two h-BN flakes can be found and a hole is shown (blue square) which is resulted from the tape peeling off process and Co evaporation at high-temperature. Most area of Co surface shows uniform color contrast but still some contrast is observed (especially on the top left part), which means graphene growth is locally. Raman spectra were measured at various locations. The red spectrum is measured on h-BN flake and black one is away from h-BN flake, as shown in the red and black circles in Fig. 5.3 (a). Clear graphene Raman peaks at 1572 and 2685 cm^{-1} are observed with G/2D ratio of ~1 when measured on Co film, indicating existence of bi- or tri-layer graphene. A 20 cm^{-1} blue shift of 2D peak is found when measurement was done on h-BN flake, which will be discussed later.

Detailed Raman mappings of h-BN E_{2g} and graphene G peaks were done to achieve a better distribution information, shown in Fig. 5.3 (c) and (d). The mapping area is shown by the blue square of Fig. 5.3 (a). When mapping over h-BN peak intensity, a h-BN flake shape is identified in Fig. 5.3 (c), which agrees with the optical microscopy observations. Different colors are observed, which is from different intensity/thickness of h-BN layers from the exfoliation process: the red area is thicker compared with green area, and blue area is measured on SiO_2. A more uniform color distribution in Fig.5.3 (d), which is

mapping of graphene G peak intensity, shows the graphene film coverage. Most of the area is covered by yellow color, indicating graphene's good uniformity over 20 um *20 um area. However, weaker or even no graphene signal (red and green color) can be observed in the center part of h-BN flake (light blue shape indicated). An interesting phenomenon was discovered here: the distribution of graphene is not correlated with the thickness or roughness of h-BN flake, but relies on the off-edge distance or h-BN flake size, which helps clarify growth mechanism.

5.4 Temperature and time dependence of the growth analysis

5.4.1 Growth temperature dependence

In chapter 4, we discussed and revealed that the growth temperature has very large influence on the characteristics of graphene film grown on Fe. And it has revealed carbon solubility and reaction with metal substrate plays a key role on the growth result. For better understanding of graphene growth on exfoliated h-BN on Co, besides the sample grown at 770 ˚C, we tried another three more samples with the same growth conditions but different growth temperatures: 800 ˚C, 740 ˚C and 720 ˚C.

Once the samples were grown, a direct Raman measurement with optical microscope was performed shown in Fig. 5.4. Optical microscopy images show different graphene contrast in Fig. 5.4 (a-c). Thicker graphene regions (darker spots) with higher density are observed at higher growth temperature samples, shown in Fig. 5.4 (a) 800 ˚C. The thicker graphene islands become less and disappeared when growth temperature decreases, shown in Fig. 5.4 (a) 720 ˚C.

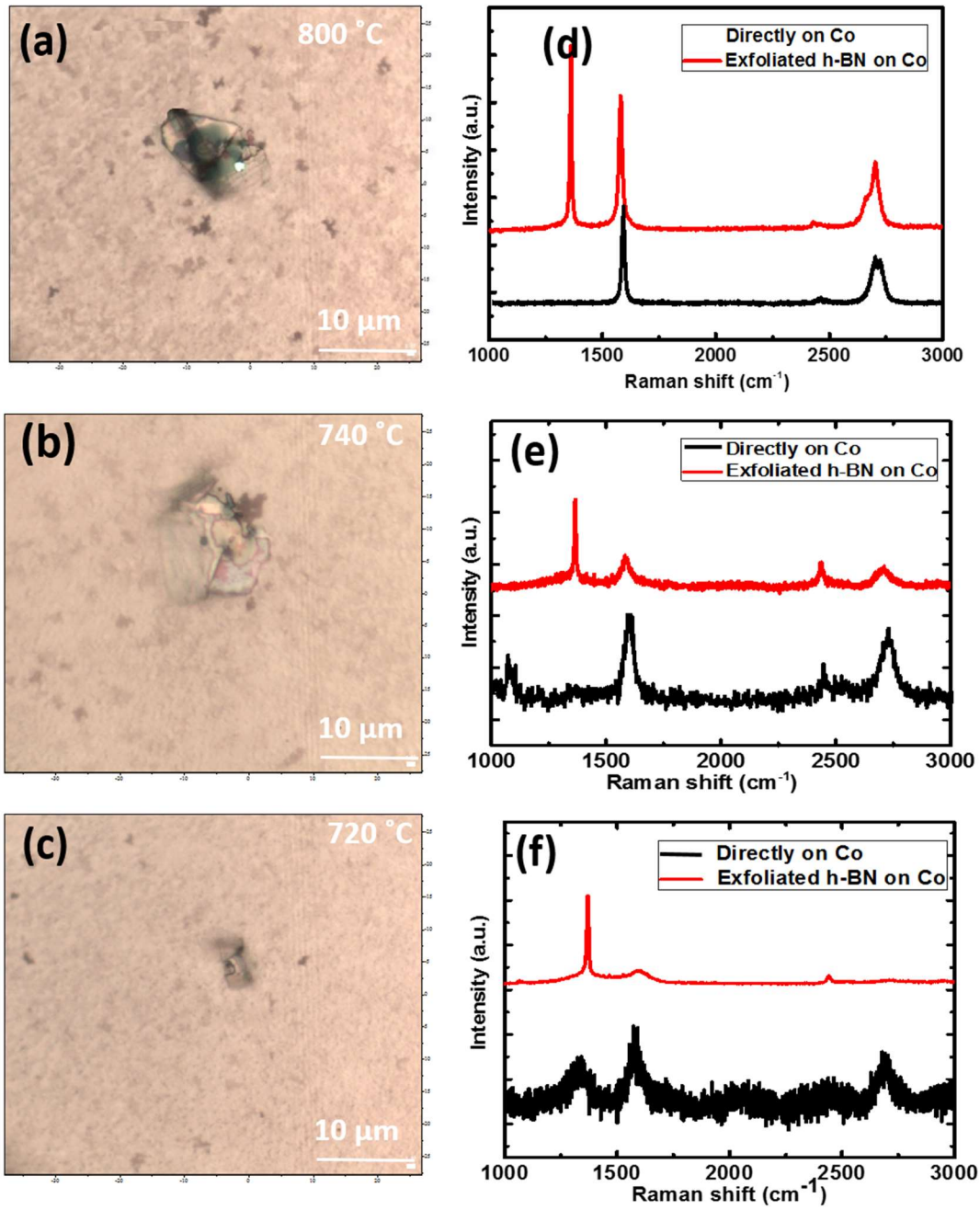

Fig. 5.4 Temperature-dependent graphene growth on exfoliated h-BN on Co. (a-c) Optical microscopy images of graphene on exfoliated h-BN on Co, with growth temperature changes from 800 ˚C to 720 ˚C. (d-f) Raman spectra measured at locations indicated as red and black circles shown in (a-c).

A series of Raman spectra were measured at the locations shown in the optical images with red and black circles (on h-BN and away from h-BN respectively) of samples grown at different temperature. Sharp h-BN peak is observed from all three samples. However, graphene signal (G/2D ratio) becomes weaker with the decrease of growth temperature, and when the growth is at 720 ˚C, visible D peak is shown on Raman spectrum and graphene signal is ignorable. The fact that '*the lower growth temperature, the weaker graphene signal is*' happens not only in the bare Co but also h-BN regions, as shown in red and black curves of each individual Raman spectra. The result agrees with the optical microscopy observations, and shares similar trend as graphene growth on other metals. It stimulates our interest in more analysis to find graphene growth similarity and difference on insulating h-BN and conductive Co substrates.

5.4.2 Growth time dependence

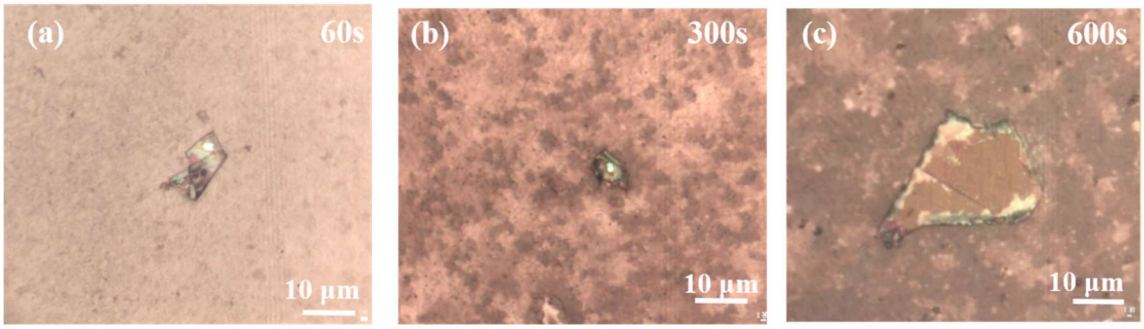

Fig. 5.5 Optical microscopy images of graphene on exfoliated h-BN on Co, with growth duration varies from (a) 60 s, (b) 300 s and (c) 600 s.

Different samples were grown on exfoliated h-BN on Co at 770 ˚C for 60 s, 300 s, and 600 s to find graphene dependence of growth time. As shown in the optical microscopy images of Fig. 5.5, with longer growth time, blacker domains with higher density and larger

area are observed, which is direct proof of thicker graphene flakes. The phenomenon is similar to the graphene growth on Fe that we observed in Chapter 4.

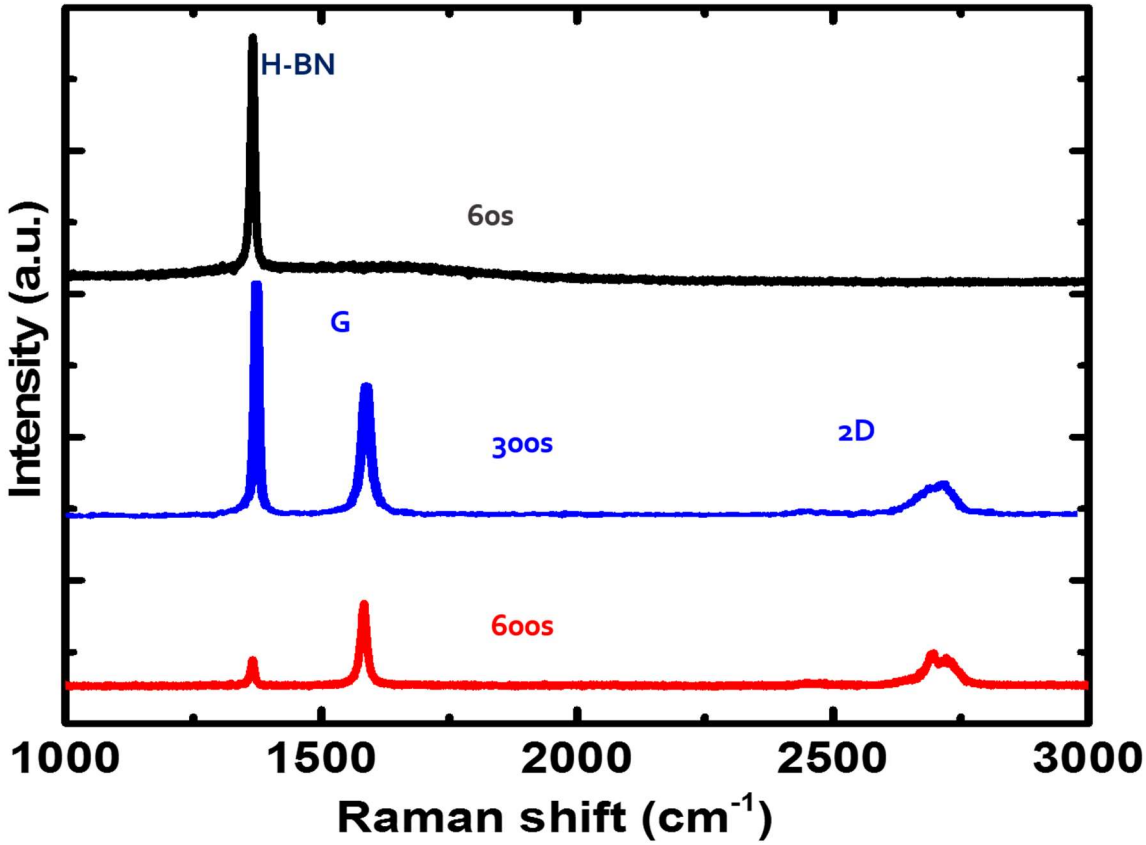

Fig. 5.6 Time-dependent graphene growth on exfoliated h-BN on Co. Raman spectra of graphene grown with different duration, discussed in Fig. 5.5. The measurement was done on exfoliated h-BN region.

Here we also present Raman characterization (as shown in Fig. 5.6) for samples shown in Fig. 5.5. Three main peaks are observed, which is h-BN located at ~1365 cm^{-1}, graphene G located at 1570 cm^{-1} and 2D at 2700 cm^{-1}. When the growth time is short (≤ 60 s), only h-BN peak is detected with no graphene signal, as shown in the black curve, which means graphene cannot grow within this growth duration; and as growth time

increases, G peak appears and becomes larger which means graphene starts to grow and thickness is increasing (shown in the blue curve). When the growth time reaches 600 s, G/2D ratio (representing graphene thickness) reaches largest among three Raman spectra, and G peak is higher compared with h-BN ratio, which gives a relative thickness information of graphene normalized with h-BN thickness. It agrees with result from optical microscopy images. Graphene is growing thicker with the increase of growth of time. With this guidance, we then try to grow even longer time, up to 1200 s.

A detailed analysis of Raman spectra was done based on 2D peak information collected from Raman spectrum with wider growth temperatures changing from 60s, 100s, 200s, 300s, 600s, 900s and 1200s. As observed in Fig. 5.6, double-peak phenomenon was observed on graphene 2D peak. A zoomed-in Raman spectrum of 2D peak at 2700 cm^{-1} is shown in Fig. 5.7 (a). After fitting, two peaks are found to exist at 2693 and 2736 cm^{-1} which are the two components of graphene 2D peak [120]. Similar broaden 2D peaks have been observed for all heterostructured samples, which is due to the orientation and stacking of multilayer graphene.

The graphene thickness dependence on growth time is studied in Fig. 5.7 (b). Assuming thickness of h-BN flakes is roughly the same, we use G/h-BN ratio to identify the graphene thickness. With the increase of growth time, graphene thickness increases, which agrees with what is observed from optical microscopy studies (Fig. 5.5); however, the increasing rate slows down and then reaches the saturation level after a long growth duration ($\geq$ 900 s in our experiment). It provides an assumption that the graphene might not be epitaxially grown 'on' h-BN, instead precipitated from Co substrate. The limitation

of the graphene thickness is from carbon solubility in Co at certain growth temperature. When growth time is short, carbon solubility hasn't reached its saturation at the growth temperature. With the increase of the growth time, more carbon atoms dissolve into Co and precipitate to form graphene during the cooling process. However, when the growth time is long enough, carbon solubility reaches its saturation in Co metal. The carbon atoms in metal have reached maxima which prevent graphene to grow thicker. Thus graphene thickness won't be influenced by growth time anymore.

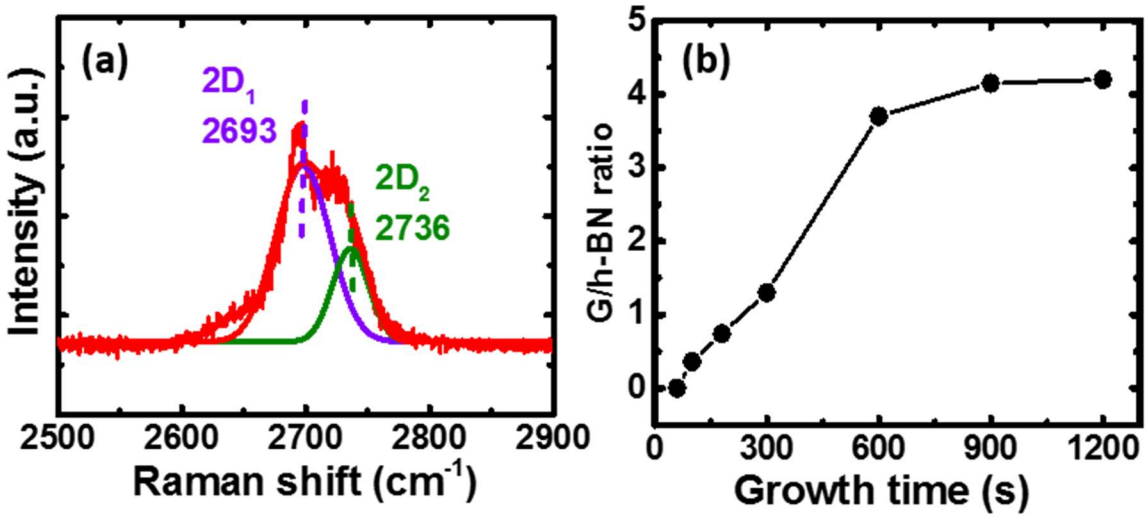

Fig. 5.7 Detailed analysis on Raman spectrum of 2D graphene peak. (a) Zoomed-in Raman spectrum showing two components of graphene 2D peak at around 2700 cm^{-1}. (b) G/ h-BN ratio dependence of graphene growth time.

For reference, a series of samples were grown at the same conditions as the sample discussed in Fig. 5.3 but the substrate is different: no Co film was deposited and exfoliated h-BN flakes were put on SiO_2 directly. The growth duration varies from 100s to 1 hour. Sample shown in Fig. 5.8 (a) (b) was grown for 100 s, same as the sample described in Fig.

5.3. Sample shown in Fig. 5.8 (c)(d) was grown for 20 min, and sample shown in Fig. 5.8 (c) (d) was grown for 1 hour. The optical images and related Raman spectra are shown in Fig. 5.8. No graphene signal can be detected at all growth durations, which means graphene cannot grow epitaxially on exfoliated h-BN without assistance of Co. This phenomenon implies the importance of Co: Co plays a key role of graphene growth on exfoliated h-BN growth. And when the growth duration is getting even longer, amorphous carbon as indicated from the Raman peak located ~1560 cm^{-1} starts to show up at the wrinkle edges of h-BN. For long growth duration, atomic carbon could deposit on the surface but prefer staying at the defects area of h-BN, but won't form graphene layer without catalyst effect of Co metal.

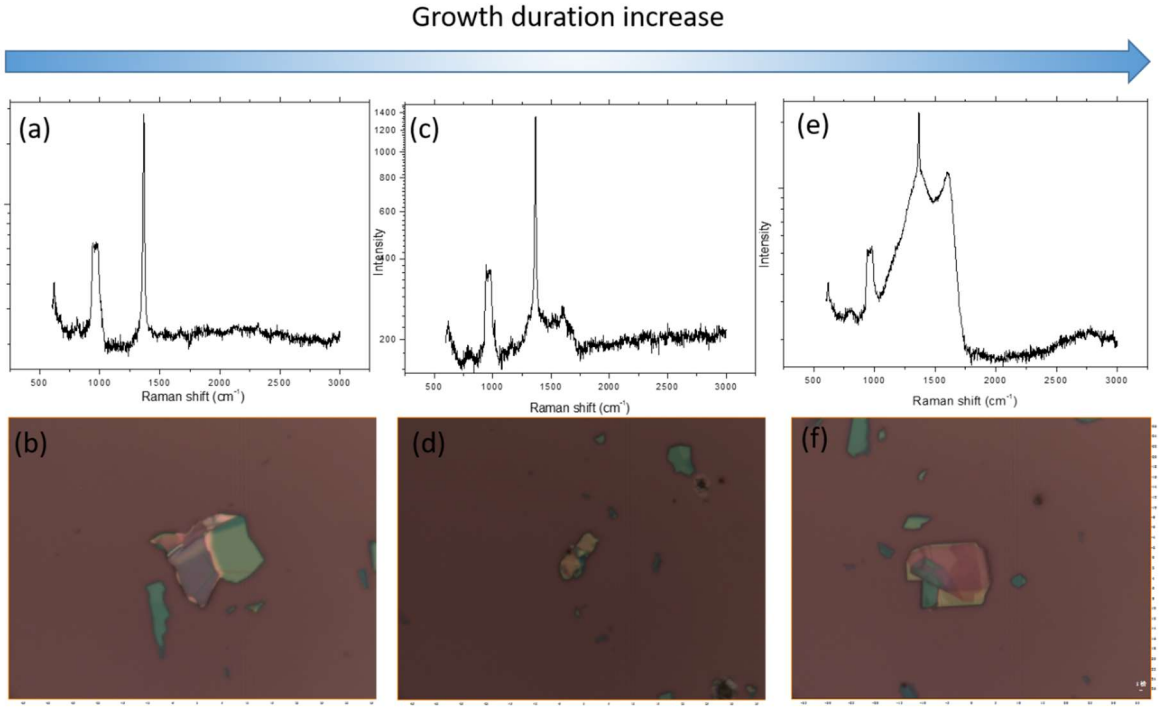

Fig. 5.8 Characterizations of graphene on exfoliated h-BN on SiO_2 growth. Different growth durations were used for three samples. (b) (d) (f) Optical microscopy image of

graphene on exfoliated h-BN on SiO_2. The middle part is h-BN flake. (a) (c) (e) Raman spectra of as-grown samples shown in (b) (d) (f), respectively. The growth time varies from 100 s to 1 hour.

5.5 Scanning probe microscopy (SPM) measurement on the grown film

A series of scanning probe microscopy measurements were performed to further reveal that graphene grows underneath rather than on top of the exfoliated h-BN flake. An h-BN flake with a thickness of ~60 nm is observed by contact mode AFM (Fig. 5.9 (a)). The roughness of the flake is around 0.90 nm for 4 μm^2 area, which is close to RMS roughness value before growth (Fig. 5.2). The deflection error image (Fig. 5.9 (b)), which gives qualitative mapping of the surface, shows some small 'wrinkles' on the h-BN flake and most of the area are locally flat.

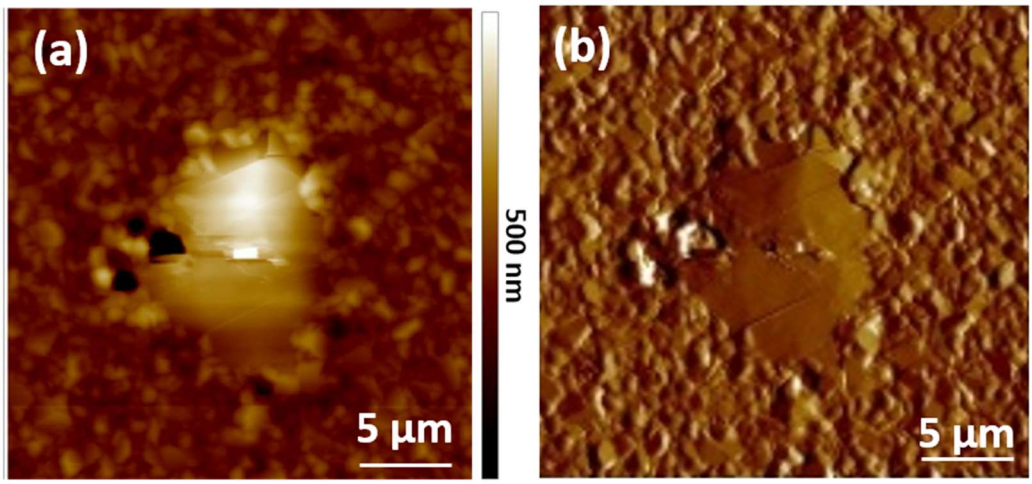

Fig. 5.9 (a) Contact AFM image of as-grown film and (b) deflection error image at same location.

Microwave impedance microscopy was carried out using a lab-built MIM [121, 122] with a solid platinum cantilever probe that has a sharp tip at the end. A microwave signal

at 1 GHz was sent to the metal probe, and the reflection signal, determined by the tip-sample admittance (inverse of impedance) was analyzed (Fig. 5.10 (a)). When the tip makes direct electrical contact with a conductive region, a large increase in the MIM signal, referenced to the case when contacting an insulating region, can be detected. It is worth noting that the MIM detection of metallic regions does not require a back-electrode on the sample because MIM senses the local screening of microwave electric field by the sample.

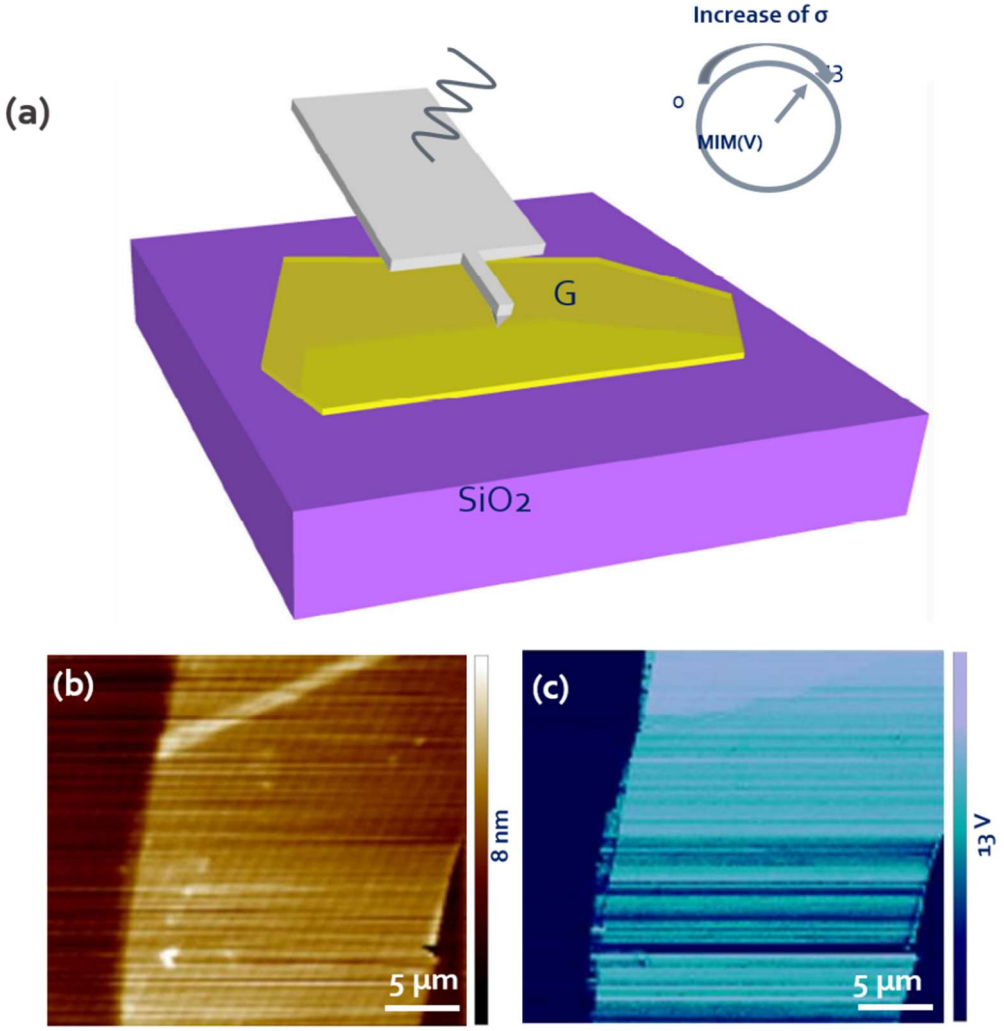

Fig. 5.10 SPM images on reference sample. (a) Illustration of lab-built AFM-based MIM setup. (b) AFM image of exfoliated graphene on SiO_2. (c) MIM of sample shown in (b).

A reference sample was first measured to guarantee proper function of MIM, as shown in Fig. 5.10 (b) and (c). An exfoliated graphene was transferred on SiO_2/Si and then measured under contact AFM and MIM. The graphene thickness is ~1 nm from AFM measurement with pristine surface (Fig. 5.10 (b)), a folded-layer feature was observed at the edge of AFM image. Fig. 5.10(c) shows MIM image of the sample. When the tip is on graphene area, brighter color is observed compared with SiO_2 area, which means larger conductance leads to larger signal in MIM measurement.

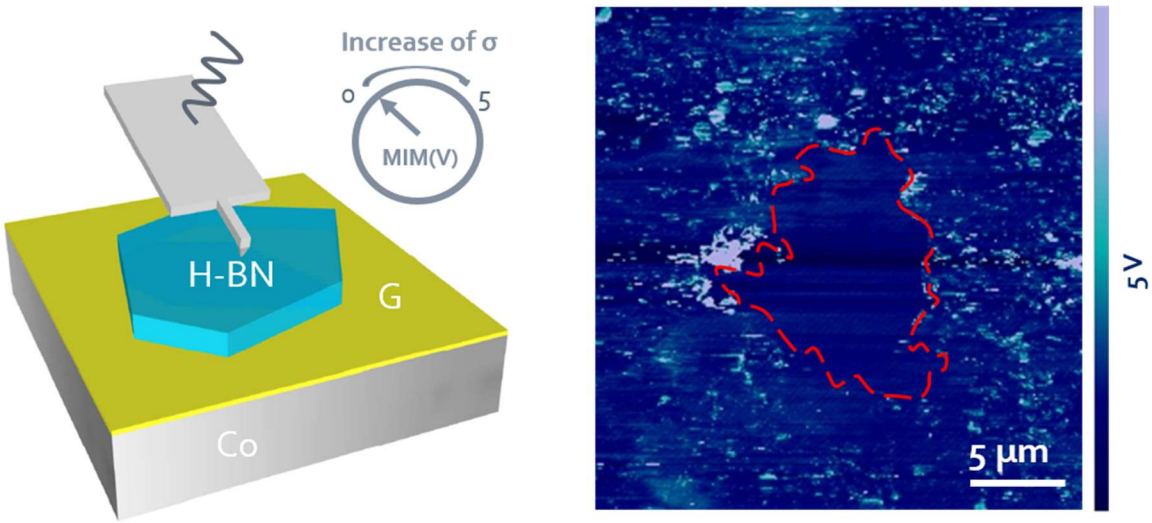

Fig. 5.11 MIM image on grown sample. (a) Illustration of lab-built AFM-based MIM setup measured on as-grown sample. (b) MIM of sample shown in Fig 5.9.

In the simultaneously obtained MIM image for as-grown sample in Fig. 5.9, qualitatively different features are observed in the h-BN region and its surrounding Co area (shown in Fig. 5.11): random spark signals (bright spots) are observed in the Co area whereas the h-BN area has a consistently low MIM signal. The inhomogeneous MIM spark signals over the Co area is due to imperfection of graphene quality and substrate flatness,

different with the MIM image of pristine exfoliated graphene on SiO_2 in Fig. 5.10 (c). In contrast, no sparks being detected in the h-BN area indicate that there is no graphene on top of h-BN. Since Raman spectra indicate the existence of graphene from h-BN area, it can be concluded that graphene has not been grown on top of the exfoliated h-BN, but underneath the flake.

When plotting MIM intensity vs. materials (Fig. 5.12), we can find that the MIM signal intensity increases with the increase of conductivity of materials, which agrees with the theoretical prediction. [122]

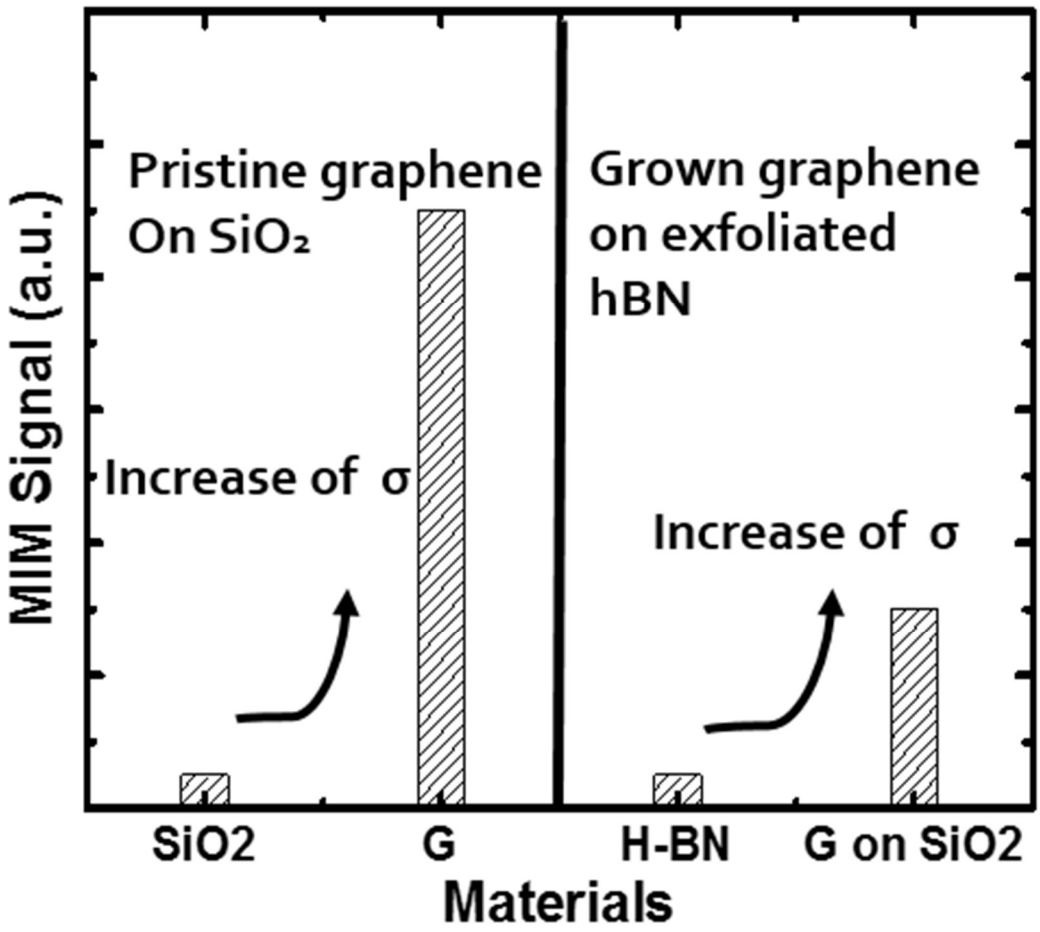

Fig. 5.12 Comparison of MIM signal measured on different surfaces

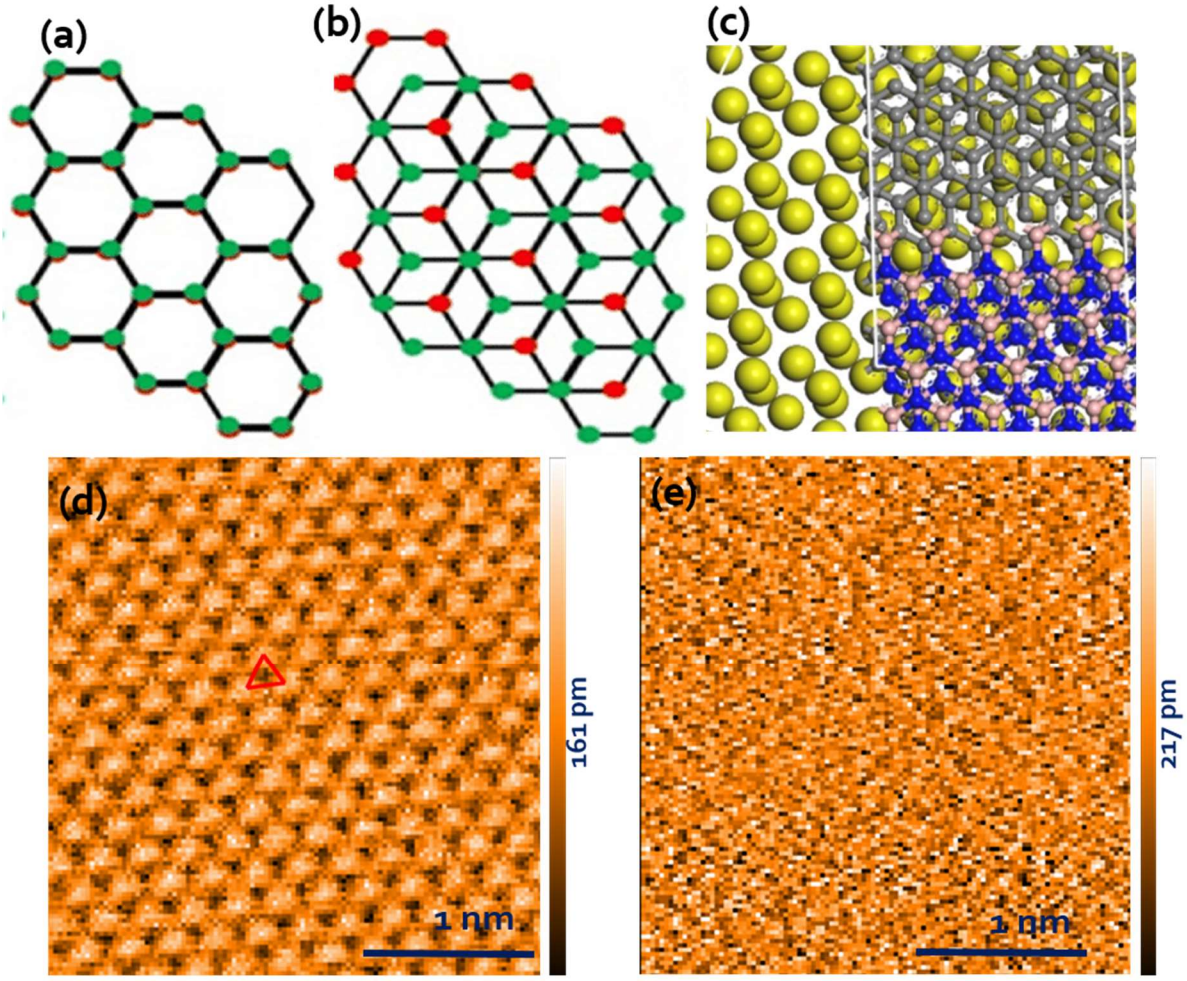

Fig. 5.13 STM on as-grown sample. (a) Monolayer graphene, (b) ABA stacking of graphene to form triangular pattern of STM. (c) schematic of graphene on exfoliated h-BN sample. (d) STM measured directly on graphene. (e) STM measured on h-BN area.

STM was performed to check the atomic information of the as grown sample: typical graphene STM pattern with a lattice constant of 2.40 Å is observed on Co (Fig. 5.13(d)), but no pattern can be detected when measured on exfoliated h-BN (Fig. 5.13(e)). This result implies the reason that (i) either there is completely no graphene (ii) or graphene is not continuous on top of insulating h-BN, leading to the difficulty to be detected. From

the graphene pattern and compared with Fig. 5.13(a)-(c), we can conclude graphene is ABA stacking mode.

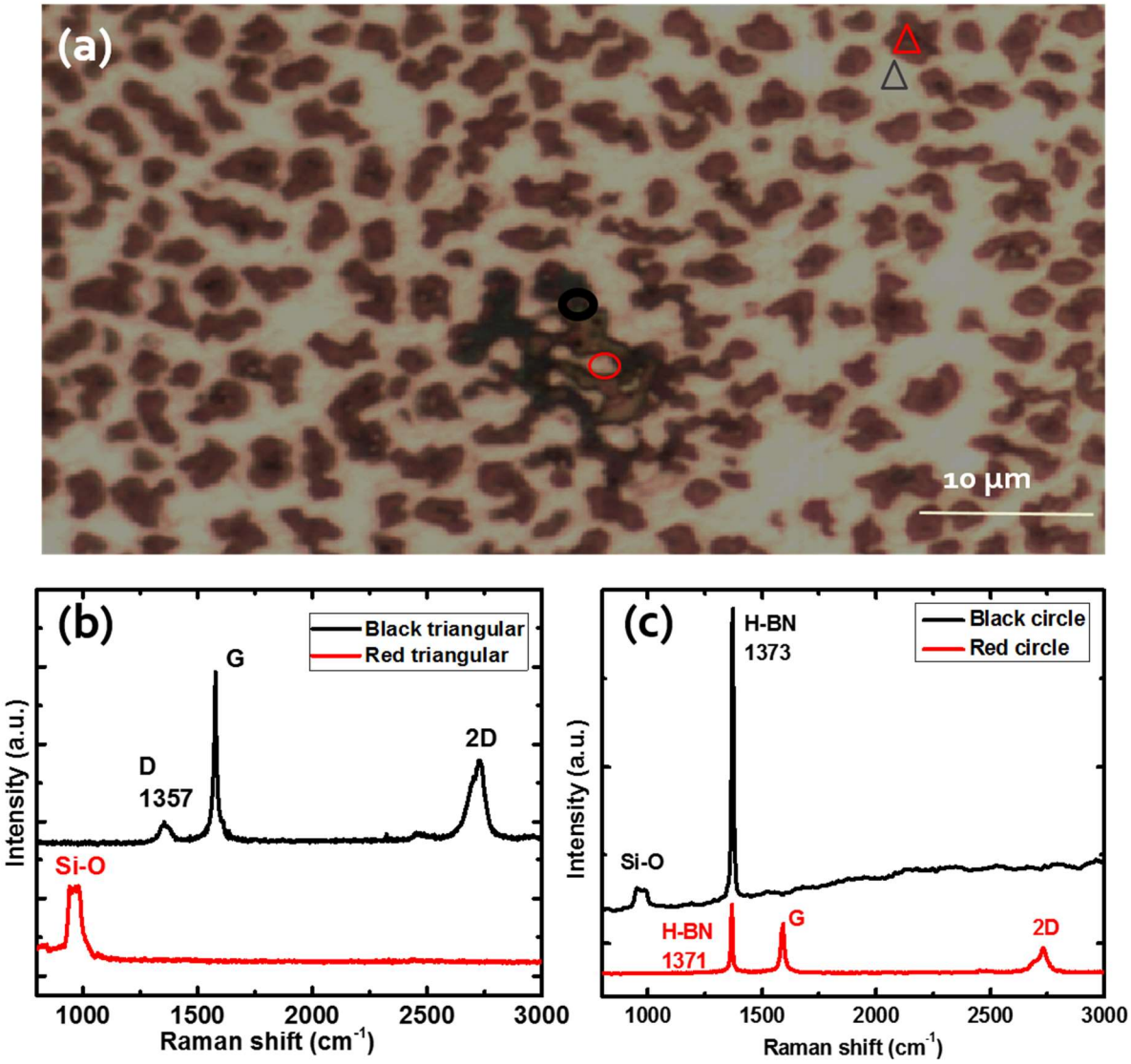

Fig. 5.14 (a) Optical microscopy image and (b-c) Raman spectra of graphene on exfoliated h-BN on Co film substrate. (b) are Raman spectra measured on h-BN flake, with red curve on the hole and black curve off the hole. (c) are Raman spectra measured on h-BN flake, with red curve off the hole and black curve on the hole.

A sample was grown at the same growth conditions mentioned previously (Fig. 5.9), except that no H_2 gas was used. After growth, some Co was evaporated and left holes, as shown in Fig. 5.14 (a). Raman analysis was done directly on the Co and h-BN area. When measured on Co, Raman shows graphene signal (Fig. 15 (b) black curve), but no graphene signal can be detected when measured on the holes (Fig. 15 (b) red curve). Similar result is found when measured on the exfoliated h-BN area. If the h-BN flakes cover holes (no Co underneath), no graphene signal can be observed (Fig. 5.14 (b) black curve). If there is Co underneath h-BN, it shows graphene signal as discussed before (Fig. 5.14 (b) red curve). It provides another evidence of the necessity of Co for the graphene/h-BN heterostructure growth.

5.6 Transferred as-grown film and growth mechanism

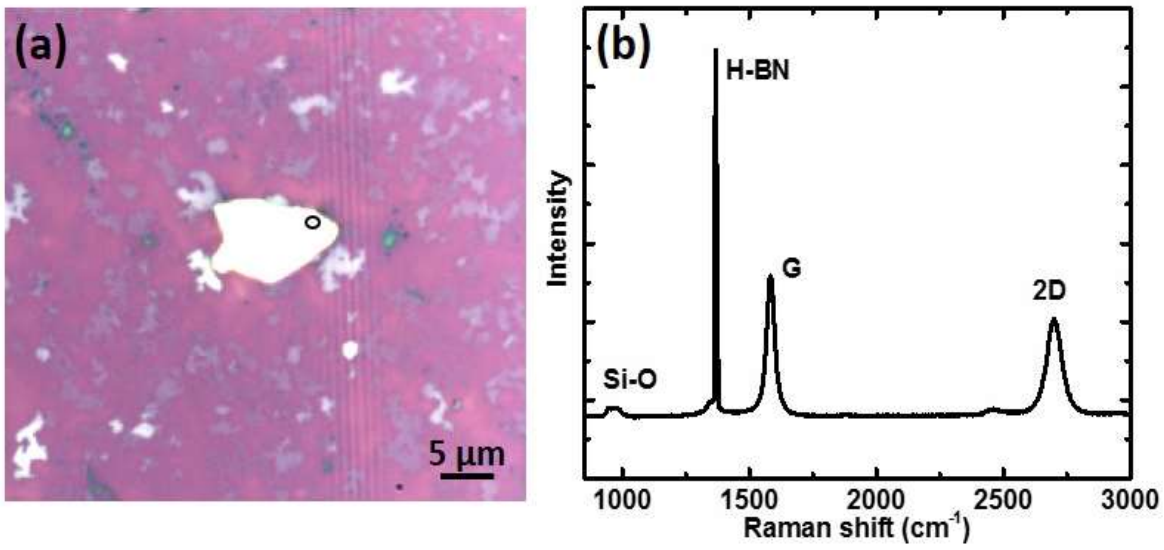

Fig.5.15 Optical and Raman images of transferred heterostructure on SiO_2. (a) Optical image of graphene/exfoliated h-BN on SiO_2. (b) Raman spectrum of black circle area indicated in (a).

Further film transfer experiment was performed to remove the Co substrate (the etching and transferring procedure has been discussed in details in Chapter 2), and the resultant film consists of graphene/exfoliated heterostructure. After transferring, h-BN and graphene signal are both detected (shown in Fig. 5.15 (b)), meaning attractive force between as grown graphene and exfoliated h-BN can withstand transferring process, which indicates the existence of vdW forces between graphene and exfoliated h-BN layers. The transferable property of film would significantly broaden the application of exfoliation-based heterostructure.

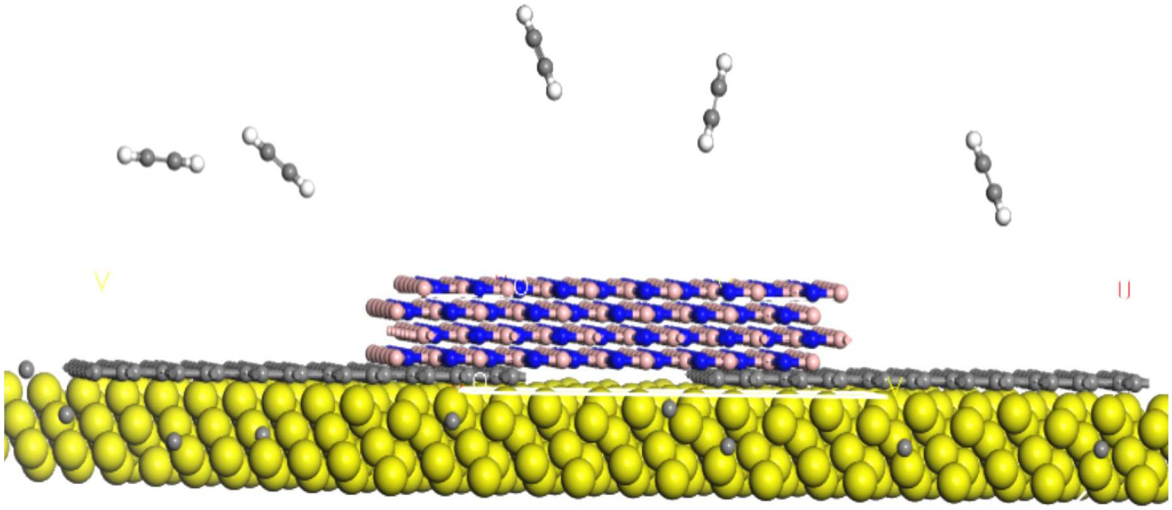

Fig.5.16 Schematic growth mode of graphene on exfoliated h-BN on Co.

Finally, we can briefly discuss the growth mechanism as illustrated in Fig. 5.16. C_2H_2 molecule decomposes into carbon and hydrocarbon atoms at the Co surface, and the dissolved carbon atoms diffuse into the area under the exfoliated h-BN flake and precipitate later in the same area to form graphene during the substrate cooling period. The graphene coverage underneath h-BN is determined by carbon solubility in Co, diffusion length (how far carbon atoms can reach the center area of h-BN from its edge), and substrate

temperature cooling rate. For example, we can transfer exfoliated h-BN onto Cu-Ni alloy and achieve h-BN on single- or bi- layer graphene with controlling the fraction of Ni. [123-125] It would significantly broaden the application of exfoliation-based heterostructure.

5.7 Conclusion and future working direction

In summary, we demonstrated h-BN/graphene heterostructure by precipitation growth of graphene under exfoliated h-BN flakes on Co film substrates. The growth was done by introducing C_2H_2 gas onto heated substrate in an MBE chamber. No graphene was grown on top of the h-BN flakes under the investigated growth conditions. The graphene coverage and thickness are dependent on the size of h-BN flakes and the growth temperature and duration, which is related to the carbon's diffusion length and solubility in Co. This growth method provides a convenient path to produce graphene/h-BN heterostructures, which avoids high temperature and long duration needed for BN growth.

Chapter 6 Summary

2D van der Waals (vdW) material systems have received extensive attention recently due to their potential wide variety of applications. To stride over the limitation of silicon platform electronics and explore new paradigm in 2D materials and devices, scalable and wafer-scale synthesis of vdW materials and heterostructures is indispensable. Molecular beam epitaxy (MBE) provides a unique avenue to develop vdW materials and heterostructures because of its UHV condition, atomic layer deposition accuracy and in-situ characterization techniques.

This dissertation summarizes my work in the past four years on the study of MBE growth and various characterization of vdW materials, specifically about graphene and hexagonal boron nitride (h-BN) on metal substrates. We studied the MBE growth conditions and characterizations of different vdW materials on different substrates. H-BN growth on Cu is achieved with MBE system. We developed the first h-BN/ graphene heterostructure with in-situ MBE growth on Co. We observed the layers' interaction and orientation of vdW systems comprised of multilayer graphene and h-BN. We also developed an effective method to create graphene/h-BN heterostructures by utilizing mechanical exfoliation method of h-BN. By utilizing Fe, we have in-depth studied graphene growth mechanism and achieved graphene film at relatively low growth temperature to extend graphene's usage for those devices which can only survive in moderate or low temperature. Various characterizations have been used to get better knowledge of grown film's properties in the aspects of morphology, thickness, crystallinity and so on.

Based on what we have achieved, there are several promising directions needed to be paid attention to and worked on in the future: (i) Better understanding of growth mechanism including different growth conditions' effect on growth result to achieve layer-by-layer growth controllability. (ii) Further improve as-grown vdW materials and heterostrucutres' quality and decrease difficulty of production: growth time, growth temperature and other requirements. With effort on this direction, realization of industrial application will be ramped up. (iii) Besides h-BN and graphene hybrid structures, realizing MBE growth of various 2D heterostructures comprising of alternating h-BN, BCN, graphene, topological insulators and other vdW materials. With achievement on this field, the close proximity of different layers may lead to new properties. (iv) Device applications in use of in-situ grown stacked 2D layers. For example, with graphene or other vdW materials as electrodes or active layers, h-BN as passivation and/or substrate and/or tunneling layers to discover novel properties in 2D transistors.

In conclusion, vdW materials and related heterostructures are the most promising candidate for next-generation nanotechnology innovators. The broad applications of vdW materials and heterostructures are being studied by a lot of groups in the world. And growth and characterization of vdW materials and related heterostructures is the first and key step to make the practical application possible.

Reference

1) Fiori, Gianluca, Francesco Bonaccorso, Giuseppe Iannaccone, Tomás Palacios, Daniel Neumaier, Alan Seabaugh, Sanjay K. Banerjee, and Luigi Colombo. "Electronics based on two-dimensional materials." Nature nanotechnology 9, no. 10 (2014): 768-779.

2) Xia, Fengnian, Damon B. Farmer, Yu-ming Lin, and Phaedon Avouris. "Graphene field-effect transistors with high on/off current ratio and large transport band gap at room temperature." Nano letters 10, no. 2 (2010): 715-718.

3) Bolotin, Kirill I., K. J. Sikes, Zd Jiang, M. Klima, G. Fudenberg, J. Hone, Ph Kim, and H. L. Stormer. "Ultrahigh electron mobility in suspended graphene." Solid State Communications 146, no. 9 (2008): 351-355.

4) Novoselov, K. S., D. Jiang, F. Schedin, T. J. Booth, V. V. Khotkevich, S. V. Morozov, and A. K. Geim. "Two-dimensional atomic crystals." Proceedings of the National Academy of Sciences of the United States of America 102, no. 30 (2005): 10451-10453.

5) Osada, Minoru, and Takayoshi Sasaki. "Two-Dimensional Dielectric Nanosheets: Novel Nanoelectronics From Nanocrystal Building Blocks." Advanced Materials 24, no. 2 (2012): 210-228.

6) Jiang, Zilong, Ferhat Katmis, Chi Tang, Peng Wei, Jagadeesh S. Moodera, and Jing Shi. "A comparative transport study of Bi2Se3 and Bi2Se3/yttrium iron garnet." Applied Physics Letters 104, no. 22 (2014): 222409.

7) Gamble, F. R., J. H. Osiecki, Mo Cais, R. Pisharody, F. J. DiSalvo, and T. H. Geballe. "Intercalation complexes of Lewis bases and layered sulfides: a large class of new superconductors." Science 174, no. 4008 (1971): 493-497.

8) Wang, Qing Hua, Kourosh Kalantar-Zadeh, Andras Kis, Jonathan N. Coleman, and Michael S. Strano. "Electronics and optoelectronics of two-dimensional transition metal dichalcogenides." Nature nanotechnology 7, no. 11 (2012): 699-712.

9) Jiang, Zilong, Cui-Zu Chang, Chi Tang, Jian-Guo Zheng, Jagadeesh S. Moodera, and Jing Shi. "Structural and proximity-induced ferromagnetic properties of topological insulator-magnetic insulator heterostructures." AIP Advances 6, no. 5 (2016): 055809.

10) Radisavljevic, Branimir, Aleksandra Radenovic, Jacopo Brivio, I. V. Giacometti, and A. Kis. "Single-layer MoS2 transistors." Nature nanotechnology 6, no. 3 (2011): 147-150.

11) Liu, Lei, Y. P. Feng, and Z. X. Shen. "Structural and electronic properties of h-BN." Physical Review B 68, no. 10 (2003): 104102.

12) Watanabe, Kenji, Takashi Taniguchi, and Hisao Kanda. "Direct-bandgap properties and evidence for ultraviolet lasing of hexagonal boron nitride single crystal." Nature materials 3, no. 6 (2004): 404-409.

13) Mas-Balleste, Ruben, Cristina Gomez-Navarro, Julio Gomez-Herrero, and Felix Zamora. "2D materials: to graphene and beyond." Nanoscale 3, no. 1 (2011): 20-30.

14) Jiang, Zilong, Cui-Zu Chang, Chi Tang, Peng Wei, Jagadeesh S. Moodera and Jing Shi. "Independent tuning of electronic property and ferromagnetism in topological insulator with heterostructure approach", Nano Lett. 15, 5835-5840 (2015)

15) Xu, Mingsheng, Tao Liang, Minmin Shi, and Hongzheng Chen. "Graphene-like two-dimensional materials." Chemical reviews 113, no. 5 (2013): 3766-3798.

16) Butler, Sheneve Z., Shawna M. Hollen, Linyou Cao, Yi Cui, Jay A. Gupta, Humberto R. Gutiérrez, Tony F. Heinz et al. "Progress, challenges, and opportunities in two-dimensional materials beyond graphene." ACS nano 7, no. 4 (2013): 2898-2926.

17) Geim, Andre K., and Irina V. Grigorieva. "Van der Waals heterostructures." Nature 499, no. 7459 (2013): 419-425.

18) Ponomarenko, L. A., A. K. Geim, A. A. Zhukov, R. Jalil, S. V. Morozov, K. S. Novoselov, I. V. Grigorieva et al. "Tunable metal-insulator transition in double-layer graphene heterostructures." Nature Physics 7, no. 12 (2011): 958-961.

19) Dean, C., A. F. Young, L. Wang, I. Meric, G-H. Lee, K. Watanabe, T. Taniguchi, K. Shepard, P. Kim, and J. Hone. "Graphene based heterostructures." Solid State Communications 152, no. 15 (2012): 1275-1282.

20) Jiang, Zilong, Cui-Zu Chang, Massoud Ramezani Masir, Chi Tang, Yadong Xu, Jagadeesh S. Moodera, Allan H. MacDonald, and Jing Shi. "Enhanced spin Seebeck effect signal due to spin-momentum locked topological surface states." Nature communications 7 (2016).

21) Dean, Cory R., Andrea F. Young, Inanc Meric, Chris Lee, Lei Wang, S. Sorgenfrei, K. Watanabe et al. "Boron nitride substrates for high-quality graphene electronics." Nature nanotechnology 5, no. 10 (2010): 722-726.

22) Kim, Ki Kang, Allen Hsu, Xiaoting Jia, Soo Min Kim, Yumeng Shi, Mildred Dresselhaus, Tomas Palacios, and Jing Kong. "Synthesis and characterization of hexagonal boron nitride film as a dielectric layer for graphene devices." ACS nano 6, no. 10 (2012): 8583-8590.

23) Giovannetti, Gianluca, Petr A. Khomyakov, Geert Brocks, Paul J. Kelly, and Jeroen Van Den Brink. "Substrate-induced band gap in graphene on hexagonal boron nitride: Ab initio density functional calculations." Physical Review B 76, no. 7 (2007): 073103.

24) Young, A. F., C. R. Dean, I. Meric, S. Sorgenfrei, H. Ren, K. Watanabe, T. Taniguchi, J. Hone, K. L. Shepard, and P. Kim. "Electronic compressibility of gapped bilayer graphene." preprint at (2010).

25) Shi, Yumeng, Christoph Hamsen, Xiaoting Jia, Ki Kang Kim, Alfonso Reina, Mario Hofmann, Allen Long Hsu et al. "Synthesis of few-layer hexagonal boron nitride thin film by chemical vapor deposition." Nano letters 10, no. 10 (2010): 4134-4139.

26) Bjelkevig, Cameron, Zhou Mi, Jie Xiao, P. A. Dowben, Lu Wang, Wai-Ning Mei, and Jeffry A. Kelber. "Electronic structure of a graphene/hexagonal-BN heterostructure grown on Ru (0001) by chemical vapor deposition and atomic layer deposition: extrinsically dopedgraphene." Journal of Physics: Condensed Matter 22, no. 30 (2010): 302002.

27) Yang, Wei, Guorui Chen, Zhiwen Shi, Cheng-Cheng Liu, Lianchang Zhang, Guibai Xie, Meng Cheng et al. "Epitaxial growth of single-domain graphene on hexagonal boron nitride." Nature materials 12, no. 9 (2013): 792-797.

28) Koma, Atsushi, Kazumasa Sunouchi, and Takao Miyajima. "Fabrication of ultrathin heterostructures with van der Waals epitaxy." Journal of Vacuum Science & Technology B 3, no. 2 (1985): 724-724.

29) Zhan, Ning, Guoping Wang, and Jianlin Liu. "Cobalt-assisted large-area epitaxial graphene growth in thermal cracker enhanced gas source molecular beam epitaxy." Applied Physics A: Materials Science & Processing 105, no. 2 (2011): 341-345.

30) Novoselov, Kostya S., Andre K. Geim, Sergei V. Morozov, D. Jiang, Y_ Zhang, Sergey V. Dubonos, Irina V. Grigorieva, and Alexandr A. Firsov. "Electric field effect in atomically thin carbon films." science 306, no. 5696 (2004): 666-669.

31) Chen, Jian-Hao, Chaun Jang, Shudong Xiao, Masa Ishigami, and Michael S. Fuhrer. "Intrinsic and extrinsic performance limits of graphene devices on SiO2." Nature nanotechnology 3, no. 4 (2008): 206-209.

32) Bolotin, Kirill I., K. J. Sikes, Zd Jiang, M. Klima, G. Fudenberg, J. Hone, Ph Kim, and H. L. Stormer. "Ultrahigh electron mobility in suspended graphene." Solid State Communications 146, no. 9 (2008): 351-355.

33) De, Sukanta, and Jonathan N. Coleman. "Are there fundamental limitations on the sheet resistance and transmittance of thin graphene films?" Acs Nano 4, no. 5 (2010): 2713-2720.

34) Balandin, Alexander A., Suchismita Ghosh, Wenzhong Bao, Irene Calizo, Desalegne Teweldebrhan, Feng Miao, and Chun Ning Lau. "Superior thermal conductivity of single-layer graphene." Nano letters 8, no. 3 (2008): 902-907.

35) Chandramohan, S., Kang Bok Ko, Jong Han Yang, Beo Deul Ryu, Y. S. Katharria, Taek Yong Kim, Byung Jin Cho, and Chang-Hee Hong. "Performance evaluation of GaN light-emitting diodes using transferred graphene as current spreading layer." Journal of Applied Physics 115, no. 5 (2014): 054503.

36) Lee, Changgu, Xiaoding Wei, Jeffrey W. Kysar, and James Hone. "Measurement of the elastic properties and intrinsic strength of monolayer graphene." science 321, no. 5887 (2008): 385-388.

37) Allen, Matthew J., Vincent C. Tung, and Richard B. Kaner. "Honeycomb carbon: a review of graphene." Chemical reviews 110, no. 1 (2009): 132-145.

38) Wang, Haibo, Thandavarayan Maiyalagan, and Xin Wang. "Review on recent progress in nitrogen-doped graphene: synthesis, characterization, and its potential applications." Acs Catalysis 2, no. 5 (2012): 781-794.

39) Emtsev, Konstantin V., Aaron Bostwick, Karsten Horn, Johannes Jobst, Gary L. Kellogg, Lothar Ley, Jessica L. McChesney et al. "Towards wafer-size graphene layers by atmospheric pressure graphitization of silicon carbide." Nature materials 8, no. 3 (2009): 203-207.

40) Hajlaoui, Mahdi, Haikel Sediri, Debora Pierucci, Hugo Henck, Thanyanan Phuphachong, Mathieu G. Silly, Louis-Anne De Vaulchier et al. "High Electron Mobility in Epitaxial Trilayer Graphene on Off-axis SiC (0001)." Scientific reports 6 (2016).

41) Faugeras, Clément, Anouck Nerrière, Marek Potemski, Ather Mahmood, Erik Dujardin, Claire Berger, and W. A. De Heer. "Few-layer graphene on SiC, pyrolitic graphite, and graphene: A Raman scattering study." Applied Physics Letters 92, no. 1 (2008): 011914.

42) Wang, Zhu-Jun, Gisela Weinberg, Qiang Zhang, Thomas Lunkenbein, Achim Klein-Hoffmann, Michalina Kurnatowska, Milivoj Plodinec et al. "Direct observation of graphene growth and associated copper substrate dynamics by in situ scanning electron microscopy." ACS nano 9, no. 2 (2015): 1506-1519.

43) Kim, Keun Soo, Yue Zhao, Houk Jang, Sang Yoon Lee, Jong Min Kim, Kwang S. Kim, Jong-Hyun Ahn, Philip Kim, Jae-Young Choi, and Byung Hee Hong. "Large-scale pattern growth of graphene films for stretchable transparent electrodes." nature 457, no. 7230 (2009): 706-710.

44) Patera, Laerte L., Cristina Africh, Robert S. Weatherup, Raoul Blume, Sunil Bhardwaj, Carla Castellarin-Cudia, Axel Knop-Gericke et al. "In situ observations of the atomistic mechanisms of Ni catalyzed low temperature graphene growth." ACS nano 7, no. 9 (2013): 7901-7912.

45) Zhan, Ning, Guoping Wang, and Jianlin Liu. "Cobalt-assisted large-area epitaxial graphene growth in thermal cracker enhanced gas source molecular beam epitaxy." Applied Physics A: Materials Science & Processing 105, no. 2 (2011): 341-345.

46) Hernández-Rodríguez, Irene, Jorge M. García, José A. Martín-Gago, Pedro L. de Andrés, and Javier Méndez. "Graphene growth on Pt (111) and Au (111) using a MBE carbon solid-source." Diamond and Related Materials 57 (2015): 58-62.

47) Sutter, Peter, Jerzy T. Sadowski, and Eli Sutter. "Graphene on Pt (111): Growth and substrate interaction." Physical Review B 80, no. 24 (2009): 245411.

48) Weatherup, Robert S., Ashwin J. Shahani, Zhu-Jun Wang, Ken Mingard, Andrew J. Pollard, Marc-Georg Willinger, Robert Schloegl, Peter W. Voorhees, and Stephan Hofmann. "In Situ Graphene Growth Dynamics on Polycrystalline Catalyst Foils." Nano Letters 16, no. 10 (2016): 6196-6206.

49) Wu, Ping, Wenhua Zhang, Zhenyu Li, and Jinglong Yang. "Mechanisms of graphene growth on metal surfaces: theoretical perspectives." Small 10, no. 11 (2014): 2136-2150.

50) Li, Yuan, and Nitin Chopra. "Progress in large-scale production of graphene. Part 2: vapor methods." Jom 67, no. 1 (2015): 44-52.

51) Cassabois, Guillaume, Pierre Valvin, and Bernard Gil. "Hexagonal boron nitride is an indirect bandgap semiconductor." Nature Photonics (2016).

52) Kim, Ki Kang, Allen Hsu, Xiaoting Jia, Soo Min Kim, Yumeng Shi, Mildred Dresselhaus, Tomas Palacios, and Jing Kong. "Synthesis and characterization of hexagonal boron nitride film as a dielectric layer for graphene devices." ACS nano 6, no. 10 (2012): 8583-8590.

53) Manchanda, L. and Gurvitch, M., 1988. Yttrium oxide/silicon dioxide: a new dielectric structure for VLSI/ULSI circuits. IEEE electron device letters, 9(4), pp.180-182.

54) Watanabe, Kenji, Takashi Taniguchi, Takahiro Niiyama, Kenta Miya, and Masateru Taniguchi. "Far-ultraviolet plane-emission handheld device based on hexagonal boron nitride." Nature photonics 3, no. 10 (2009): 591-594.

55) Kubota, Yoichi, Kenji Watanabe, Osamu Tsuda, and Takashi Taniguchi. "Deep ultraviolet light-emitting hexagonal boron nitride synthesized at atmospheric pressure." Science 317, no. 5840 (2007): 932-934.

56) Watanabe, Kenji, Takashi Taniguchi, and Hisao Kanda. "Direct-bandgap properties and evidence for ultraviolet lasing of hexagonal boron nitride single crystal." Nature materials 3, no. 6 (2004): 404-409.

57) Liu, Wei, Hong Li, Chuan Xu, Yasin Khatami, and Kaustav Banerjee. "Synthesis of high-quality monolayer and bilayer graphene on copper using chemical vapor deposition." Carbon 49, no. 13 (2011): 4122-4130.

58) Rakheja, Shaloo, Vachan Kumar, and Azad Naeemi. "Evaluation of the potential performance of graphene nanoribbons as on-chip interconnects." Proceedings of the IEEE 101, no. 7 (2013): 1740-1765.

59) Lee, Gwan-Hyoung, Young-Jun Yu, Changgu Lee, Cory Dean, Kenneth L. Shepard, Philip Kim, and James Hone. "Electron tunneling through atomically flat and ultrathin hexagonal boron nitride." Applied physics letters 99, no. 24 (2011): 243114.

60) Pacile, D., J. C. Meyer, Ç. Ö. Girit, and A. Zettl. "The two-dimensional phase of boron nitride: few-atomic-layer sheets and suspended membranes." Applied Physics Letters 92, no. 13 (2008): 133107.

61) Pierson, Hugh O. "Boron nitride composites by chemical vapor deposition." Journal of Composite Materials 9, no. 3 (1975): 228-240.

62) Rozenberg, A. S., Yu A. Sinenko, and N. V. Chukanov. "Regularities of pyrolytic boron nitride coating formation on a graphite matrix." Journal of materials science 28, no. 20 (1993): 5528-5533.

63) Adams, A. C. "Characterization of films formed by pyrolysis of borazine." Journal of The Electrochemical Society 128, no. 6 (1981): 1378-1379.

64) Bouchacourt, M., and F. Thevenot. "Analytical investigations in the B C system." Journal of the Less Common Metals 82 (1981): 219-226.

65) Auwärter, Willi, Hans Ulrich Suter, Hermann Sachdev, and Thomas Greber. "Synthesis of one monolayer of hexagonal boron nitride on Ni (111) from B-trichloroborazine (ClBNH) 3." Chemistry of materials 16, no. 2 (2004): 343-345.

66) Paffett, M. T., R. J. Simonson, P. Papin, and R. T. Paine. "Borazine adsorption and decomposition at Pt (111) and Ru (001) surfaces." Surface Science 232, no. 3 (1990): 286-296.

67) Nagashima, A. Y. A. T. O., N. Tejima, Y. Gamou, T. Kawai, and C. Oshima. "Electronic dispersion relations of monolayer hexagonal boron nitride formed on the Ni (111) surface." Physical Review B 51, no. 7 (1995): 4606.

68) Nagashima, A. Y. A. T. O., N. Tejima, Y. Gamou, T. Kawai, and C. Oshima. "Electronic states of monolayer hexagonal boron nitride formed on the metal surfaces." Surface science 357 (1996): 307-311.

69) Ćavar, E., R. Westerström, Anders Mikkelsen, Edvin Lundgren, A. S. Vinogradov, May Ling Ng, A. B. Preobrajenski, A. A. Zakharov, and Nils Mårtensson. "A single h-BN layer on Pt (111)." Surface Science 602, no. 9 (2008): 1722-1726.

70) Shi, Yumeng, Christoph Hamsen, Xiaoting Jia, Ki Kang Kim, Alfonso Reina, Mario Hofmann, Allen Long Hsu et al. "Synthesis of few-layer hexagonal boron nitride thin film by chemical vapor deposition." Nano letters 10, no. 10 (2010): 4134-4139.

71) Qin, Li, Jie Yu, Mingyu Li, Fei Liu, and Xuedong Bai. "Catalyst-free growth of mono-and few-atomic-layer boron nitride sheets by chemical vapor deposition." Nanotechnology 22, no. 21 (2011): 215602.

72) Dahal, R., J. Li, S. Majety, B. N. Pantha, X. K. Cao, J. Y. Lin, and H. X. Jiang. "Epitaxially grown semiconducting hexagonal boron nitride as a deep ultraviolet photonic material." Applied Physics Letters 98, no. 21 (2011): 211110.

73) Li, Xuesong, Carl W. Magnuson, Archana Venugopal, Rudolf M. Tromp, James B. Hannon, Eric M. Vogel, Luigi Colombo, and Rodney S. Ruoff. "Large-area graphene single crystals grown by low-pressure chemical vapor deposition of methane on copper." Journal of the American Chemical Society 133, no. 9 (2011): 2816-2819.

74) Sutter, Peter, Jayeeta Lahiri, Peter Albrecht, and Eli Sutter. "Chemical vapor deposition and etching of high-quality monolayer hexagonal boron nitride films." ACS nano 5, no. 9 (2011): 7303-7309.

75) Mönch, Winfried. "Valence-band offsets and Schottky barrier heights of layered semiconductors explained by interface-induced gap states." Applied physics letters 72, no. 15 (1998): 1899-1901.

76) Wang, W., K. K. Leung, W. K. Fong, S. F. Wang, Y. Y. Hui, S. P. Lau, Z. Chen, L. J. Shi, C. B. Cao, and Charles Surya. "Molecular beam epitaxy growth of high quality p-doped SnS van der Waals epitaxy on a graphene buffer layer." Journal of Applied physics 111, no. 9 (2012): 093520.

77) Parkinson, B. A., F. S. Ohuchi, K. Ueno, and A. Koma. "Periodic lattice distortions as a result of lattice mismatch in epitaxial films of two-dimensional materials." Applied physics letters 58, no. 5 (1991): 472-474.

78) Marchini, S., S. Günther, and J. Wintterlin. "Scanning tunneling microscopy of graphene on Ru (0001)." Physical Review B 76, no. 7 (2007): 075429.

79) Levendorf, Mark P., Cheol-Joo Kim, Lola Brown, Pinshane Y. Huang, Robin W. Havener, David A. Muller, and Jiwoong Park. "Graphene and boron nitride lateral heterostructures for atomically thin circuitry." Nature 488, no. 7413 (2012): 627-632.

80) Britnell, L., Gorbachev, R.V., Jalil, R., Belle, B.D., Schedin, F., Mishchenko, A., Georgiou, T., Katsnelson, M.I., Eaves, L., Morozov, S.V. and Peres, N.M.R., 2012. Field-effect tunneling transistor based on vertical graphene heterostructures. Science, 335(6071), pp.947-950.

81) Britnell, L., Gorbachev, R.V., Jalil, R., Belle, B.D., Schedin, F., Mishchenko, A., Georgiou, T., Katsnelson, M.I., Eaves, L., Morozov, S.V. and Peres, N.M.R., 2012. Field-effect tunneling transistor based on vertical graphene heterostructures. Science, 335(6071), pp.947-950.

82) Drögeler, M., Volmer, F., Wolter, M., Terrés, B., Watanabe, K., Taniguchi, T., Güntherodt, G., Stampfer, C. and Beschoten, B., 2014. Nanosecond spin lifetimes in single-and few-layer graphene–hBN heterostructures at room temperature. Nano letters, 14(11), pp.6050-6055.

83) Wang, Jingang, Fengcai Ma, and Mengtao Sun. "Graphene, hexagonal boron nitride, and their heterostructures: properties and applications." RSC Advances 7, no. 27 (2017): 16801-16822.

84) Zhong, Xiaoliang, Yoke Khin Yap, Ravindra Pandey, and Shashi P. Karna. "First-principles study of strain-induced modulation of energy gaps of graphene/BN and BN bilayers." Physical review B 83, no. 19 (2011): 193403.

85) Fan, Yingcai, Mingwen Zhao, Zhenhai Wang, Xuejuan Zhang, and Hongyu Zhang. "Tunable electronic structures of graphene/boron nitride heterobilayers." Applied Physics Letters 98, no. 8 (2011): 083103.

86) Neto, AH Castro, F. Guinea, Nuno MR Peres, Kostya S. Novoselov, and Andre K. Geim. "The electronic properties of graphene." Reviews of modern physics 81, no. 1 (2009): 109.

87) Cho, Al Y., and J. R. Arthur. "Molecular beam epitaxy." Progress in solid state chemistry 10 (1975): 157-191.

88) Song, Li, Lijie Ci, Hao Lu, Pavel B. Sorokin, Chuanhong Jin, Jie Ni, Alexander G. Kvashnin et al. "Large scale growth and characterization of atomic hexagonal boron nitride layers." Nano letters 10, no. 8 (2010): 3209-3215.

89) Kim, Ki Kang, Allen Hsu, Xiaoting Jia, Soo Min Kim, Yumeng Shi, Mario Hofmann, Daniel Nezich et al. "Synthesis of monolayer hexagonal boron nitride on Cu foil using chemical vapor deposition." Nano letters 12, no. 1 (2011): 161-166.

90) Guo, Ning, Jinquan Wei, Lili Fan, Yi Jia, Dayao Liang, Hongwei Zhu, Kunlin Wang, and Dehai Wu. "Controllable growth of triangular hexagonal boron nitride domains on copper foils by an improved low-pressure chemical vapor deposition method." Nanotechnology 23, no. 41 (2012): 415605.

91) Lee, Kang Hyuck, Hyeon-Jin Shin, Jinyeong Lee, In-yeal Lee, Gil-Ho Kim, Jae-Young Choi, and Sang-Woo Kim. "Large-scale synthesis of high-quality hexagonal boron nitride nanosheets for large-area graphene electronics." Nano letters 12, no. 2 (2012): 714-718.

92) Auwärter, Willi, Hans Ulrich Suter, Hermann Sachdev, and Thomas Greber. "Synthesis of one monolayer of hexagonal boron nitride on Ni (111) from B-trichloroborazine (ClBNH) 3." Chemistry of materials 16, no. 2 (2004): 343-345.

93) Liu, Yuanyue, Somnath Bhowmick, and Boris I. Yakobson. "BN white graphene with “colorful” edges: The energies and morphology." Nano letters 11, no. 8 (2011): 3113-3116.

94) Zhan, Ning, Mario Olmedo, Guoping Wang, and Jianlin Liu. "Layer-by-layer synthesis of large-area graphene films by thermal cracker enhanced gas source molecular beam epitaxy." Carbon 49, no. 6 (2011): 2046-2052.

95) Hao, Yufeng, M. S. Bharathi, Lei Wang, Yuanyue Liu, Hua Chen, Shu Nie, Xiaohan Wang et al. "The role of surface oxygen in the growth of large single-crystal graphene on copper." Science 342, no. 6159 (2013): 720-723.

96) Kim, Soo Min, Allen Hsu, P. T. Araujo, Yi-Hsien Lee, Tomás Palacios, Mildred Dresselhaus, Juan-Carlos Idrobo, Ki Kang Kim, and Jing Kong. "Synthesis of patched or stacked graphene and hBN flakes: a route to hybrid structure discovery." Nano letters 13, no. 3 (2013): 933-941.

97) Eckmann, Axel, Jaesung Park, Huafeng Yang, Daniel Elias, Alexander S. Mayorov, Geliang Yu, Rashid Jalil et al. "Raman fingerprint of aligned graphene/h-BN superlattices." Nano letters 13, no. 11 (2013): 5242-5246.

98) Moreau, E., F. J. Ferrer, D. Vignaud, S. Godey, and X. Wallart. "Graphene growth by molecular beam epitaxy using a solid carbon source." physica status solidi (a) 207, no. 2 (2010): 300-303.

99) Park, K. S., D. Y. Lee, K. J. Kim, and D. W. Moon. "Observation of a hexagonal BN surface layer on the cubic BN film grown by dual ion beam sputter deposition." Applied physics letters 70, no. 3 (1997): 315-317.

100) Wang, Min, Sung Kyu Jang, Won-Jun Jang, Minwoo Kim, Seong-Yong Park, Sang-Woo Kim, Se-Jong Kahng et al. "A Platform for Large-Scale Graphene Electronics–CVD Growth of Single-Layer Graphene on CVD-Grown Hexagonal Boron Nitride." Advanced Materials 25, no. 19 (2013): 2746-2752.

101) Novoselov, K. S., and AH Castro Neto. "Two-dimensional crystals-based heterostructures: materials with tailored properties." Physica Scripta 2012, no. T146 (2012): 014006.

102) Vinogradov, Nikolay A., A. A. Zakharov, Vancho Kocevski, Jan Rusz, K. A. Simonov, Olle Eriksson, Anders Mikkelsen et al. "Formation and structure of graphene waves on Fe (110)." Physical review letters 109, no. 2 (2012): 026101.

103) Kondo, Daiyu, Shintaro Sato, Katsunori Yagi, Naoki Harada, Motonobu Sato, Mizuhisa Nihei, and Naoki Yokoyama. "Low-temperature synthesis of graphene and fabrication of top-gated field effect transistors without using transfer processes." Applied physics express 3, no. 2 (2010): 025102.

104) Kondo, Daiyu, Katsunori Yagi, Motonobu Sato, Mizuhisa Nihei, Yuji Awano, Shintaro Sato, and Naoki Yokoyama. "Selective synthesis of carbon nanotubes and multi-layer graphene by controlling catalyst thickness." Chemical Physics Letters 514, no. 4 (2011): 294-300.

105) Lucchese, Márcia Maria, F. Stavale, EH Martins Ferreira, C. Vilani, M. V. O. Moutinho, Rodrigo B. Capaz, C. A. Achete, and A. Jorio. "Quantifying ion-induced defects and Raman relaxation length in graphene." Carbon 48, no. 5 (2010): 1592-1597.

106) Wang, Bao, Xing-Long Wu, Chun-Ying Shu, Yu-Guo Guo, and Chun-Ru Wang. "Synthesis of CuO/graphene nanocomposite as a high-performance anode material for lithium-ion batteries." Journal of Materials Chemistry 20, no. 47 (2010): 10661-10664.

107) Yamashita, Toru, and Peter Hayes. "Analysis of XPS spectra of Fe 2+ and Fe 3+ ions in oxide materials." Applied Surface Science 254, no. 8 (2008): 2441-2449.

108) Mattevi, Cecilia, Goki Eda, Stefano Agnoli, Steve Miller, K. Andre Mkhoyan, Ozgur Celik, Daniel Mastrogiovanni, Gaetano Granozzi, Eric Garfunkel, and Manish Chhowalla. "Evolution of electrical, chemical, and structural properties of transparent and conducting chemically derived graphene thin films." Advanced Functional Materials 19, no. 16 (2009): 2577-2583.

109) Li, Q-Q., X. Zhang, W-P. Han, Y. Lu, W. Shi, J-B. Wu, and P-H. Tan. "Raman spectroscopy at the edges of multilayer graphene." Carbon 85 (2015): 221-224.

110) Chae, Seung Jin, Fethullah Güneş, Ki Kang Kim, Eun Sung Kim, Gang Hee Han, Soo Min Kim, Hyeon-Jin Shin et al. "Synthesis of large-area graphene layers on poly-nickel substrate by chemical vapor deposition: wrinkle formation." Advanced Materials 21, no. 22 (2009): 2328-2333.

111) Banhart, Florian, Jani Kotakoski, and Arkady V. Krasheninnikov. "Structural defects in graphene." ACS nano 5, no. 1 (2010): 26-41.

112) Wofford, Joseph M., Shu Nie, Kevin F. McCarty, Norman C. Bartelt, and Oscar D. Dubon. "Graphene islands on Cu foils: the interplay between shape, orientation, and defects." Nano letters 10, no. 12 (2010): 4890-4896.

113) WooáLee, Jung, and Seung BináKim. "Enhanced Cr (VI) removal using iron nanoparticle decorated graphene." Nanoscale 3, no. 9 (2011): 3583-3585.

114) Tao, N. R., Z. B. Wang, W. P. Tong, M. L. Sui, Jian Lu, and Ke Lu. "An investigation of surface nanocrystallization mechanism in Fe induced by surface mechanical attrition treatment." Acta materialia 50, no. 18 (2002): 4603-4616.

115) Geng, Dongsheng, Songlan Yang, Yong Zhang, Jinli Yang, Jian Liu, Ruying Li, Tsun-Kong Sham, Xueliang Sun, Siyu Ye, and Shanna Knights. "Nitrogen doping effects on the structure of graphene." Applied Surface Science 257, no. 21 (2011): 9193-9198.

116) Hu, Yang, Jens Oluf Jensen, Wei Zhang, Lars N. Cleemann, Wei Xing, Niels J. Bjerrum, and Qingfeng Li. "Hollow spheres of iron carbide nanoparticles encased in graphitic layers as oxygen reduction catalysts." Angewandte Chemie International Edition 53, no. 14 (2014): 3675-3679.

117) Vlassiouk, Ivan, Murari Regmi, Pasquale Fulvio, Sheng Dai, Panos Datskos, Gyula Eres, and Sergei Smirnov. "Role of hydrogen in chemical vapor deposition growth of large single-crystal graphene." ACS nano 5, no. 7 (2011): 6069-6076.

118) Losurdo, Maria, Maria Michela Giangregorio, Pio Capezzuto, and Giovanni Bruno. "Graphene CVD growth on copper and nickel: role of hydrogen in kinetics and structure." Physical Chemistry Chemical Physics 13, no. 46 (2011): 20836-20843.

119) Lee, Jae-Hyun, Eun Kyung Lee, Won-Jae Joo, Yamujin Jang, Byung-Sung Kim, Jae Young Lim, Soon-Hyung Choi et al. "Wafer-scale growth of single-crystal monolayer graphene on reusable hydrogen-terminated germanium." Science 344, no. 6181 (2014): 286-289.

120) Ferrari, Andrea C., and Denis M. Basko. "Raman spectroscopy as a versatile tool for studying the properties of graphene." Nature nanotechnology 8, no. 4 (2013): 235-246.

121) Kundhikanjana, Worasom, Keji Lai, Hailiang Wang, Hongjie Dai, Michael A. Kelly, and Zhi-xun Shen. "Hierarchy of electronic properties of chemically derived and pristine graphene probed by microwave imaging." Nano letters 9, no. 11 (2009): 3762-3765.

122) Wei, Zhun, Eric Yue Ma, Yong-Tao Cui, Scott Johnston, Yongliang Yang, Krishna Agarwal, Michael A. Kelly, Zhi-Xun Shen, and Xudong Chen. "Quantitative analysis of effective height of probes in microwave impedance microscopy." Review of Scientific Instruments 87, no. 9 (2016): 094701.

123) Liu, Xun, Lei Fu, Nan Liu, Teng Gao, Yanfeng Zhang, Lei Liao, and Zhongfan Liu. "Segregation growth of graphene on Cu–Ni alloy for precise layer control." The Journal of Physical Chemistry C 115, no. 24 (2011): 11976-11982.

124) Chen, Shanshan, Weiwei Cai, Richard D. Piner, Ji Won Suk, Yaping Wu, Yujie Ren, Junyong Kang, and Rodney S. Ruoff. "Synthesis and characterization of large-area graphene and graphite films on commercial Cu–Ni alloy foils." Nano letters 11, no. 9 (2011): 3519-3525.

125) Wu, Yaping, Harry Chou, Hengxing Ji, Qingzhi Wu, Shanshan Chen, Wei Jiang, Yufeng Hao et al. "Growth mechanism and controlled synthesis of AB-stacked bilayer graphene on Cu–Ni alloy foils." Acs Nano 6, no. 9 (2012): 7731-7738.

126) Reina, Alfonso, Xiaoting Jia, John Ho, Daniel Nezich, Hyungbin Son, Vladimir Bulovic, Mildred S. Dresselhaus, and Jing Kong. "Large area, few-layer graphene films on arbitrary substrates by chemical vapor deposition." Nano letters 9, no. 1 (2008): 30-35.

127) Bae, Sukang, Hyeongkeun Kim, Youngbin Lee, Xiangfan Xu, Jae-Sung Park, Yi Zheng, Jayakumar Balakrishnan et al. "Roll-to-roll production of 30-inch graphene films for transparent electrodes." Nature nanotechnology 5, no. 8 (2010): 574-578.

128) Li, Xuesong, Weiwei Cai, Jinho An, Seyoung Kim, Junghyo Nah, Dongxing Yang, Richard Piner et al. "Large-area synthesis of high-quality and uniform graphene films on copper foils." Science 324, no. 5932 (2009): 1312-1314.

129) Wang, Shuai, Priscilla Kailian Ang, Ziqian Wang, Ai Ling Lena Tang, John TL Thong, and Kian Ping Loh. "High mobility, printable, and solution-processed graphene electronics." Nano letters 10, no. 1 (2009): 92-98.

130) Liu, Wei, Hong Li, Chuan Xu, Yasin Khatami, and Kaustav Banerjee. "Synthesis of high-quality monolayer and bilayer graphene on copper using chemical vapor deposition." Carbon 49, no. 13 (2011): 4122-4130.

131) Zuo, Zheng, Zhongguang Xu, Renjing Zheng, Alireza Khanaki, Jian-Guo Zheng, and Jianlin Liu. "In-situ epitaxial growth of graphene/h-BN van der Waals heterostructures by molecular beam epitaxy." Scientific reports 5 (2015): 14760.

132) Zheng, Renjing, Zhongguang Xu, Alireza Khanaki, Hao Tian, Zheng Zuo, Jian-Guo Zheng, and Jianlin Liu. "Low-temperature growth of graphene on iron substrate by molecular beam epitaxy." Thin Solid Films 627 (2017): 39-43.

133) Decker, Régis, Yang Wang, Victor W. Brar, William Regan, Hsin-Zon Tsai, Qiong Wu, William Gannett, Alex Zettl, and Michael F. Crommie. "Local electronic properties of graphene on a BN substrate via scanning tunneling microscopy." Nano letters 11, no. 6 (2011): 2291-2295.

134) Xue, Jiamin, Javier Sanchez-Yamagishi, Danny Bulmash, Philippe Jacquod, Aparna Deshpande, K. Watanabe, T. Taniguchi, Pablo Jarillo-Herrero, and Brian J. LeRoy. "STM Spectroscopy of ultra-flat graphene on hexagonal boron nitride." arXiv preprint arXiv:1102.2642 (2011).

135) Brugger, Thomas, Sebastian Günther, Bin Wang, J. Hugo Dil, Marie-Laure Bocquet, Jürg Osterwalder, Joost Wintterlin, and Thomas Greber. "Comparison of electronic structure and template function of single-layer graphene and a hexagonal boron nitride nanomesh on Ru (0001)." Physical Review B 79, no. 4 (2009): 045407.

136) Morscher, M., M. Corso, T. Greber, and J. Osterwalder. "Formation of single layer h-BN on Pd (111)." Surface science 600, no. 16 (2006): 3280-3284.

137) Gao, Yang, Wencai Ren, Teng Ma, Zhibo Liu, Yu Zhang, Wen-Bin Liu, Lai-Peng Ma, Xiuliang Ma, and Hui-Ming Cheng. "Repeated and controlled growth of monolayer, bilayer and few-layer hexagonal boron nitride on Pt foils." ACS nano 7, no. 6 (2013): 5199-5206.

138) Reina, Alfonso, Stefan Thiele, Xiaoting Jia, Sreekar Bhaviripudi, Mildred S. Dresselhaus, Juergen A. Schaefer, and Jing Kong. "Growth of large-area single- and bi-layer graphene by controlled carbon precipitation on polycrystalline Ni surfaces." Nano Research 2, no. 6 (2009): 509-516.

139) Xu, Zhongguang, Renjing Zheng, Alireza Khanaki, Zheng Zuo, and Jianlin Liu. "Direct growth of graphene on in situ epitaxial hexagonal boron nitride flakes by plasma-assisted molecular beam epitaxy." Applied Physics Letters 107, no. 21 (2015): 213103.

140) Xu, Zhongguang, Alireza Khanaki, Hao Tian, Renjing Zheng, Mohammad Suja, Jian-Guo Zheng, and Jianlin Liu. "Direct growth of hexagonal boron nitride/graphene heterostructures on cobalt foil substrates by plasma-assisted molecular beam epitaxy." Applied Physics Letters 109, no. 4 (2016): 043110.